POLITECNICO DI MILANO

Dipartimento di Chimica, Materiali e Ingegneria Chimica "Giulio Natta"

Scuola di Ingegneria Industriale e dell'Informazione

SHEAR STABILITY OF POLYMERIC COLLOIDAL DISPERSIONS:

INTERPLAY BETWEEN AGGREGATION AND COALESCENCE

Relatore: Prof. Davide Moscatelli

Correlatore: Dr. Miroslav Soos

Autore:

Luca Colonna

Matr. n. 797553

Anno Accademico 2013-2014

Contents

Acknowledgments

I want to express my deep gratitude to Professor Morbidelli for introducing me to the wonderful world of colloids and for giving me the opportunity to develop my master thesis in his research group at the ETH Zurich. I am very thankful to Professor Moscatelli, Dr. Soos, Dr. Bastian Brand, Baptiste Jaquet and Dr. Stefano Lazzari for their valuable supervision, outstanding patience, lesson and help.

In primis vorrei ringraziare di tutto cuore i miei genitori Ezio e Silvia per i valori che mi hanno trasmesso e per tutti i sacrifici fatti per permettermi di arrivare dove sono. Molte altre persone hanno reso possibile questo lavoro di tesi con il sostegno e l'appoggio che mi hanno sempre dimostrato, in particolare voglio ringraziare mia nonna Anna, la mia fidanzata Stefania, le mie sorelle Lucia e Cecilia, la zia Federica, i carissimi amici Alessio, Alessio, Christian, Francesco, Giovanna, Giulia, Marcello, Riccardo e Tommaso.

Ganz besonders möchte ich mich bei Steffi und Peter Lüthy dafür bedanken, dass sie mich in ihrer Familie so herzlich aufgenommen haben und mir in schwierigen Momenten mit Rat und Tat zur Seite standen.

Alla memoria della mia cara nonna Giovanna

Abstract

The aim of the present work is to study the role that coalescence plays in the aggregation under shear of polymeric colloidal dispersions.

Understanding the role of coalescence is very important not only from the scientific point of view, since at the moment in the literature a unified depiction of this phenomenon is missing, but also from the industrial one: indeed, coalescence is involved in many applications concerning the manufacture of polymer colloidal products and the design of polymer processes.

In the present study four samples of poly(methyl methacrylate –co- butyl acrylate) latexes have been synthesized by starved emulsion polymerization in a semi-batch reactor. Changing the monomer ratios leads to polymer particles exhibiting a glass transition temperature gradient which allows studying the coalescence process.
The coalescence behavior of our systems has been first clarified in stagnant conditions; while in a second stage shear conditions have been investigated.

1 INTRODUCTION

1.1 Emulsion Polymerization:

1.1.1 Description of the process:

Emulsion polymerization is a very common process in industrial application. It allows the production of a colloidal dispersion of polymer nanoparticles with a diameter of 50-500 nm in a continuous medium called latex and is typically carried out in stirred-tank reactors, which usually operate in a semi-continuous mode, although both batch and continuous operations are also used.

If the continuous phase is water one speaks of direct emulsions, otherwise of inverse emulsions. A typical direct emulsion polymerization process involves: monomers, water, surfactant and a water soluble initiator.

In a batch emulsion polymerization, at the beginning of the process the mixture of monomers is dispersed in water by stirring. Monomer droplets (100-1000µm) are formed and then stabilized by the emulsifier adsorbed on their surface.

The available surfactant actually partitions between the surface of the monomer droplets and the aqueous phase; if both the monomer droplets and the aqueous phase are saturated and further surfactant is added, the formation of micelles occurs. The concentration at which these aggregates are formed is the so called critical micellar concentration (CMC) (cf. Figure 1-1).

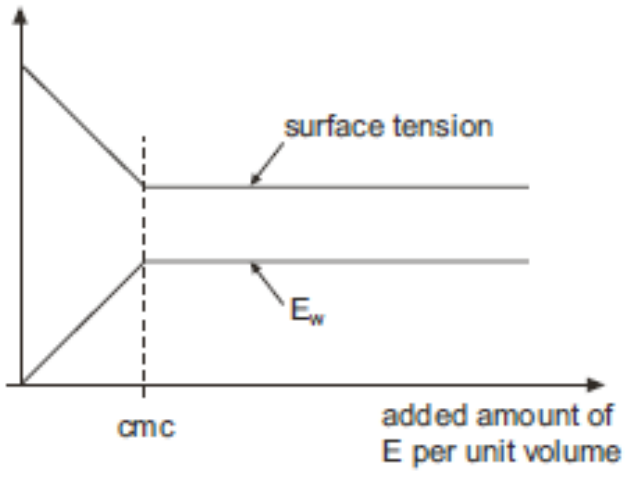

Figure 1-1 Trends of surface tension [J/m^2] and emulsifier concentration [mol/m^3] as a function of the added amount of emulsifier per unit volume [mol/m^3]: once the dispersion is saturated (cmc), since micelles are forming, the surface tension/emulsifier concentration stop decreasing/increasing and remain constant. Picture taken from [1]

Polymerization starts after the addition of water-soluble initiators. When a water-soluble initiator is added to the monomer dispersion, radicals are formed. They are usually too hydrophilic to enter the organic phase and rather react with the monomer dissolved in the aqueous phase, forming oligoradicals; after adding few monomer units they become quickly hydrophobic, giving rise to particle formation. In particular depending on E^0, the initial amount of surfactant, two processes of polymer particle formation (i.e. nucleation) are possible: heterogeneous nucleation and homogeneous nucleation. In case of heterogeneous nucleation as $E^0 >$ CMC, micelles are present and oligoradicals diffusive in the micelles, nucleating them. In case of homogeneous nucleation $E^0 <$ CMC, there is not sufficient surfactant in order to form micelles; the propagating radicals reach a critical length, become too hydrophobic and precipitate, creating particles nuclei. The emulsifier present in the system will adsorb onto the newly formed interface stabilizing the polymer particles. In both nucleation mechanisms, the oligoradicals could diffuse also into the monomer droplets. This further nucleation mechanism can be typically neglected, as the surface/volume ratio of the micelles in the heterogeneous nucleation case is much larger than the one of monomer droplets, being the latter three orders of magnitude larger in size.

Focusing on heterogeneous nucleation, as soon as the radicals enter the micelles, polymer particles are formed. In principle, a radical can terminate in the aqueous phase, enter previously formed particles or enter monomer droplets, but, if we assume a fast nucleation, all radicals enter completely micelles; it is worth to point out that radicals are formed during all the polymerization process, in fact their characteristic time of formation is larger than the monomer addition one. After typically 5-10% of conversion micelles are completely consumed by the entry of radicals and the stabilization of growing particles. This is the end of the nucleation and after that the number of particles will remain constant; this stage of the process is called interval I (cf. Figure 1-2). In interval II the system is composed by monomer droplets and monomer swollen polymer particles (up to 60% of their volume fraction), growing in time due to radical entry. The monomer diffuses from the droplets through the water on the polymer particles in order to maintain its volume fraction on particles constant. This interval continues as long as monomer droplets are present. In interval III monomer concentration in polymer particles and water phase decreases continuously. The rate of polymerization decreases so until the end of the process.

An exhaustive mathematical formulation of the batch emulsion polymerization kinetic mechanism can be found in [2].

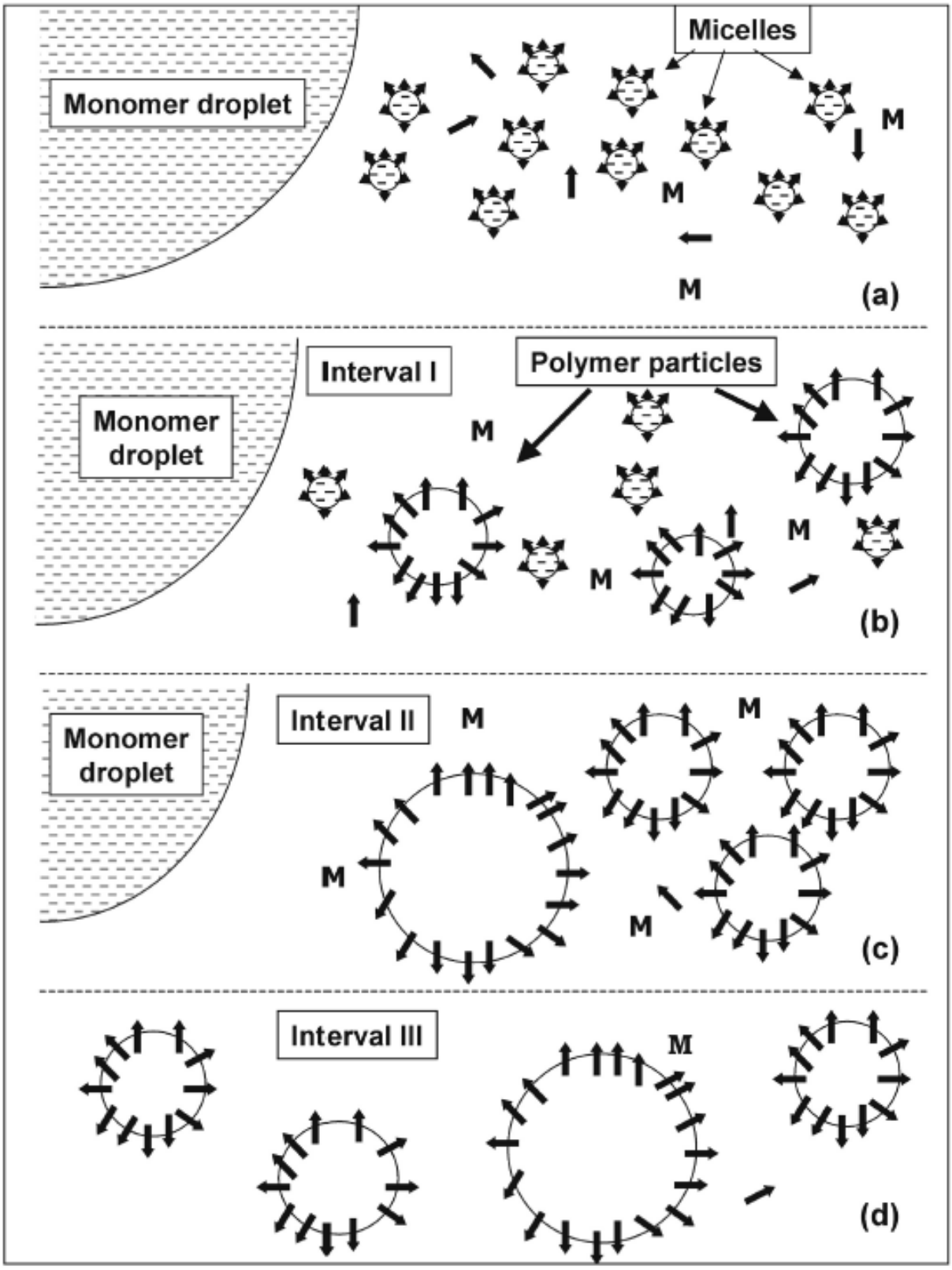

Figure 1-2 Intervals in batch heterogeneous emulsion polymerization. Picture taken from [3]

1.1.2 Composition and size control

In batch copolymerization processes it is important to control the chain composition due to the so-called composition drift occurring the more the reacting monomers exhibit different reactivity. To clarify this point, consider two monomers A and B, where both A and B preferentially react with A rather than with B (A has a larger reactivity ratio than B). Be X_A^0 the molar fraction of monomer A at time zero, the instantaneous chain composition of polymer $\overline{F_A}$ contains a certain fraction of monomer A, which is calculated via the Mayo-Lewis plot (cf. Figure 1-3). As the reaction takes place, the monomer phase becomes poorer of A and X_A decreases, leading the subsequent polymer chains to be as well poorer in A in composition (i.e. F_A decreases, cf. arrow in Figure 1-3)

This issue can be well appreciated looking at a general Mayo Lewis plot.

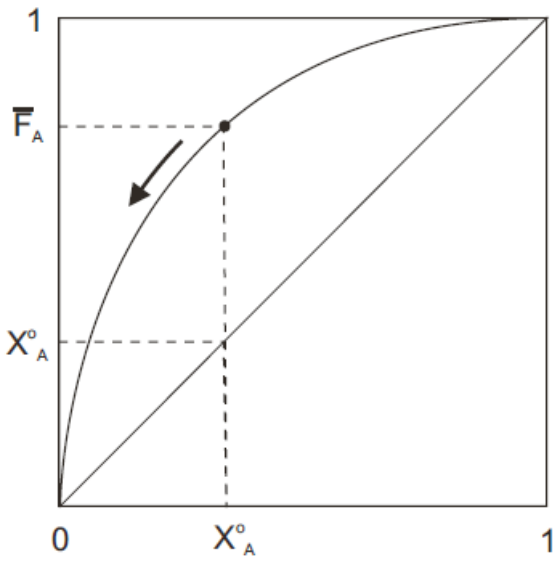

Figure 1-3 Mayo-Lewis plot in case the monomer A is the most reactive. Picture taken from [1]

It is very clear that the composition drift strongly affects the average composition of the chains. To avoid the composition drift, emulsion polymerization can be carried out in semibatch reactors, where a proper flow rate of the two monomers is fed to keep their mole fractions in the reactor constant.

The general mass balance for the i^{th}-monomer species in a semibatch reactor is:

$$\frac{dN_i}{dt} = \dot{N}_i - R_{pi}V \tag{1.1}$$

Where N_i, $\dot{N}_i$, R_{pi} and V represent the moles, the molar flow rate, the polymerization rate of the i^{th}-monomer and the reactor volume.

The reactor under consideration admits only one stable pseudo-steady state at sufficiently large times, equation (1.1) simplifies to:

$$\frac{dN_i}{dt} = 0 \tag{1.2}$$

$$\dot{N}_i = R_{pi}V = k_{pi}R^{\cdot}N_i^{pssa} \tag{1.3}$$

Where $R^{\cdot}$ is the overall concentration of radicals and k_{pi}. is the pseudo-propagation rate constant of the i^{th}-monomer species. The system evolves from the initial monomer concentrations approaching the steady state ones.

It is so a self-regulated system and by only keeping the two flow rates of the monomers at the value which grants the desired F_A, we can achieve composition control. Taking long feed times imposes to the system a much slower dynamics than its intrinsic, which is the monomer consumption. From a physical point of view all the monomer fed is immediately consumed as soon as it enters the system and monomer droplets cannot be formed. This operation modus is referred to as starved. In starved operations there is no monomer accumulation, and the global conversion overlaps with the monomer feed. Size control can be easily achieved in starved emulsion polymerization: as the particles grow progressively upon monomer addition, it is sufficient to stop the feed as the required particle size is reached.

1.2 Stability of colloidal suspensions:

A system state is considered stable if it returns unchanged to its original condition, after any perturbation that occurs. A process that evolves toward a stable state can be more accurately described in terms of thermodynamic functions: if it tends to a stable state, the variation of Gibbs free energy ΔG of this process is negative.
For general dispersion processes (cf. Figure 1-4) the variation of the surface free energy ΔG_{surf} is given by:

$$\Delta G_{surf} = \gamma \Delta A \tag{1.4}$$

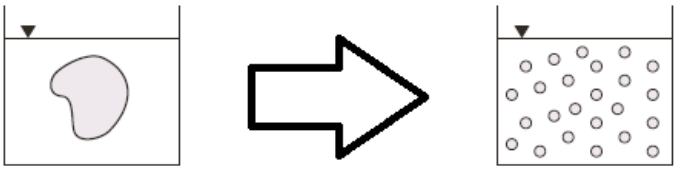

Figure 1-4 Dispersion process from a bulk to a dispersed state. Picture taken from [1]

γ is the surface tension at the interface and is twice the work per unit area required to separate up to infinite two parts of a liquid column; it can be interpreted as the work per unit area to create a new surface. ΔA is the variation of the system specific surface from the bulk (single big aggregate) to the dispersed state (colloid particles). Since smaller particles have a larger area/volume ratio ΔA is always positive.
The stability of such a system depends so on the sign of γ (cf. equation (1.4)): if the surface tension is positive, the colloidal dispersion is unstable; in fact positive γ means that positive work enters the system (i.e. stirring) in order to produce surfaces and maintain clear interphases separation (without stirring the particles would tend to collide, aggregate and return to their previous bulk state); on the other side if γ is negative, the colloidal system is stable; the particles remain “well dispersed” constituting a single phase with the dispersant medium.
In spite of thermodynamics, which states regardless time only the equilibrium state of a system, a temporary concept of stability can be introduced: kinetic meta-stability.

A kinetic meta-stable state is not the final stable configuration of the system but only a transient state in which the system remains for sufficient long times, slowly evolving towards the thermodynamic one.

Due to their nanoscale nature colloidal particles undergo only Brownian motion: they move randomly with an average kinetic energy proportional to $k_B T$ and follow Maxwell-Boltzmann speed distribution. This thermal agitation leads the particles to collide with one another and then to aggregate. In order to limit the aggregation-worth collisions an energy barrier sufficiently large to deal with the thermal energy can be built. Introducing such an energetic barrier, which can be overcome only by few particles according to Maxwell-Boltzmann speed distribution, increases the so called system shelf-life and makes the system kinetically meta-stable.

In general colloidal systems depending on their stability can be classified as lyophilic (stable) or lyophobic (unstable). Lyophobic colloids can be made kinetically meta-stable by bringing charges on the particles surfaces or coating the particles with some material that provides steric repulsion (cf. Figure 1-5).

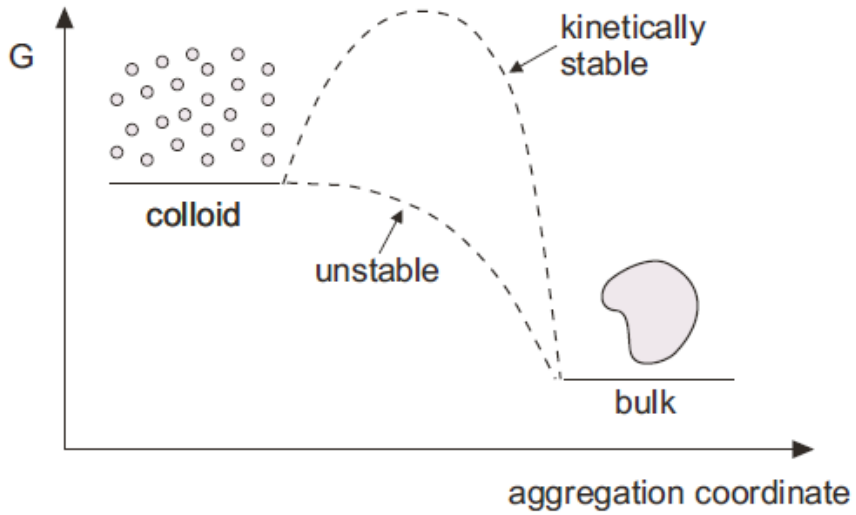

Figure 1-5 Building an energy barrier on lyophobic colloidal particles delays aggregation and the formation of the bulk state, thermodynamically preferred. Picture taken from [1].

1.3 Interaction between colloid particles:

1.3.1 Attractive interactions:

Purely physical attractive interactions between colloidal particles are referred to as Van der Waals interactions. These interactions are originated by the attraction between permanent charge distributions (i.e. dipoles, quadrupoles) and the corresponding induced charge distributions.
As shown in [1] an expression for the potential energy of interaction between two dipoles as function of the particles separation distance r can be derived:

$$V_{vdW}^{molec} = -\frac{C}{r^6} \tag{1.5}$$

Where C is a constant.
From equation (1.5) can be seen that Van der Waals interactions decay very strongly with the distance and become therefore relevant only at short range.

1.3.2 Repulsive interactions:

At interface separation between colloidal particles and their continuum medium are very commonly located electrical charges.
In particular, these charges can be brought on colloidal particles surfaces in several ways: by adsorption of an ionic surfactant or, by acting on the concentration of potential determining ions.
Regardless how charges are brought on particles surfaces, identically charged bodies involve electrical repulsive forces between themselves. In order to quantify these repulsive interactions it is possible to distinguish two regions: in the first, very close to the particle surface and few nanometers thick, counterions are fixedly adsorbed on their correspondent ions; in the second at larger distance Brownian motion dominates and the ions diffuse freely in the electrical field. This picture is referred to as the Helmoltz double layer (cf. Figure 1-6).

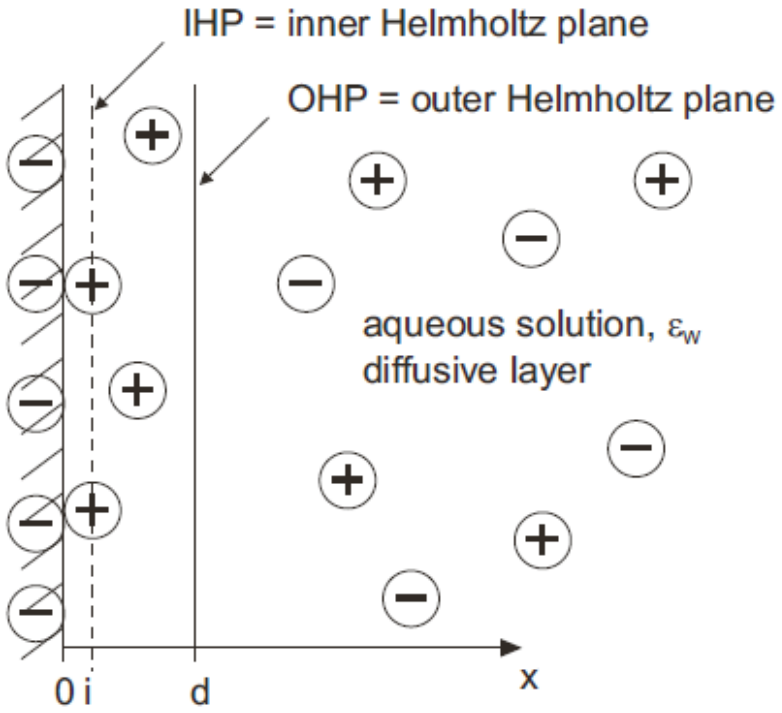

Figure 1-6 Helmoltz double layer. Picture taken from [1].

For x>0 the Poisson equation is valid:

$$\nabla^2\psi = -\frac{\rho}{\varepsilon} \tag{1.6}$$

Where ψ, ε, ρ are respectively electrostatic potential, medium permittivity and charge density. ρ can be expressed as $\sum_{i}^{all\ ions} n_i z_i e$, where n_i is the number ion concentration of the i^{th} ion, z_i is the valance of the ion and e is the electron charge.

For x>d is valid Boltzmann equation:

$$n_i = n_i^0 \exp\left(-\frac{z_i e\psi}{k_B T}\right) \tag{1.7}$$

Where k_B is Boltzmann constant and T is the system temperature. Combining equation (1.6) and equation (1.7) we obtain:

$$\nabla^2\psi = -\frac{1}{\varepsilon}\sum z_i e n_i^0 \exp(-\frac{z_i e\psi}{k_B T}) \tag{1.8}$$

with boundaries conditions: $\psi = 0$ at $x = \infty$ (bulk) and $\psi = \psi_d$ at $x = 0$.

Solving equation (1.8), it is possible to obtain ψ as a function of the distance. What is generally observed is that at a particular distance defined Debye length, the electrostatic potential becomes negligible. Physically the ions are completely screened by the layer of their corresponding counterions. The Debye length ξ is defined as:

$$\xi = \sqrt{\frac{\varepsilon k_B T}{2 N_A e^2 I}} \tag{1.9}$$

Where $I = \frac{\sum z_i^2 n_i^0}{2}$ is the solution ionic strength and N_A is the Avogadro number. This relation highlights a strong potential dependence from the solution electrolyte concentrations. In particular increasing the electrolyte concentration and so the ionic strength, ξ decreases meaning that the presence of charge will be perceived a shorter distances. This phenomenon is known as double layer compression and is widely used in applications to destabilize colloids.

When two charged bodies approach each other the corresponding double layer overlap, the local ion concentration increases compared to the bulk, thus creating an osmotic pressure and therefore a corresponding repulsive force.

Based on this approach several quantitative descriptions have been derived to evaluate the electrostatic repulsive potential energy V_R between two bodies.

1.3.3 DLVO theory

The Derjaguin-Landau-Verwey-Overbeek (DLVO) theory is commonly used to describe colloidal interactions. DLVO theory is based on the assumption that colloidal interactions can be explained as combination of attractive forces and repulsive forces.

The total potential interaction energy is so given by the sum of Van der Waals V_A and electrostatic V_R potential energy:

$$V_{tot} = V_A + V_R \tag{1.10}$$

The total potential curve has a number of important features in relation to colloidal stability (cf. Figure 1-7): it displays an intermediate maximum due to electrostatic forces that represents a potential energy barrier which has to be overcome for aggregation to occur; it shows a deep primary attractive well, indicating that Van der Waals forces dominate at short distances and once aggregation has occurred the aggregate is difficult to break; it points out that at high distance Van der Waals forces become relevant again leading to formation of a secondary less deep minimum and weaker aggregates. To decrease the energy barrier and so to induce aggregation it is possible acting on the ionic strength causing the compression of the double layer. Increasing salt concentration leads to a decrease of the potential energy barrier whose maximum becomes zero (curve d in Figure 1-7). At this point there is no opposition to aggregation which becomes controlled by Brownian diffusion. The smallest electrolyte concentration leading to such rapid coagulation is called critical coagulation concentration (CCC). Mathematically it corresponds to the situation where $V_{tot} = 0$ and $\frac{dV_{tot}}{dD} = 0$.

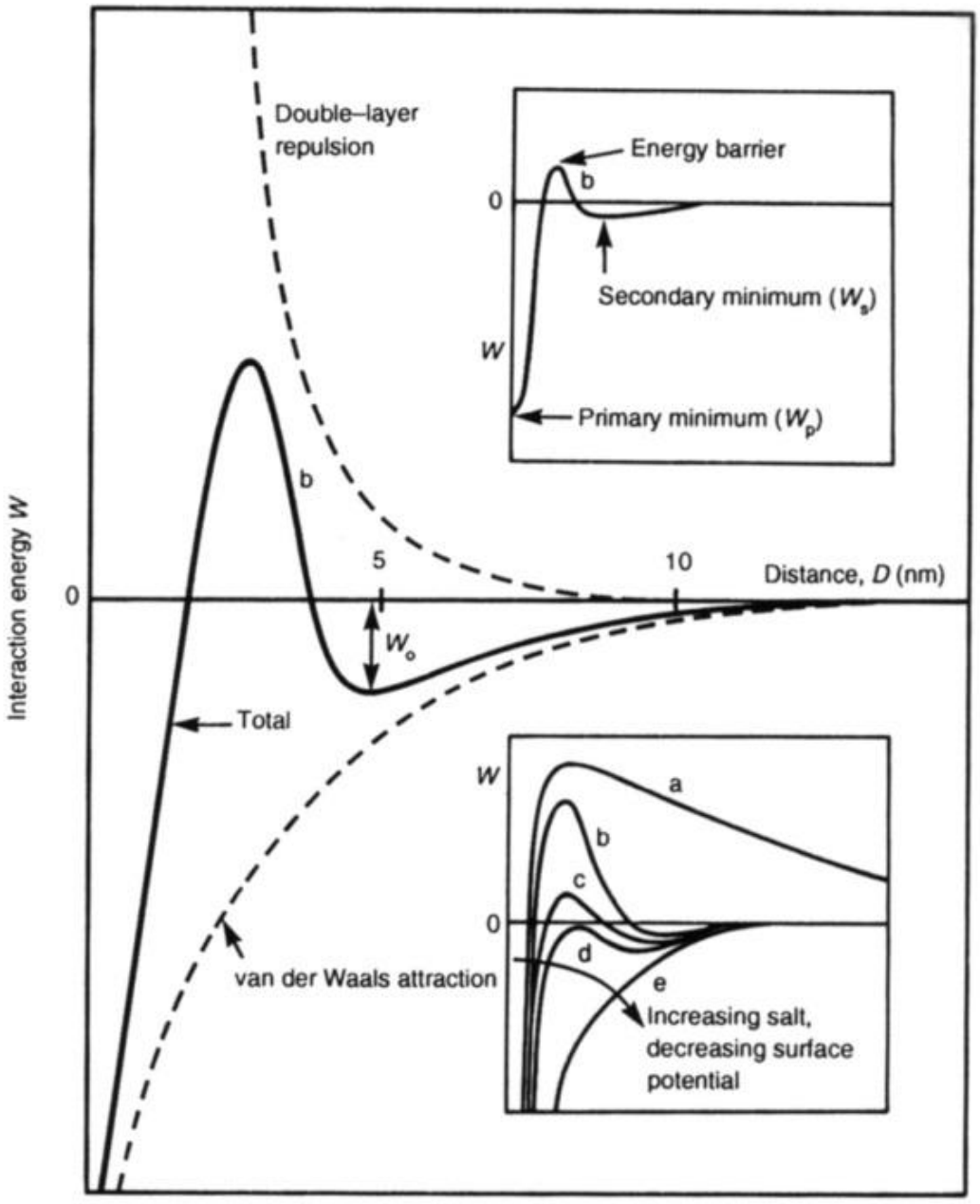

Figure 1-7 In the middle the total potential as sum of double layer repulsion and van der Waals attraction (dashed lines). At top right zoom on primary and secondary minimum. At bottom right effect of salt increase on the potential curve. Picture taken from [4]

1.4 Aggregation

As previously introduced, aggregation is the process in which colloidal particles, named primary particles, collide between themselves in their continuum medium and then stick together forming larger aggregates called clusters that can as well again collide and stick together.

The two main processes bringing particles together are Brownian motion and convection induced by an external imposed velocity field. The former process is referred to as stagnant or perikinetic aggregation, the latter as orthokinetic or shear-induced aggregation (SIA).

Regardless how particles get together, they may or may not stick one to each other depending on their interaction profile given by the DLVO potential: if no energetic barrier is present each collision will turn out to be effective. In case of stagnant conditions where the aggregation process would be dominated only by Brownian diffusion, this situation is classified as diffusion-limited cluster aggregation (DLCA). On the other hand, if an energetic barrier is present the particles can repel each other and every collision will not necessarily lead to an aggregate formation. This situation, somewhat analogous to the activation process for a bimolecular chemical reaction, is defined as reaction limited cluster aggregation (RLCA) and can occur in both stagnant and shear conditions.

During aggregation clusters of different shapes and masses are formed. In order to describe this distribution, typically broad, mass balances for each cluster must be written. This mathematical formalism was developed by Smoluchowski under the hypothesis that clusters breakage is negligible. The corresponding population balance equations (PBE) read:

$$\frac{dN_k}{dt} = \frac{1}{2}\sum_{i=1}^{k-1}\beta_{i,k-i}N_{k-i}N_i - N_k\sum_{i=1}^{\infty}\beta_{i,k}N_i \qquad (1.11)$$

N_k is the number concentration of k-mass aggregates, referred to as cluster mass distribution (CMD). The first term on the right side of equation (1.11) represents all the collisions of i,k-sized clusters that lead to the formation of k-sized clusters; the second term of equation (1.11) is the rate of disappearance of k-sized aggregates

with clusters of any mass. $\beta_{i,k}$ are the aggregation rate constants, expressions for RLCA, DLCA and SIA will be derived more in details in the following sections.

1.4.1 Diffusion limited cluster aggregation kernel

It is worth to focus on a single fixed (non-diffusing) particle with a hydrodynamics radius a, which interacts with equally sized, freely diffusing particles. Under the assumption that upon collision the diffusive particles disappear, the system governing equation is the continuity equation

$$\frac{\partial N}{\partial t} + div(\boldsymbol{J}) = 0 \tag{1.12}$$

where $\boldsymbol{J} = \frac{F}{S}$ with F the flux of identical particles diffusing through a sphere with surface S centered around the reference particle (cf. Figure 1-8).

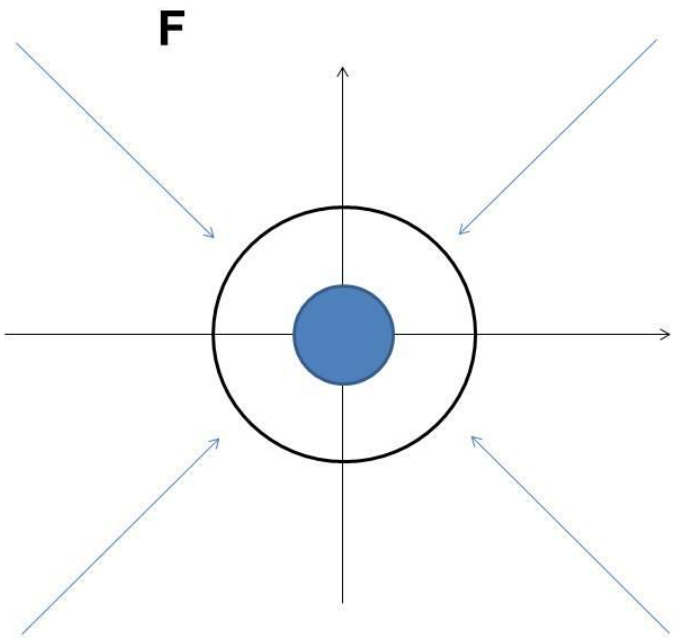

Figure 1-8 Flux of identical particles diffusing through a sphere centered around a reference particle.

At steady state equation (1.12) becomes

$$\frac{\partial N}{\partial t} = 0 \tag{1.13}$$

And

$$div\left(F\right) = 0 \tag{1.14}$$

in case of aggregation entirely controlled by diffusion according to Fick's law F expression is given by

$$F = 8\pi r^2 D \frac{dN}{dr} \tag{1.15}$$

Where D is the self-diffusion coefficient, N the particle concentration and r the radius of the sphere. Integrating equation (1.15) from bulk condition ($r = \infty$ and $N = N_0$) to the particle contact point ($r = 2a$ and $N = 0$.) leads to:

$$F = 8\pi D(2a)N_0 \tag{1.16}$$

The total rate of capture per unit volume of the system would be

$$\frac{dN}{dt} = -\frac{1}{2} F N_0 = -\frac{1}{2} \beta N_0^2 \tag{1.17}$$

Where $\beta = \frac{F}{N_0}$ and the factor 0.5 is used not to count twice the same collision event.

Since the particles are treated as hard spheres, one may express D in terms of the Einstein-Smoluchowski equation as:

$$D = \frac{k_B T}{6\pi\eta a} \tag{1.18}$$

Where η is the medium dynamic viscosity. β becomes

$$\beta = \frac{8}{3}\frac{k_B T}{\eta} \tag{1.19}$$

This expression for β is valid only in case of identical aggregates sizes and is referred as β_{ii}. In case of different size particles with radii R_i and R_j can be shown that (cf. [1]):

$$\beta_{ij} = 4\pi(R_i + R_j)(D_i + D_j) = \frac{2}{3}\frac{k_B T}{\eta}(R_i + R_j)(\frac{1}{R_i} + \frac{1}{R_j}) \tag{1.20}$$

In order to solve PBE in the general case where the aggregation rate is size dependent β_{ij} must be correlated to the masses i and j of the two colliding clusters. From scattering measurements it has been observed that aggregating clusters exhibit a self-similar (fractal) morphology and so $R_i \propto i^{d_f}$,where d_f is defined as the fractal dimension. In particular d_f equal to one corresponds to a line, d_f equal to two to a plane and d_f equal to three to a sphere (typical values for d_f in DLCA are in the range 1.6-1.9).

It is so finally possible to link β_{ij} with i and j obtaining the following expression:

$$\beta_{ij} = \frac{2}{3}\frac{k_B T}{\eta}(i^{\frac{1}{d_f}} + j^{\frac{1}{d_f}})(i^{-\frac{1}{d_f}} + j^{-\frac{1}{d_f}}) \tag{1.21}$$

1.4.2 Reaction limited cluster aggregation kernel

In case of perikinetic aggregation where is present a repulsive energy barrier between particles aggregation is potential-limited. In detail if two diffusing particles

interact with one another they experience a force given by their total interaction potential V_{tot}:

$$F_{tot} = -\frac{dV_{tot}}{dr} \tag{1.22}$$

This force is equilibrated by the Stokes friction force $F_{fc} = Bu$ where B is the friction coefficient in a viscous fluid and u the particle speed.
It is possible to show that the expression for the flux F becomes so:

$$F = 8\pi r^2 D\left(\frac{dN}{dr} + \frac{N}{k_B T}\frac{dV_{tot}}{dr}\right) \tag{1.23}$$

Integrating equation (1.23) at steady state from bulk condition ($r = \infty$, $N = N_0$. and $V_{tot} = 0$) to the particle contact point ($r = 2a$ and $N = 0$) leads to:

$$F = \frac{8\pi D N_0}{\int_{2a}^{\infty} e^{\frac{V_{tot}}{k_B T}} \frac{dr}{r^2}} \tag{1.24}$$

It is worth to point out that if $V_{tot} = 0$ in the whole domain we obtain the same previous DLCA flux. β (defined as $\frac{F}{N}$) can be extended to RLCA. It becomes so possible compare DLCA kernel with RLCA:

$$\frac{\beta^{DLCA}}{\beta} = \frac{F^{RLCA}}{F} = W = 2a\int_{2a}^{\infty} e^{\frac{V_{tot}}{k_B T}} \frac{dr}{r^2} \tag{1.25}$$

The parameter W defined as Fuchs stability ratio gives crucial information about how distant in term of stability is the system from its most unstable configuration: if W =1 the system is fully destabilized; if W increases the stability improves.
The meaning of W can be more appreciated in relation to the system salt concentration and its most important effect: the double layer compression.

Looking at the region in Figure 1-9 where W >1 can be observed that increasing the salt concentration leads to a less stable situation until in the region where W =1 the system is completely under diffusion control. It is important to note that the intersection of the two straight lines indicates the CCC value, where the energy barrier vanishes.

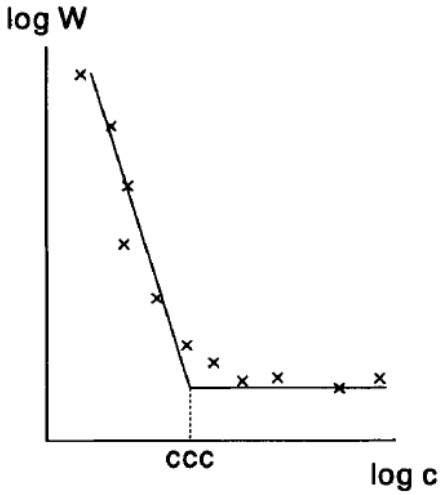

Figure 1-9 Typical profile of the Fuchs stability ratio as function of the salt concentration. Picture taken from [5]

The earlier comparison between DLCA and RLCA kernel was obtained only considering primary particles. To extend this to the aggregation of two clusters with sizes i and j the interaction aggregate-aggregate can be approximated with the interaction between the two colliding primary particle (described by the stability ratio W) and the rate of aggregation can be assumed proportional to the probability of collision between primary particles on the cluster surface.

For a given k-mass cluster the change in the primary particles in the cluster with is size a_k is given by:

$$k \propto (\frac{a_k}{a})^{d_f} \rightarrow \frac{dk}{da_k} \propto \frac{d_f}{a}(\frac{a_k}{a})^{d_f-1} \propto \frac{d_f}{a} k^{\frac{d_f-1}{d_f}} \tag{1.26}$$

The final expression for RLCA kernel results so:

$$\beta_{ij}^{RLCA} = \frac{\beta^{DLCA}_{ij}}{W}(ij)^{\lambda} \tag{1.27}$$

Where $\lambda = \frac{d_f - 1}{d_f}$ (typical RLCA d_f are in the range 2-2.2). More in general λ is obtained by fitting experimental data.

1.4.3 Shear induced aggregation kernel

The most general situation in orthokinetic aggregation is when the diffusing particles are immersed in an external speed field and their DLVO potentials V_{tot} interact with one another [6].
The expression for F is given by (cf. [6]):

$$F = \oint \left(\frac{ND}{k_B T} \left(-\nabla V_{tot} + Bu \right) - D\nabla \left(N \right) \right) \boldsymbol{n} dS \tag{1.28}$$

Equation (1.28) if inserted in the continuity equation (equation (1.12)) leads to a three-dimensional space partial differential equation that cannot be solved analytically. However since our problem is to determine the collision frequency the equation can be reduced to an ordinary differential equation in the radial distance as the independent variable. Integrating under the proper boundary conditions (cf. [6]) equation (1.28) becomes:

$$F = \frac{16\pi DaN_0}{2\int_0^{\frac{\delta}{a}} \frac{dx}{\chi(x)(x+2)^2} exp \int_{\frac{\delta}{a}}^{x} dx \, [\frac{1}{k_B T} \frac{dV_{tot}}{dx} + Pev_{eff}]} \tag{1.29}$$

Where δ is the thickness of the hydrodynamic boundary layer, x is the surface to surface radial distance between particles, $\chi(x)$ is an hydrodynamic functions accounting for the resistance of the solvent being squeezed when two particles approach each other, v_{eff} is the relative velocity between two particles normalized by $a\dot{\gamma}$ ($\dot{\gamma}$ is the shear rate [1/s]) and Pe is the Peclet number (the ratio between shear and Brownian forces)

$$Pe = \frac{3\eta\pi a^3 \dot{\gamma}}{k_B T} \tag{1.30}$$

A more generalized expression for the stability ratio W valid for arbitrary Pe numbers and interaction potentials can be obtained:

$$W = 2\int_0^{\frac{\delta}{a}} \frac{dx}{\chi(x)(x+2)^2} exp\int_{\frac{\delta}{a}}^{x} dx \, [\frac{1}{k_B T}\frac{dV_{tot}}{dx} + Pev_{eff}] \tag{1.31}$$

The integrals in equation (1.31) need again to be evaluated numerically. Further approximations can be done by considering high interaction potential barrier and moderate Peclet numbers. These simplifications lead to a loss of accuracy in the calculation and allow only a proportional relation (cf. [6]):

$$W \propto e^{\frac{V_m}{k_B T} - 2\alpha Pe} \tag{1.32}$$

Where V_m is the value of the potential and evaluated at the maximum of the interaction potential; α is a geometric parameter. From the W expression can be evaluated the shear induced aggregation kernel which is given by

$$\beta_{ij}^{SIA} \propto e^{-\frac{V_m}{k_B T} + 2\alpha Pe} \tag{1.33}$$

Finally a characteristic time for binary encounters can be introduced. This is referred to as characteristic time of aggregation and is defined as:

$$\tau_{agg} = \frac{W}{\beta^{DLCA} N_0} \tag{1.34}$$

1.5 Gelation

In viscous liquid dispersions with solid volumetric fraction higher than 1% aggregation processes end most of the times in the formation of a viscoelastic solid phase, usually referred as colloidal gel. After clusters are formed, due to the ongoing aggregation, they continuously grow in time as long as they interconnect with one another and thus create a network which occupies all the dispersion available volume (cf. Figure 1-10).

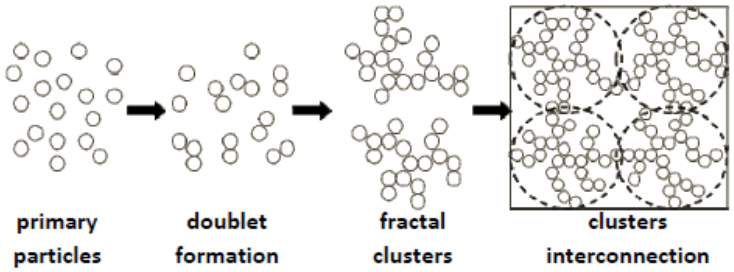

Figure 1-10 Steps of gel formation. Picture taken from [1].

In order to identify the condition at which the system gel can be introduced the volume fraction of cluster at time t:

$$\varphi(t) = \sum_i \frac{4}{3}\pi N_i R_i^3 \tag{1.35}$$

Where N_i is the cluster mass distribution and R_i, is the smallest sphere radius containing the aggregate. When $\varphi(t)$ reaches 0.5 half of the dispersion volume is occupied by cluster that cannot freely move any more. At this point where interconnection starts the system stop behaving like a viscous liquid becoming a viscoelastic solid able to sustain applied external stresses. The gel time t_{gel} depends on the regime at which gelation takes place: in DLCA there is no energy repulsion and the CMD is rather mono-disperse (all clusters experience the same environment and are on average separated by the same short distances) so the gelation process is very fast; in RLCA the interconnection process is not instantaneous because of the energy barrier and the super poly-disperse CMD which decreases the diffusion speed since clusters of different sizes obstruct one another.

1.6 Coalescence

Coalescence is the process in which the dispersed phase is a fluid. The liquid droplets join together fusing in larger droplets and in so doing destroy interfacial area. In order for particles to coalesce, they first need to approach closely enough to aggregate, then they interdiffuse in one another, melting in a single droplet (cf. Figure 1-11).

Figure 1-11 Steps of coalescence: approach, aggregation and finally coalescence.

A characteristic time of coalescence was introduced by Frenkel [7]:

$$\tau_{coal} \propto \frac{\eta_p d}{\gamma} \tag{1.36}$$

Where η_p is the particles viscosity, d the diameter of the final sphere and γ the surface tension.

Coalescence strongly affects the final shape of clusters. In fact if its characteristic time is comparable with the time of aggregation spherical cluster are formed and in this case no gelation can occur.

In polymeric dispersions coalescence can occur only if the system temperature is above the material glass transition temperature T_g. In fact above T_g a non-crystalline polymer material behaves rubbery or like a viscous fluid, depending on how much the temperature exceeds the T_g; below T_g a bulk polymer shows hard-solid material features.

2 SAMPLES PREPARATION:

2.1 Synthesis:

2.1.1 Materials:

Four samples of poly(methylmethacrylate-co-butylacrylate) P(MMA-co-BA) have been synthesized by starved emulsion polymerization in a semi-batch reactor. These samples are copolymers produced at different mass ratios (Table 2-1) of methyl methacrylate (MMA) and butyl acrylate (BA) (cf. Figure 2-1)

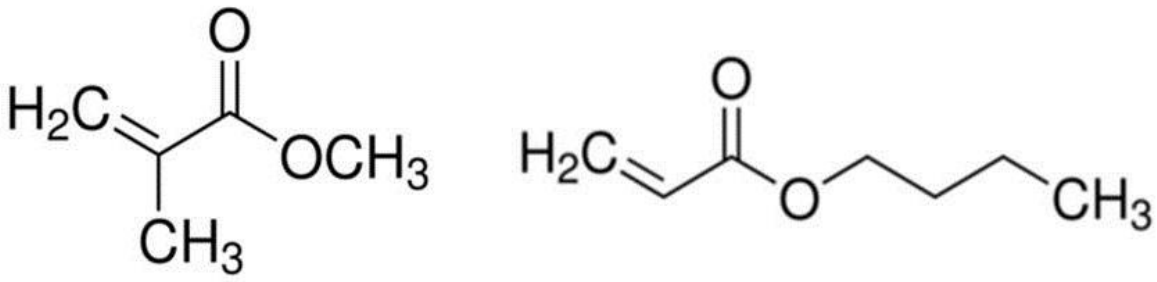

Figure 2-1 Left methylmethacrylate molecule; Right butylacrylate molecule

Table 2-1 Mass ratios of MMA and BA for each sample

PMMA-co-BA	%MMA	%BA
SAMPLE 1	30	70
SAMPLE 2	50	50
SAMPLE 3	60	40
SAMPLE 4	70	30

Henceforth every sample will be identified by referring only to its MMA content.
MMA and BA were supplied by ABCR CHEMICALS with purities of 99% and were used as received.

During the polymerization Sodiumdodecylsulfate (SDS) and Potassiumpersulfate (KPS) were used as surfactant and initiator respectively (cf. Figure 2-2).

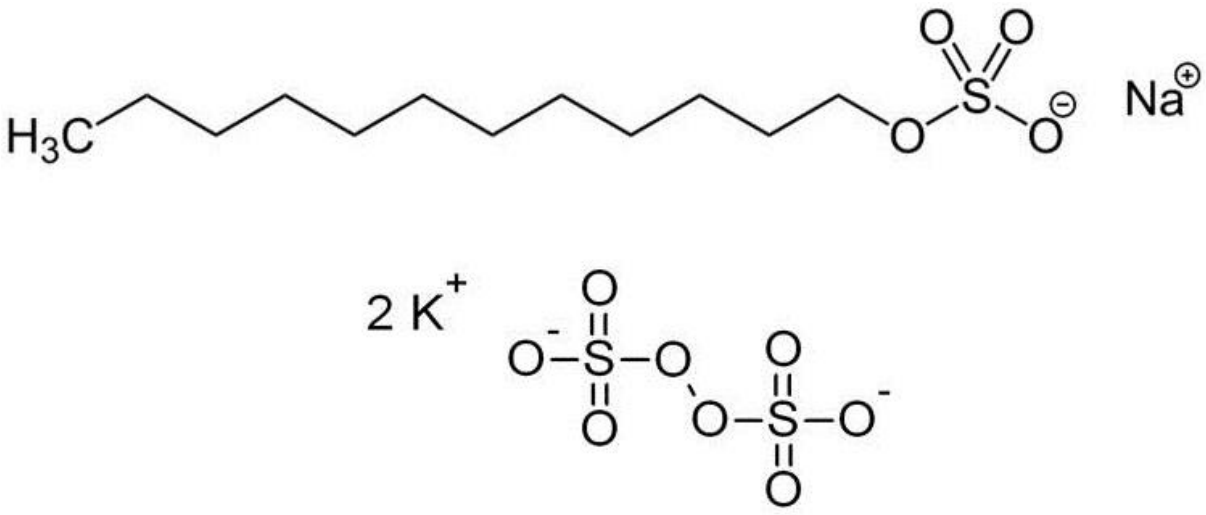

Figure 2-2 Top Sodiumdodecylsulfate; bottom Potassiumpersulfate

The amounts of SDS and KPS relative to each sample are listed in Table 2-2:

Table 2-2 Amounts of SDS and KPS relative to each sample

%MMA	SDS [g]	KPS [g]
30	0.291	0.815
50	0.275	0.815+0.4
60	0.227	0.815
70	0.207	0.815

SDS with purity >99% was provided by Apollo scientific; KPS with purity >99% was provided by Sigma-Aldrich. Both were used as received.
It is worth to point out that in each synthesis the nucleation was homogenous; in fact surfactant amount did not exceed the CMC (from the literature 6-8 [mM] at 25 [ºC]).
Deionized water previously stripped for 40 minutes with nitrogen (in order to remove oxygen) was employed as continuous phase in the polymerization.

2.1.2 Equipment:

The polymerization was run round bottom flask of 1000 ml. Four openings were present on the top of this flask: one was used to connect it with a water condenser, all the others were sealed with septums.
These caps were able to avoid air entry and to allow the feed through capillaries of the monomer using a volumetric pump and of the nitrogen.
Temperature and mixing control were achieved through a programmable heating plate, in particular a thermocouple linked to the heating plate.

2.1.3 Protocol:

- SDS was initially charged into the reactor dissolved into 673 [ml] of water (approximately with a ratio SDS/ water of 0.04%)
- The mixture was heated to 70 ºC and stirred at 800 r.p.m.
- KPS dissolved in 40 [ml] of water, once the temperature was reached and stabilized for 20 minutes, was added (approximately with a ratio KPS/ water of 0.19-0.12%)
- After temperature stabilization 10 minutes the monomers feed (0.285 [ml/min]) was started
- Samples were taken during the polymerization in order to monitor conversion, particle size, particle polydispersity (PDI), and dry content (DC); as soon as DC>5% and the sample particles reached sizes of circa 200 [nm] the feed was stopped
- The latex was kept at 70 ºC for one hour in order to guarantee a complete monomer conversion
- During the whole polymerization the reactor was purged with nitrogen

Exception: the polymerizations of the 50% MMA lasted longer than five hours so it was necessary to add after five hours 0.4 [g] of KPS dissolved in 20 [ml] of water in order to guarantee a continuous radicals production.
During sampling after circa one hour only unitary conversion were measured. At the end of the polymerization every sample was cooled and filtered with filters paper.
The final sizes, PDI and dry contents of the samples are reported in Table 2-3.

Table 2-3 Samples final particles average diameter, polydispersity index and dry content

%MMA	Average diameter [nm]	PDI [-]	DC [%]
30	198	0.027	9.73
50	188	0.016	13.44
60	199	0.017	9.42
70	198	0.021	9.48

Sizes and PDI measurements were performed by dynamic light scattering DLS.
It is relevant to note that the PDI index (dimensionless measure of the broadness of the size distribution) is not defined as common. In the DLS software it is calculated by cumulant analysis and it ranges from 0 to 1. Zero value stands for completely mono-dispersed samples whereas one for very poly-dispersed ones. Values of PDI<0.05 are normally encountered with monodisperse latexes.

2.2 Purification:

2.2.1 Materials:

In order to purify the latexes from the ions (surfactant, sodium and potassium) an ion exchange resin was used. Ion exchange is the reversible interchange of ions between a solid (ion exchange material) and a liquid in which there is no permanent change in the structure of the solid. Conventionally ions exchange resins consists of a cross-linked polymer matrix with a relatively uniform distribution of ion-active sites throughout the structure [8].
The ion exchange resin used as received in our application was Dowex Marathon MR-3 hydrogen and hydroxide form 20-50 mesh, provided by SIGMA ALDRICH.
On this resin matrix are present both cationic H^+ and anionic OH^- sites so all the target ions were removed.

In order to check the effective removal of surfactant the interfacial tension of each purified latex was measured with a dynamic contact angle meter and tensiometer (supplied by DATAPHYSICS).

2.2.2 Protocol:

- An amount of resin between 10-20% of the latex mass was added to the sample to purify
- The resin was removed by filtrating the solution with 50 [μm] and 5 [μm] filters
- 5 [ml] of the sample where diluted in 50 [ml] of water and the interfacial tension was measured

The protocol was repeated until the values of γ were comparable with the one of pure water (73 [mN/m]). The final γ values are listed in Table 2-4.

Table 2-4 Samples final γ values

%MMA	γ [mN/m]
30	71.89
50	72.02
60	72.34
70	72.21

At the end of the purification in order to check if aggregation occurred the sizes of all the samples were measured. No appreciable differences were found.

2.3 Composition control:

2.3.1 Equipment: Differential scanning calorimetry

Although starved emulsion polymerization assured an excellent composition control, further composition verifications can be carried out by measuring the samples glass transition temperatures. From the literature it results a T_g of 105 ºC for the pure MMA polymers and of -43 ºC for the pure BA ones; changing in the intermediate samples the composition ratio MMA/BA should lead to a T_g gradient among these two temperatures (cf. Table 2-5).

Differential scanning calorimetry (DSC) is one of the most effective methods of determining glass transition temperature. The basis of DSC is the change in the specific heat of a polymer due to the change of temperature as it passes through the glass transition point; particularly the heat capacity increases at T_g going from amorphous solid to viscous liquid.

In a typical DSC experiment [9], two pans (one contains the polymer and the other is empty [reference pan]) are placed in an inert atmosphere on a pair of identically positioned platforms connected with a heating system. The two pans are heated up at exactly the same specific rate despite the fact that one pan contains polymer and the other one is empty. In order to keep the temperature of the sample pan increasing at the same rate as the reference pan more heat is required; so it is possible to plot this difference in the heat flow as a function of temperature.

When there is no glass transition in the polymer, the heat flow in the plot is parallel to the x-axis; when the glass transition temperature is reached the heat flow shows an increased slope. Usually as T_g is taken approximately the middle of the increased slope. For the analysis was used the DSC Q200 provided by TA INSTRUMENTS. The pan material was aluminum.

2.3.2 Protocol:

- 10 ml of each sample have been dried one night at 45 [ºC] in an oven with the vacuum open

- 5-10 [µg] of sample have been inserted in the DSC machine for the analysis
- As heating rate was used 10 [ºC/min] and the interval scanned was of 100 degrees centered on the theoretical expected T_g

T_g curves are reported in APPENDIX I, the final results are listed in Table 2-5

Table 2-5 T_g values for each sample

%MMA	T_g [ºC]
30	-12.3
50	17.3
60	35.7
70	54.4

3 SAMPLES CHARACTERIZATION:

3.1 Light scattering

Amongst many experimental techniques available to investigate colloidal systems and aggregation phenomena light scattering measurements are the most efficient in terms of accuracy and non-intrusiveness [10].
When particles are irradiated by electromagnetic waves of wavelength comparable or larger than the size of the particles themselves an oscillating dipole is formed. As the dipole changes they scatter the radiation in all directions (cf. Figure 3-1).

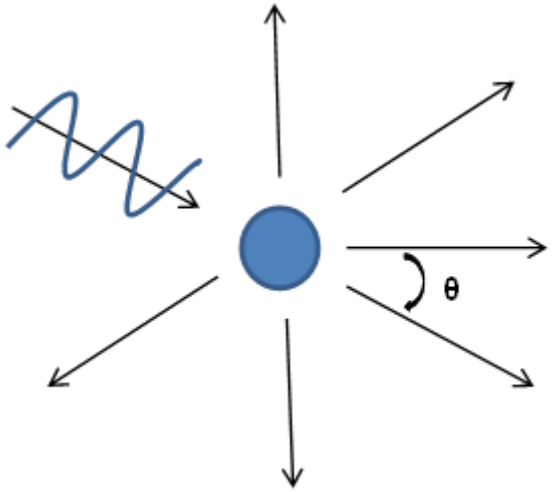

Figure 3-1 Incident light scattered by a particle

3.1.1 Static light scattering theory:

Static light scattering (SLS) is a light scattering technique that operates measuring the scattering intensity I, intended as the sum of all the radiations scattered by the element, at every angle θ and at a fixed distance from the scattering center.
From the spectrum analysis of the scattering intensity is then possible to gain crucial information regarding the dispersion and the aggregates structure, in fact I is sensitive in general to the particles size, structure…
At the basic of the conventional SLS theory for colloidal dispersion (Rayleigh-Debye-Gans) [11] there are the assumptions that electromagnetic radiations are identically scattered only once (the contribution of multiple scattering is neglected), only the

incident radiation is considered and the difference of refractive index between the particles and the medium is not too large.
Experimentally these conditions can be achieved working at very low concentrations.
Generally the intensity is expressed as function of the scattering wave vector in place of θ:

$$\vec{q} = \frac{4\pi n_0}{\lambda} \sin\theta \tag{3.1}$$

Where n_0 is the refractive index of the dispersion medium and λ is the radiation wave length in the vacuum. The importance of this vector is that its inverse $\vec{q}^{-1}$ represents the length scale of the scattering experiment.
The scattered intensity can be expressed as the product of different factors [1]:

$$I(q) = I_0 K_1 N V_p^2 P(q) S(q) = const\, P(q) S(q) \tag{3.2}$$

I_0 is the intensity of the incident radiation. K_1 is a constant which incorporates the dependence on the optical constants. N is the number of identical cluster per unit volume; V_p is the particle volume. $P(q)$, defined as form factor, describes the scattered intensity from a single primary particle and depends only on its shape and size; in case of spherical particles smaller at last ten times smaller than the wavelength of radiation the form factor is given by [1]:

$$P(q) = \left[\frac{3\,(\sin(qR_p) - qR_p \cos(qR_p))}{(qR_p)^3} \right]^2 \tag{3.3}$$

It is worth to point out that $\lim_{q\to 0} P(q) = 1$. $S(q)$, defined as structure factor, depends on the correlation among the particles in the aggregate: for primary particles it results everywhere $S(q) = 1$; for self-similar aggregates is valid in the fractal region $S(q) \sim q^{-d_f}$.

In general $I_0 K_1 N V_p^2$ is a constant: in case of primary particles, since at $q=0$ we have $P(q)=1$ and $S(q)=1$, it can be directly determined from the intensity profile $I(q=0)=I(0)=I_0 K_1 N V_p^2$; in case of cluster and poly-disperse cluster the quantity $I(0)$ must be in general extrapolated. Dividing $I(0)$ of primary particles by $I(0)$ allows determining $P(q)$.

In case of aggregation the structure factor $S(q)$ changes in times due to the growth in size and the change in structure of the aggregates. Dividing the scattering intensity spectrum by $P(q)$ allows to obtain the structure factor of the aggregate $S(q)$ and so indirectly from the power the fractal dimension.

Another very important quantity that can be obtained by the scattering profile is the radius of gyration R_g, defined as the sum of the squares of the distances of all the cluster particle from its mass center. It can be determined by a linear fitting of $I(0)$ using the so called Guinier plot analysis (cf. [11]):

$$\log\frac{I(q)}{I(0)} = \log(P(q)S(q)) = \log\left(1-\frac{1}{3}q^2R_g^2\right) \cong -\frac{1}{3}q^2R_g^2 \qquad (3.4)$$

Where the approximation $\log(1+x)\cong x$ has been used in equation (3.4).

Our analysis have been performed in MALVERN MASTERSIZER 2000, particularly several kinetics of aggregation in stagnant DLCA have been carried out.

3.1.2 Protocol:

Measurements of $P(q)$:

- Each sample was diluted in pure deionized water at $5\text{x}10^{-5}$ in volume fraction
- A proper amount of a 2 [M] NaCl solution was added to reach the final concentration of 10 [mM] NaCl

All the intensity data have been treated as previously explained in order to get the final expression of $P(q)$. 10 [mM] NaCl are experimentally suggested in order to reduce the Debye length of the cleaned samples and so to allow diffusion avoiding structure effects (In case of no salt the particles feel a too long range their mutual interaction and have less space in which can diffuse).

Aggregation kinetics:

- Each sample was diluted in pure deionized water (where previously air bubbles were removed) according to the final volume fraction and salt concentration
- The necessary amount of a 5 [M] NaCl solution (where previously air bubbles were removed) was poured into the latex solution

This protocol was adopted in order to avoid mixing the latex with a highly concentrated salt solution which could have induced locally fast aggregation, spoiling so the consequent kinetic measurements.
High final NaCl concentrations were used in order to have density matching between the solutions and growing aggregates preventing so sedimentation.

3.1.3 Dynamic light scattering theory:

In dynamic light scattering (DLS) measurements the scattered light intensity I is monitored at one fixed angle θ and at a fixed distance from the scattering center. More in detail, since the particles in the dispersion undergo to Brownian motion and so their mutual position change on a time scale, the observed scattering intensity exhibits fluctuations. From the rate of decay of these fluctuations information about the diffusion rate and so about the particles sizes (once the diffusion coefficient is known the hydrodynamic radius can be easily evaluated for spherical particles $R_h = \frac{k_B T}{6\pi\eta D}$) can be extracted; it is evident in fact that the more the particles diffuse and so the smaller they are, the higher will be the fluctuation frequency. Such

fluctuation can be analyzed defining a correlation function which takes into account the intensity self-correlation between time 0 and τ . This function is defined as follow:

$$g(\tau) = \frac{< I(q,0) I(q,\tau) >}{< I(q) >^2} = 1 + Ae^{-D\tau q^2} \quad (3.5)$$

Where A is a constant depending on the experimental set-up.

Once the correlation function is experimentally built D can be obtained by fitting with cumulant analysis the right member term expression with the left one.

Two different DLS machines were used: BROOKHAVEN and MALVERN ZETASIZER. The angles at which measurements were taken are respectively 90º and 173º. The same experimental protocol of SLS was used for DLS measurements.

3.2 Titration

3.2.1 Theory:

On the surfaces of our latex particles fixed negative charges (sulfate groups) are present as KPS was used during the polymerization.

By far the most commonly used method to count the number of fixed groups is provided by conductometric titration.

In fact for each acid site there is a corresponding H^+ associated. Measuring the amount of H^+ in the system gives the amount of sulfate groups and therefore the fixed charges amount.

In a conductometric titration a titrant (in our case NaOH) is added to the colloidal dispersion and the conductivity is monitored.

At first as the titrant is added, the conductivity decreases because the more conductive (mobile) ions H^+ are replaced by the less mobile Na^+ ions and then are neutralized with the OH^- ions.

Once all the ions H^+ associated with the surface groups are neutralized, further addition of base just increase the total electrolyte content of the solution leading to a raise in conductivity.

The breakpoint extrapolated from the two slopes gives the number of sulfate sites (the amount of titrant added is in fact known).

3.2.2 Protocol:

- 5 [g] of sample were diluted in 50 [g] of deionized water previously stripped with nitrogen (in order to avoid the effect of the eventually dissolved CO_2)
- 0.5 [ml] of 0.1 [M] solution of NaCl were added in order to promote the replacement mechanism. At each step 0.05 [ml] of a 10 [mM] NaOH were added to the solution and then the conductivity was measured

During all the titration time the samples were gently stirred and continuously stripped with nitrogen.
The results of the titrations are reported in Table 3-1

Table 3-1 Surface charges for each sample

%MMA	σ_{SO4} [mol $H^+/Kg_{Polymer}$]
30	0.01607
50	0.00896
60	0.01064
70	0.00931

3.3 ζ-potential

3.3.1 Theory:

If an external electric field is applied to charged particles in dispersion, phenomena associated with the relative movement of charges (i.e. electrokinetic) are possible. These phenomena are referred to as electro-osmosis, if the liquid moves and the solid is stationary, and electrophoresis, the opposite phenomenon [10].

If the particle size is larger than the double-layer thickness and a coordinate system referred to the solid particle is chosen electro-osmosis and electrophoresis can be described essentially as the same phenomenon. Only one description is so required and electro-osmosis will serve the purpose [10].

In details a double-layer thickness much smaller than the particle size allows to approximate the particle surface as a flat one (cf. Figure 3-2); considering then a coordinate system referred to the solid particle allow to consider the liquid in motion around it.

The final objective of this representation is to derive an expression for the velocity profile v on the particle surface and in particular its value in bulk V_e .

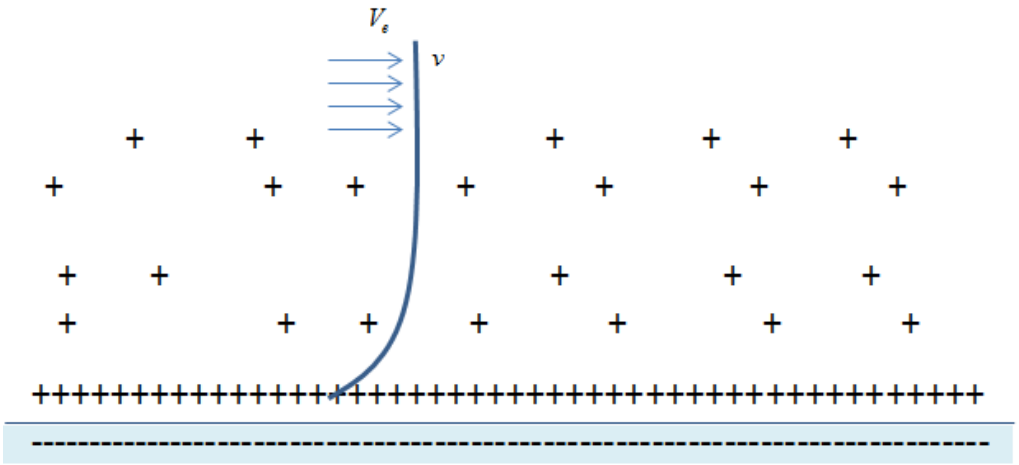

Figure 3-2 Velocity profile on a negatively charged particle surface. In the inner part of the double layer were counter ions are fixedly adsorbed on their correspondent ions (slip plane) the velocity profile is zero and the potential is equal to the value of the ζ-potential.

It can be demonstrated [10] that this is given by:

$$V_e = \frac{\varepsilon \zeta E}{\eta} \tag{3.6}$$

Where ε is the dielectric constant, η the medium viscosity, E the intensity of the electric field and ζ is the so called ζ-potential. The ζ-potential is the value of the potential very close to the particle surface (slip plane) where the velocity profile is equal to zero.

Changing coordinate system from the solid particles to the continuum medium leads to find particles moving by effect of the electric field at speed $V_p = -V_e$.

This velocity or more exactly the electrophoretic mobility $u = \frac{V_p}{E}$ (so also the ζ-potential) can be directly measured by combining DLS and electrophoresis techniques.

In our case was used a MALVERN ZETASIZER.

3.3.2 Protocol:

- The necessary amount of each sample was diluted at 1x10^{-5} volume fraction and at the target salt concentration of NaCl mixing at first the salt with water and then adding the latex.
- In case of measurements at 45 [ºC] the samples were pre-heated in an oven and equilibrated for 5 minutes in the Zetasizer

Results are listed in Table 3-2 and Table 3-3

Table 3-2 ζ-potential values at 10 [mM] NaCl

%MMA	**ζ-potential [mV]**	
	25[ºC]	**45 [ºC]**
30	-73.23	-62.66
50	-57.8	-55.6
60	-59.8	-61.66
70	-45.8	-55.16

Table 3-3 ζ-potential values at 140 [mM] NaCl

%MMA	ζ -potential [mV]	
	25[ºC]	**45 [ºC]**
30	-42.26	-40.13
50	-33.9	-30.5
60	-31.33	-28.76
70	-27.63	-26.4

3.4 Rheometer

3.4.1 Theory:

A rheometer is a device capable of applying controlled shear to a colloidal dispersion. Our instrument consisted in an outer rotating cup and an inner fixed cylinder (cf. Figure 3-3). This particular configuration, referred to as Couette geometry, was employed because it guarantees to obtain between the moving and fixed solid surfaces a steady laminar and isothermal flow of the dispersion [12].

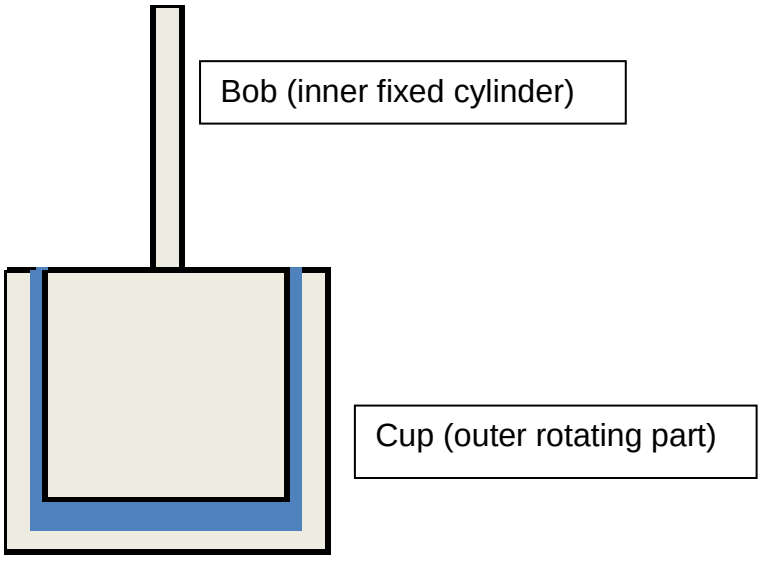

Figure 3-3 Schematic of a rheometer Couette geometry. The sheared dispersion (blue) lies between the cup (outer rotating part) and the bob (fixed inner cylinder).

In detail a rheometer measures the angular deflection of the fixed part which indicates the torque on the bob.
By measuring this stress the viscosity of the system can be easily monitored on time, for Newtonian fluid is valid in fact [12]:

$$\tau_{shear} = \eta\dot{\gamma} \tag{3.7}$$

Where τ_{shear} is the shear stress. For non-Newtonian fluids relations similar to equation (3.7) are available in the literature.
An ARES rheometer was used for the analysis. The temperature was controlled with a thermal bath. The outer fixed part diameter was 33.3 [mm], the inner cup diameter was 34 [mm]. A gap of 3 [mm] from the bottom of the rotating cup was used in order to avoid border effects. Since aggregation alone under shear can occur on very large time scales small amount of salts were added to fasten the process.

3.4.2 Protocol:

- The sample were diluted at first with the proper amount water and then with a 2 [M] NaCl solution in order to reach a final dry content and the target salt concentration
- After mixing the latex with the salt solution the size was checked in DLS and if no variations were observed the analysis were started

The rheometer turned up to be a very sensitive system. In order to achieve reproducible experiments a very strict cleaning procedure must be followed:

- Wash the cup and bob with deionized water and soap
- Wash the cup and bob with methyl-ethyl-ketone
- Clean the cup and bob with deionized water and soap
- Keep the cup and bob in 0.5 [M] H_2SO_4 solution for at least 10 minutes
- Wash the cup and bob with deionized water and soap
- Dry the cup and bob with nitrogen

4 RESULTS AND DISCUSSION

The present work purpose is to understand the role that coalescence plays in the aggregation under shear.

In general sheared dispersions are a very complex system to analyze; their aggregating behavior involves several physical phenomena: the particles are diffusing immersed in an external speed field and are interacting with one another according to the attractive and repulsive forces they are subjected to (i.e. their interaction potential).

Therefore, it was initially necessary to understand their interaction potential in stagnant conditions and only later shear conditions were explored.

In particular, aggregations induced by salt (NaCl) were performed in stagnant DLCA conditions at different latexes volume fractions (φ=1-3x10^{-5} and 0.05-0.1)and temperatures (25-45 [ºC]).This temperature range was examined as it enabled coalescence (which occurs only above the material glass transition temperature) for some of the samples (cf. Table 2-5). Low volume fractions were tested since smaller particles concentration increase the characteristic time of aggregation (cf. equation(1.34)) and allow to clearly observe the effects of coalescence ($\tau_{coal} << \tau_{agg}$). Higher volume fractions were analyzed, although the characteristic time of aggregation ($\tau_{coal} >> \tau_{agg}$) is very small in those cases, in order to elucidate the mechanism of gelation of different samples in stagnant conditions. Note that comparable particle volume fractions were then employed in shear conditions.

The RLCA experiments were performed in order to better understand the role and nature of the particle interaction potential on particle aggregation. Surface charge, ζ-potential and light scattering measurements were performed in order to deepen this point.

Finally shear aggregations were performed in the rheometer with a fixed dry content (DC=5%) and shear rate (4900 [1/s]); in these conditions the salt concentration and temperature were changed in order to clarify the interplay of coalescence and aggregation.

4.1 Stagnant Aggregation

4.1.1 DLCA:

4.1.1.1 Characterization at low volume fractions:

The interplay between coalescence and aggregation was at first investigated in DLCA by carrying out several salt-induced aggregation kinetics in the small angle static light scattering at φ=1x10^{-5}, 2x10^{-5}, 3x10^{-5}. The SLS temperature and final NaCl concentration were in all cases respectively 30 [ºC] and 4 [M] (This high salt concentration was employed in order to have density matching between the solution and the aggregates, avoiding their sedimentation). The results of the aggregation kinetics (in terms of gyration radius R_g versus time) are reported in Figure 4-1, Figure 4-2 and Figure 4-3.

Working at low primary particles concentration increases the characteristic time of aggregation.

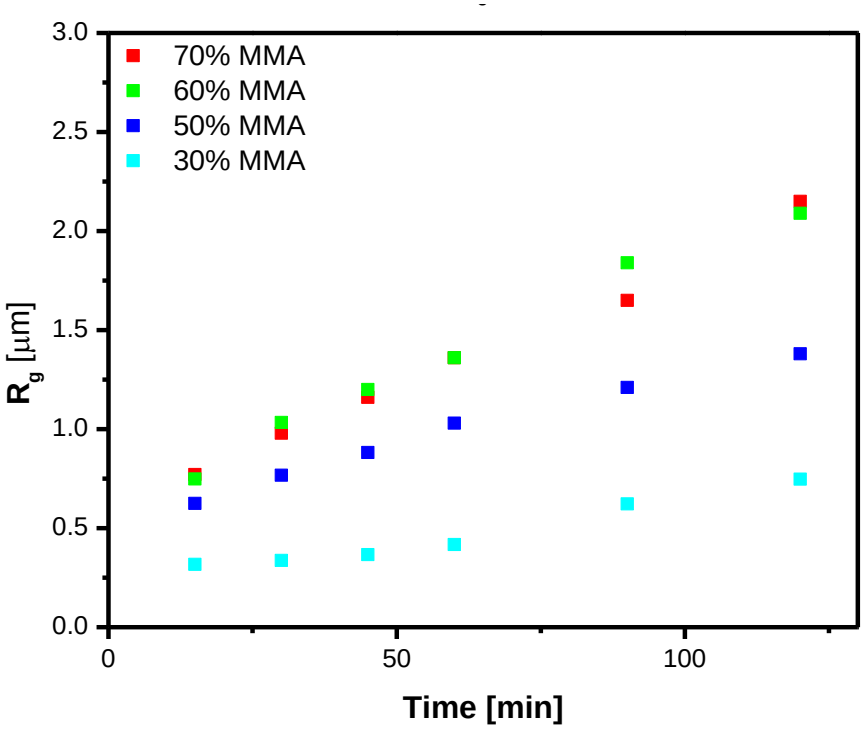

Figure 4-1 Gyration radii evolutions of 70-30% MMA samples as function of time at φ = 1x10^{-5}

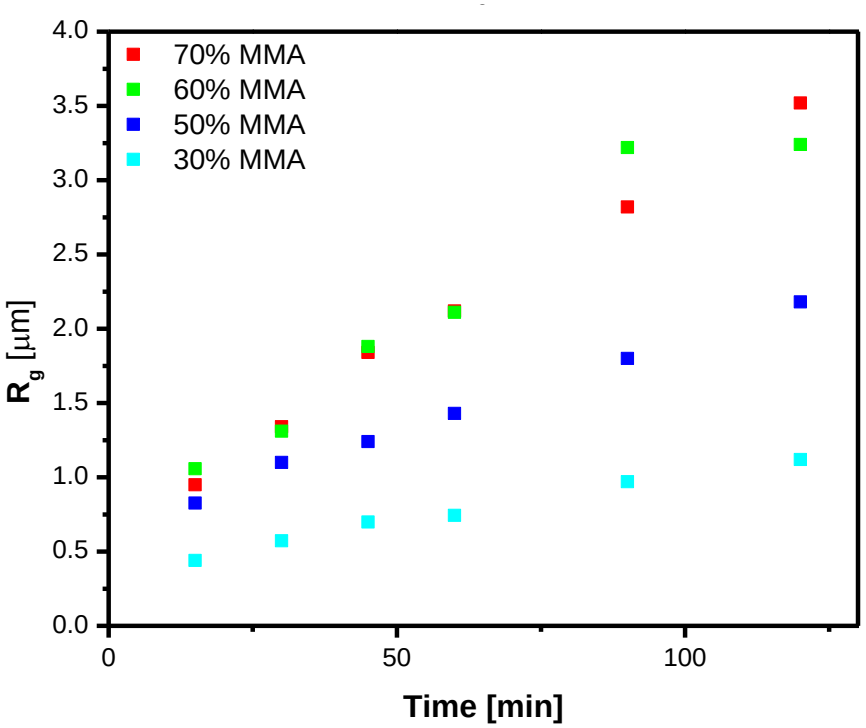

Figure 4-2 Gyration radii evolutions of 70-30% MMA samples as function of time at $\varphi = 2x10^{-5}$

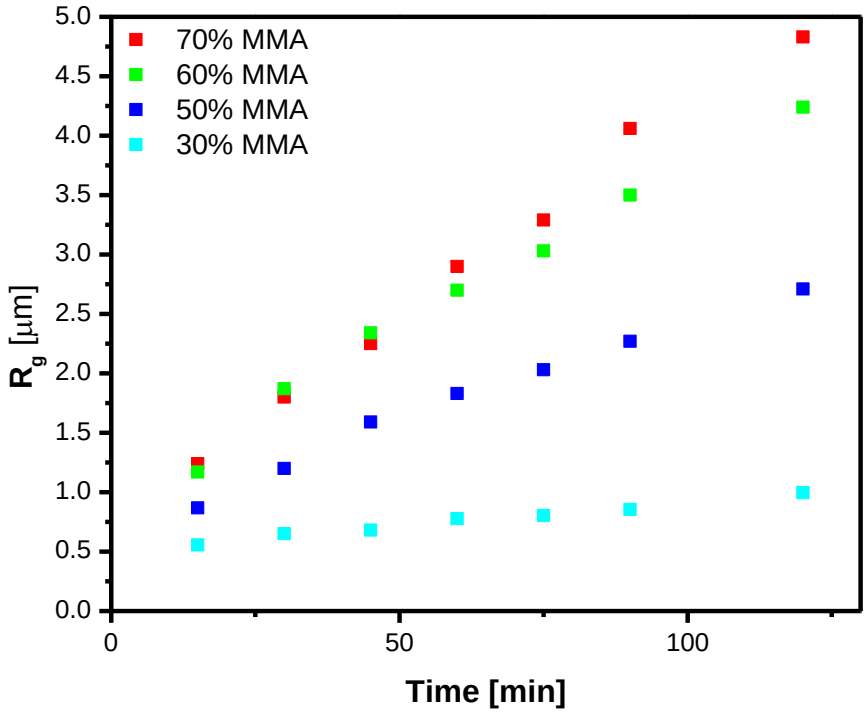

Figure 4-3 Gyration radii evolutions of 70-30% MMA samples as function of time at $\varphi = 3x10^{-5}$

In particular in DLCA τ_{agg} can be evaluated since in equation (1.34) W is equal to one:

$$\tau_{agg} = \frac{W}{\beta^{DLCA} N_0} = \frac{1}{\beta^{DLCA} N_0} \tag{4.1}$$

Table 4-1 τ_{agg} values evaluated at $\varphi =$ 1x10^{-5}, 2x10^{-5}, 3x10^{-5}

φ	τ_{agg} [s]
1x10^{-5}	45
2x10^{-5}	22
3x10^{-5}	15

Increasing the characteristic aggregation times allows the particles in the aggregates (if they can) to coalesce ($\tau_{coal} \ll \tau_{agg}$). The main effect of coalescence during these aggregation kinetics would be the formation of spherical-similar aggregates (d_f =2.4 – 3) with smaller gyration radii compared with the non- coalescing ones.

Focusing on the gyration radii it can be seen from Figure 4-1, Figure 4-2 and Figure 4-3 that the 70% MMA and 60% MMA ones completely overlap.

Notably, the 70% MMA and 60% MMA particles at these experimental conditions are below their T_g (cf. Table 2-5) and so exhibit hard-solid material features, in particularly their viscosity diverges to infinite. As a consequence their corresponding characteristic times of coalescence, defined in equation (1.36), diverge to infinite and coalescence cannot occur. These gyration radii are therefore evolving at the maximum rate according to the DLCA aggregation regime.

Figure 4-1, Figure 4-2 and Figure 4-3 show that the 50% MMA and 30% MMA radii of gyration are progressively smaller than the 70% MMA and 60% MMA ones. Notably the 50% MMA and 30% MMA particles at these experimental conditions are above their T_g (cf. Table 2-5) and so behave like viscous fluid with a well-defined and progressively lower viscosity. Therefore coalescence occurs for these samples: as expected the higher the BA content, the faster coalescence occurs.

Additional evidences for the 50% MMA and 30% MMA particles coalescence can be gained looking at a more universal behavior of the aggregating system: introducing the dimensionless time defined as

$$t_{ad} = \frac{t}{\tau_{agg}} = N_0 \frac{8}{3} \frac{k_B T}{\eta} \frac{t}{W} \tag{4.2}$$

it results from the literature [13] [14] that when the aggregates radii are plotted against the dimensionless time defined in equation (4.2) independently of temperature, primary particles concentration N_0 and stability W, they collapse to form a unique curve known as master curve [14]. In particular, this universal behavior can be appreciated for DLCA aggregating system looking at the PBE dimensionless equations:

$$\frac{dX_i}{dt_{ad}} = \frac{1}{2} \sum_{j=1}^{i-1} B_{i-j,j} X_{i-j} X_j - X_i \sum_{j=1}^{\infty} B_{i,j} X_j \tag{4.3}$$

where

$$X_i = \frac{N_i}{N_0} \tag{4.4}$$

$$B_{ij} = \frac{1}{4} (i^{\frac{1}{d_f}} + j^{\frac{1}{d_f}})(i^{-\frac{1}{d_f}} + j^{-\frac{1}{d_f}}) \tag{4.5}$$

As in DLCA conditions the fractal dimension is fixed once the particle size is defined [15], it results that the dimensionless CMD (and therefore all resulting averages) are the same for all the aggregation processes, disregardful of particle concentration and temperature.

As comparable sizes lead to similar fractal dimensions and the number of primary particles per cluster is the same, overlapped gyration radii should be obtained according to the fractal scaling expression (cf. with equation (1.26)):

$$< i >= k_f (\frac{< R_g >}{a})^{d_f} \quad (4.6)$$

where $k_f = 4.46 d_f^{-2.08}$ depends only on the fractal dimension and not on the material [16].

Figure 4-4 reports all the gyration radii kinetics at $\varphi = 1x10^{-5}$, $2x10^{-5}$, $3x10^{-5}$ plotted against the dimensionless time. As it is shown, for each sample the gyration radii are overlapped regardless of the volume fraction. As expected the 70%MMA and 60%MMA gyration radii are superimposed while the 50%MMA and 30%MMA ones remain lower: once more this indicates how coalescence becomes more relevant while increasing the BA content.

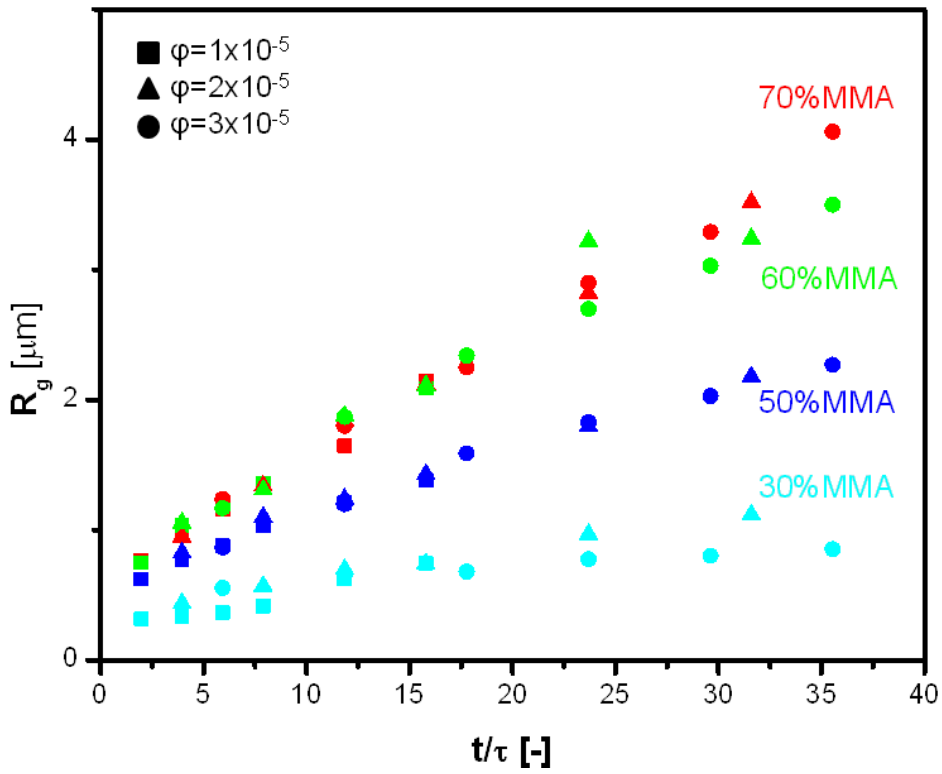

Figure 4-4 Aggregation kinetics of 70-30% MMA samples as function of dimensionless time at different volume fractions $\varphi = 1x10^{-5}$, $2x10^{-5}$, $3x10^{-5}$

Further insights about coalescence can be gained looking at the structure of the aggregates from SLS fractal dimension measurements.

As previously discussed d_f values can be obtained by the SLS intensity curve in the fractal region with the relation $S(q) \sim q^{-d_f}$.

At the beginning of each aggregation, due to the very low concentrations, self-similar structures were not yet formed so fractal dimensions increasing in time were found. When finally fractal aggregates were formed, fractal d_f constant in time were found. These values are reported in Table 4-2. Moreover due to the very low volume fractions in case of the 30% MMA kinetics the $S(q)$ analysis could not be performed since the coalesced particles were too small and consequently the fractal region was not large enough to extract safely d_f values. As shown in [17] another method to obtain d_f is available: it consists in plotting on a logarithmic graph $I(0)$ and R_g respectively as y-axis and x-axis and extracting d_f as the value of the exponent in a power regression between these data ($I(0)$ vs. R_g plots are reported in APPENDIX II). d_f values extracted with both methods are listed in Table 4-2.

Table 4-2 Values of d_f from $<S(q)>$ and $R_g - I(0)$ analysis:

d_f						
Φ	$1x10^{-5}$		$2x10^{-5}$		$3x10^{-5}$	
SAMPLE	$<S(q)>$	$R_g - I(0)$	$<S(q)>$	$R_g - I(0)$	$<S(q)>$	$R_g - I(0)$
30%MMA	-	2.45	-	2.33	-	2.98
50%MMA	1.77	1.77	1.8	1.78	1.8	1.86
60%MMA	1.73	1.86	1.74	1.73	1.78	1.87
70%MMA	1.81	1.77	1.8	1.87	1.8	1.72

d_f values obtained with the $S(q)$ analysis are generally comparable with the $I(0)$ vs. R_g ones. In case of the 30% MMA were found $d_f > 2.3$, additional evidences that coalescence occurs for this sample.

The only critical issue are the 50%MMA d_f: these d_f are comparable with the 60%MMA and 70%MMA. If coalesce occurs for this sample, as previously discussed,

higher d_f would be expected. This inconsistency can be explained with a lag time between coalescence and the d_f measured. At the beginning of the sintering the 50%MMA aggregates present a very open branched structure according to the DLCA regime; coalescence occurs on the ramified aggregates branches shrinking them and so decreasing the relative gyration radii. This internal restructuring which strongly affect the gyration radii slowly changes the overall structure which results therefore in time only slowly increasing in d_f (cf. Figure 4-5).

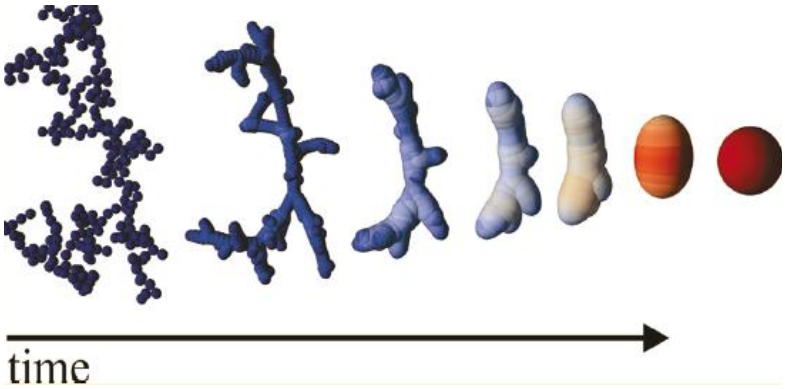

Figure 4-5 Depiction of the internal coalescing aggregates restructuring: the radius of gyration changes faster than the overall aggregate shape. Picture taken from [18]

For the 30%MMA this lag time between coalescence and the d_f measured has not been observed. The reason is that the sample characteristic time of coalescence is much smaller than the 50% one and so a faster coalescence occurred.

Faster coalescence occurs the higher the sample temperature overshoots its T_g until eventually a maximum final rate is reached. The reason is due to the viscosity which plays a crucial role in the characteristic time of coalescence (cf. equation (1.36)): as the temperature increases the particles viscosity decreases reducing the characteristic time of coalescence.

In order to prove the previous statement, several salt-induced aggregation kinetics were performed in the DLS at $\varphi =$ 1x10^{-5} and 4 [M] NaCl. Our available DLS device allowed investigating the temperature range [25-45ºC]. In these conditions only the 30%MMA, 50%MMA and 60%MMA samples were tested since, according to their

relative T_g plot listed in APPENDIX I, are the only ones at which the glass transition occurs. The respective results (in terms of hydrodynamic radius R_h versus time) are reported in Figure 4-6, Figure 4-7, Figure 4-8.

As consequence of faster coalescence, Figure 4-7 shows that increasing the 50%MMA sample temperature over its T_g value (17 [°C]) leads to a progressively smaller hydrodynamic radii evolution.

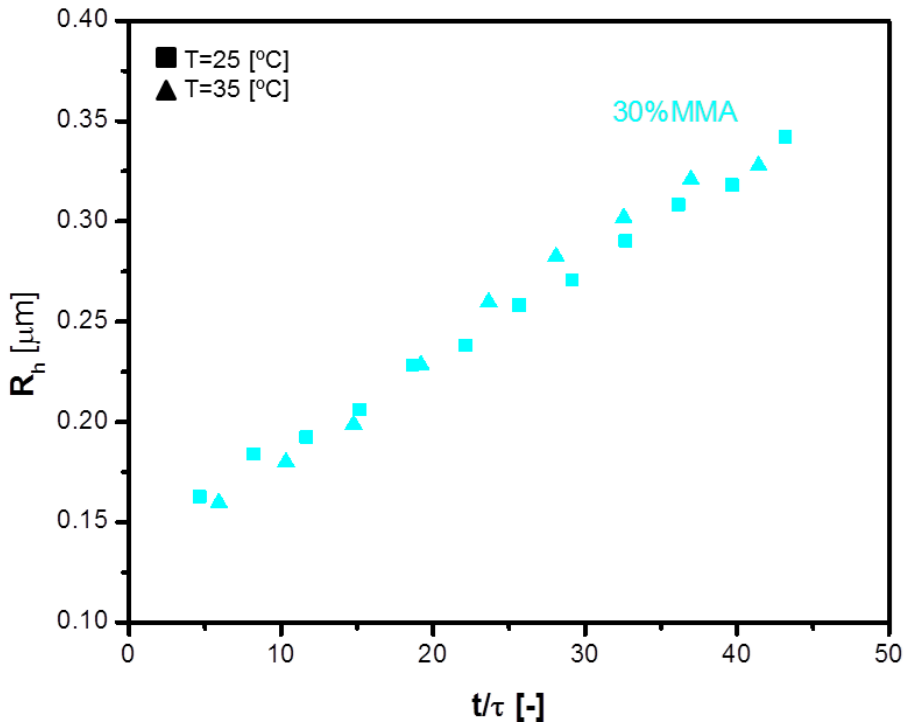

Figure 4-6 30% MMA hydrodynamic radii evolutions as function of dimensionless time at different temperatures [25-35º] and at volume fraction $\varphi = 1\text{x}10^{-5}$

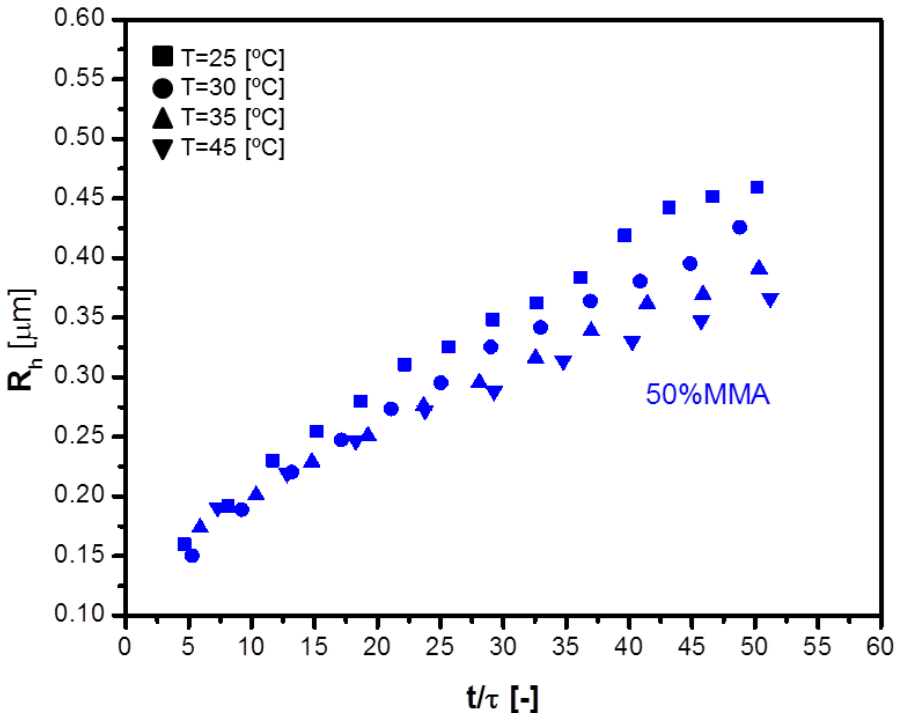

Figure 4-7 50% MMA hydrodynamic radii evolutions as function of dimensionless time at different temperatures [25-45º] and at volume fraction $\varphi = 1x10^{-5}$

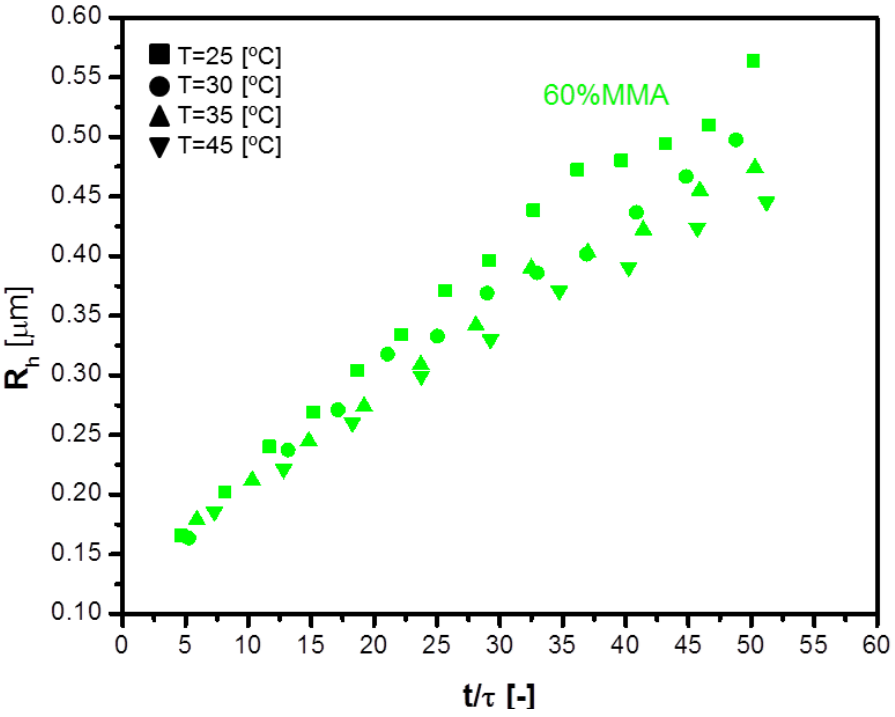

Figure 4-8 60% MMA hydrodynamic radii evolutions as function of dimensionless time at different temperatures [25-45º] and at volume fraction $\varphi = 1x10^{-5}$

A similar trend it is observed for the 60%MMA sample in Figure 4-8. In this case it is worth to point out that below the 60%MMA T_g (35 [°C]) the corresponding hydrodynamic radii are not overlapped. The reason is that the glass transition does occur in a region of temperature centered around the glass transition temperature and not at single fixed temperature as for example for a phase transition. In this region therefore the particles viscosity can be well defined even below the T_g value.

Figure 4-6 exhibits the maximum rate of coalescence which is reached once the hydrodynamic radii coalesce at their maximum speed rate. This maximum rate of coalescence it is reached only by the 30%MMA since at the experimental condition investigated is already fully coalesced (T_g =-12 [°C]).

Further information about the samples relative rate of coalescence can be obtained comparing the 30%MMA, 50%MMA and 60%MMA aggregation kinetics (cf. Figure 4-9). The 50%MMA hydrodynamic radii at 45 [°C] are superimposed with the 30%MMA ones. This means that the 50%MMA sample in this condition is coalescing at the same rate of the 30%MMA. Therefore these two samples become comparable from the coalescence point of view only over 45 [°C].

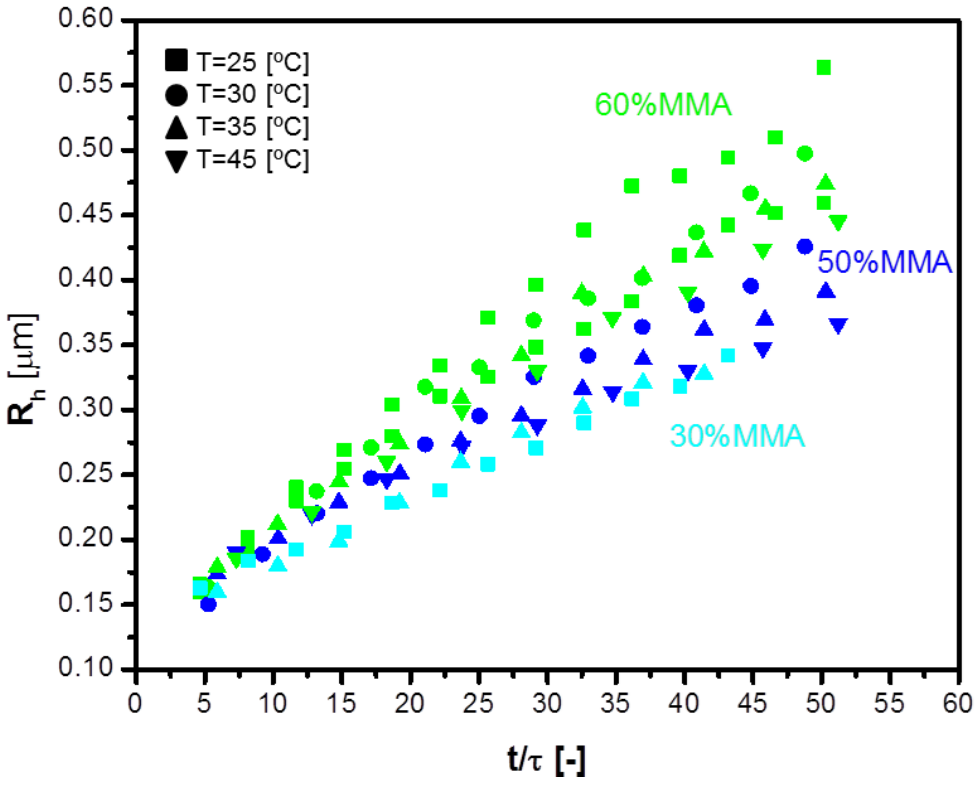

Figure 4-9 30%-60%MMA hydrodynamic radii evolutions as function of dimensionless time at different temperatures [25-35°] and at volume fraction $\varphi = 1x10^{-5}$

Finally, since it has been figured out that the 30%MMA and 50%MMA samples at 30 [°C] are coalescing, hypothesis concerning the respective characteristic times of coalescence can be formulated (only hypothesis can be put forward due to the nature of equation (1.36) which results only as proportional relation and therefore does not allow exact evaluations). These characteristic times can be inferred looking at the characteristic time of aggregation listed in Table 4-3. As the 30%MMA sample is clearly fully coalescing, it is clear that its characteristic time of coalescence has to be lower than 15 seconds (as it manages to coalesce even in this case). On the other side as the 50%MMA is only partially coalescing even at φ=1x10^{-5}, its characteristic time of coalescence has to be higher than 45 seconds.

A physical evidence to these assumed values can be provided by evaluating the particles viscosities. Due to the proportional nature of equation (1.36) this can be carried out only with a magnitude order magnitude approach, assuming for simplicity equation (1.36) as strict equality and a fixed particles surface tension (for PMMA 22.69 [mN/m] [19]). Postulating for the 30%MMA and 50%MMA samples as characteristic times of coalescence respectively 1-15 [s] and 60-120 [s], the corresponding particles viscosities result 1.13x10^{5}-1.7x10^{6} [Pa s] and 6.8x10^{6}-1.36x10^{7} [Pa s]. Since the obtained viscosities are consistent with typical values reported in the literature [20], the coalescence characteristic times might actually lie around the suggested values.

4.1.1.2 Characterization at high volume fractions:

In order to investigate the gelation of the particles, salt-induced aggregation kinetics were carried out in DLCA conditions at high latexes volume fractions (0.05-0.1) for all the samples. At high particles concentrations aggregation becomes the most dominant phenomenon ($\tau_{coal} >> \tau_{agg}$) and typically ends up in gels formations. In our particular conditions the characteristic times of aggregation τ_{agg} (evaluated through equation (4.1)) are as expected very small (in the range 9x10^{-3}-4x10^{-3} [s]). It is therefore reasonable to neglect coalescence in these experiments, as for the particles characteristic times to be so small, the particles should have viscosities in the order of 9x10^{2}-2x10^{3} [Pa s].

Experimentally 3 [ml] of 5 [M] NaCl solution were poured into 3 [ml] of the high DC purified latexes at 25 [ºC]. Depending on how the salt solution was poured into the

latexes two results were obtained: if the salt solution was slowly poured into the latexes leaving it diffusing through, gel formation occurred for all the samples; if the salt solution was rapidly poured into the latexes, gel formation occurred for the 30%MMA and 50%MMA samples but not for the 60%MMA and 70%MMA ones for which only large aggregates were found. Furthermore, once formed, these 60%MMA and 70%MMA gels were very weak and if mildly agitated showed to break. The broken gel aggregates were diluted and measured in the SLS; $d_f = 2.5$ were found, meaning that the clusters were rearranging in more compact structures. On the other hand the 50%MMA and 30%MMA gels proved to be very compact regardless the pouring method used.

Since at 25 [ºC] the 30%MMA and 50%MMA particles are both above their respective T_g (cf. Table 2-5)coalescence can occur. In these conditions the 30%MMA and 50%MMA particles behave slightly viscously and, when aggregation is induced, can partially interpenetrate with one another, sticking and forming resistant aggregates. On the contrary the 60%MMA and 70%MMA particles at 25 [ºC] are both below their respective T_g (cf. Table 2-5), coalescence cannot occur and at the minimum stress the aggregates undergo breakage.

Therefore, in spite of the fact that at high volume fraction $\tau_{coal} >> \tau_{agg}$, the role of coalescence is very important as it affects the gel strength/weakness (particularly note that this fact has to be carefully considered when studying the gelation of the particles in shear).

As additional experiment, the 60% MMA high DC sample was heated up to 45 [ºC] (60%MMA $T_g = 35$ [ºC]) and the 5 [M] NaCl solution was rapidly poured into the latex. In these conditions a strong gel was formed and maintained its structure also when the sample was cooled to room temperature.

4.1.2 RLCA

Before investigating shear conditions it was required to elucidate how our particles basically behave when there is no imposition of an external velocity field but repulsive interactions are present (stagnant RLCA).

Assuming our particles undergoing DLVO interactions, at first it will be discussed how the van der Waals and the electrostatic forces affect our samples potential energy barrier, then the effect of the electrostatic forces on the samples stability will be clarified.

Several analytical solutions for Van der Waals interaction potential energies are available in the literature [10]; in general they always take the form $V_A = -A \cdot f(geometry)$,where A is the Hamaker constant. The value of A, 1.05x10^{-20} [J] for PMMA dispersions in water [10], does not depend on the samples composition. This can be estimated through the Lifshitz theory of macroscopic Van der Waals interaction in the simplest case of slabs of two identical material 2 interacting across a medium 1 [10, 21] (McLachlan equation):

$$A = \frac{3k_B T}{4}\left[\frac{\varepsilon_2 - \varepsilon_1}{\varepsilon_2 + \varepsilon_1}\right]^2 + \frac{3h\omega}{32\pi\sqrt{2}}\frac{(n_2^2 - n_1^2)^2}{(n_2^2 + n_1^2)^2} \qquad (4.7)$$

Where ε_i are the static dieletric constant, n_i the refractive indices in the visible range, h is the Planck constant and ω is the UV peak absorption frequency.

Since our PMMA samples dielectric constants, refractive indexes and UV peak absorption frequencies in equation (4.7) are similar, the value of A can be assumed as composition independent. The geometry is given by the one of the interacting system and for each of our samples results the same (sphere).

Therefore since both the geometry and Hamaker constant do not differ changing the samples compositions, the Van der Waals interactions affect our samples interaction potentials energies in the same way.

On the other side the impact of the electrostatics on our samples energetic barriers can be directly experimentally evaluated. This was carried out by particle surface charges (cf. Figure 4-10) and ζ-potential (cf. Figure 4-11) measurements.

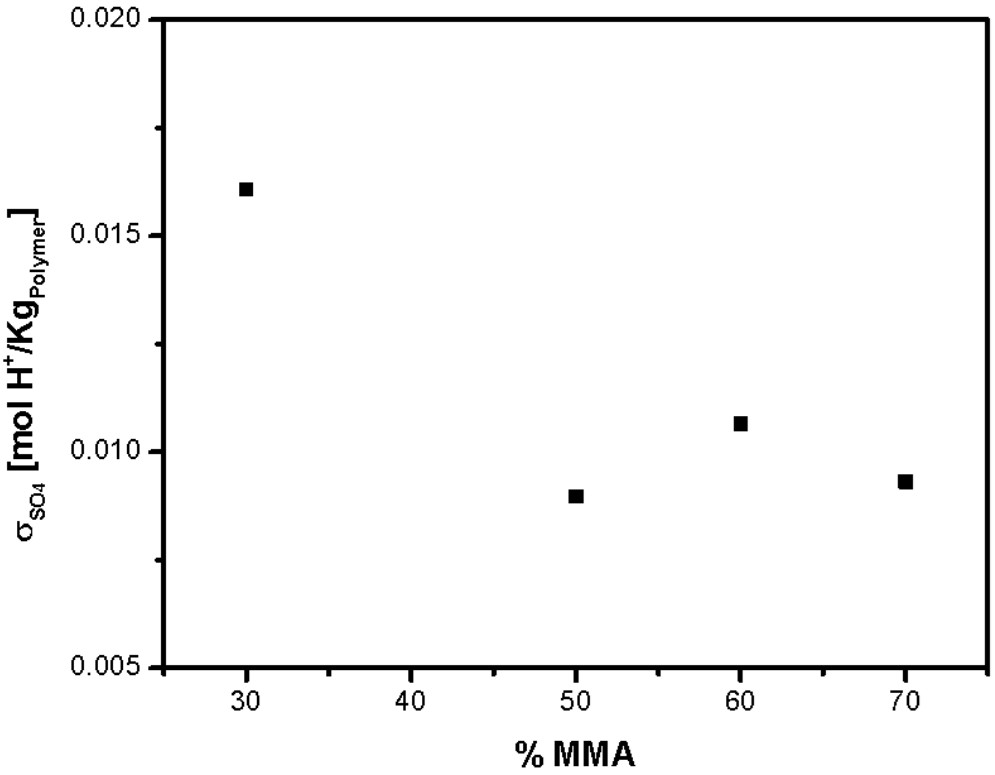

Figure 4-10 Absolute values of the surface charge density as function of the %MMA

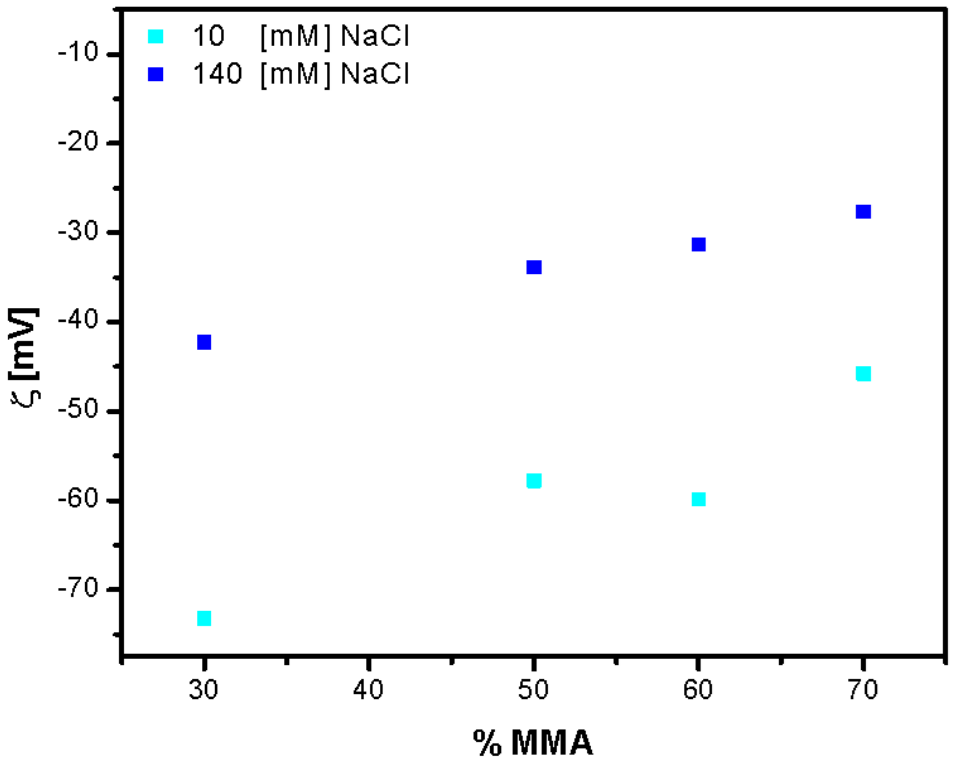

Figure 4-11 ζ-Potential at 25 [ºC] as function of the %MMA measured at $\varphi = 1x10^{-5}$ with 10 [mM] NaCl (light blue) and 140 [mM] NaCl (dark blue). Increasing the salt concentration leads to a lower absolute value of the potential.

From Figure 4-10 can be observed that the samples exhibit different surface charges densities; more in detail the trend seems to be the higher the BA%, the higher the surface charge density; such a behavior can be explained as the effect of different hydrophobicity-hydrophilicity values for the MMA and BA (the solubility at 20 [ºC] in water are respectively 16 [g/L] and 2 [g/L] [22] [23]). During the polymerization, which involves a homogenous nucleation mechanism, growing oligoradicals chains are formed; the length at which these chains precipitate on the particles nuclei is given by their solubility in water: the lower it is, the sooner they will precipitate. If long chains are formed the KPS, which is attached at one of the end, will remain wrapped inside and lower surface charges are found. Since according to the solubility the MMA forms longer chains than the BA, less charged groups are expected to be found for the rich %MMA samples.

The surface charges differently affect the total interaction potential energies shapes. In particular, the larger they are, the more the particles repel each other and therefore the higher the absolute maxima values V_m.

This can be further appreciated by measuring the samples ζ-potential. The ζ-potential values reported in Figure 4-11 result different from one sample to the other and follow the same trend of the corresponding surface charges (cf. with Figure 4-12). Note that experimentally ζ-potential measurements have to be performed at very low salt concentrations (10 [mM]). The higher salt concentration (140 [mM]) was tested since comparable ones were employed in shear conditions. As expected increasing the salt concentration leads to a lower absolute value of the potential but only slightly affects the trend between the samples which remains in the experimental error similar.

In general higher absolute values of potential energy barriers result in higher stability. The samples stability was determined by measuring the samples critical coagulation concentration (cf. Figure 4-13) and by calculating the corresponding Fuchs stability ratios (cf. Figure 4-14).

Several aggregation kinetics (reported in APPENDIX III) were run in the DLS at 25 [ºC] with $\varphi = 1\text{x}10^{-5}$ starting from high NaCl concentrations which were progressively decreased. In DLCA where W=1 the rate of aggregation is the fastest and all the aggregation kinetics overlap; as soon as the RLCA regime is entered the aggregation kinetics are slower and do not overlap any more with the DLCA ones.

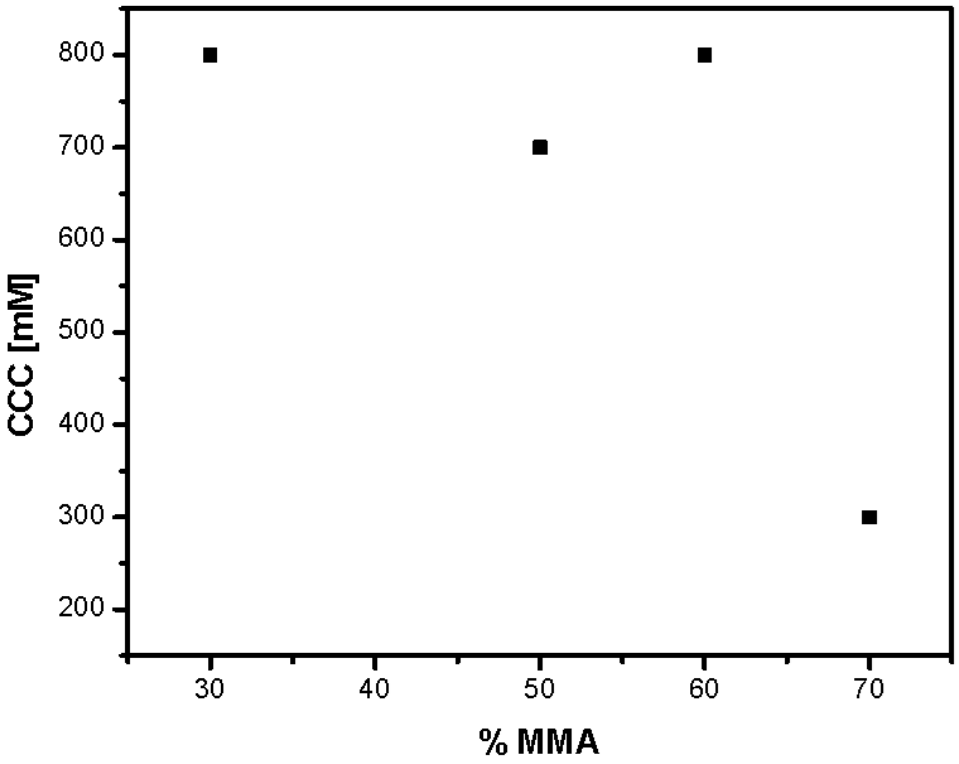

Figure 4-13 Values of the critical coagulation concentration as function of the MMA% measured at $\varphi = 1x10^{-5}$ and 25 [ºC]

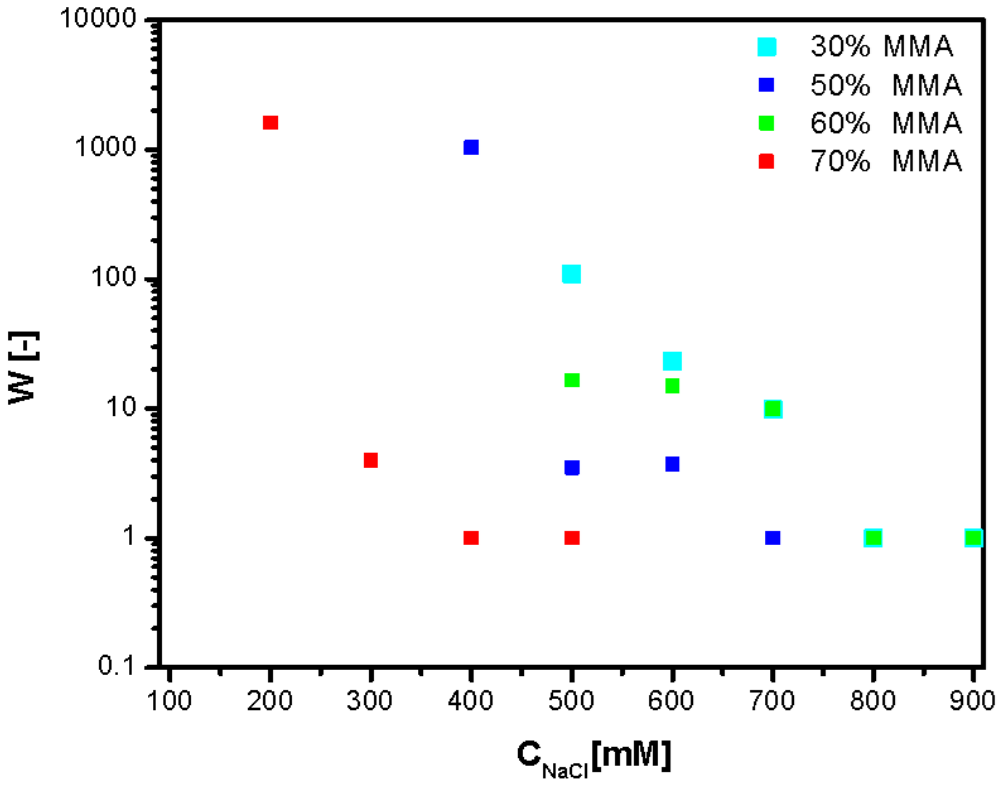

Figure 4-14 Values of the Fuchs stability ratio as function of the NaCl concentration and MMA% at $\varphi = 1x10^{-5}$ and 25 [ºC]

The CCC was determined as the lowest salt concentration at which the aggregation curves were found to be overlapped.

The Fuchs stability ratios were evaluated by fitting the aggregation curves according to the mathematical model and numerical methods described in [24], [14], [25], [26].

If the electrostatic contributes (Figure 4-10 and Figure 4-11) are compared with the overall potential ones (Figure 4-13 and Figure 4-14), similar trends can be observed. Nevertheless as shown in Figure 4-13 and Figure 4-14 increasing the %MMA content from 60% to 70% reveals a catastrophic loss in stability for the MMA rich samples. This loss of stability cannot be explained only in terms of electrostatics since the respective surface charges and ζ-potential values are comparable for all the samples, and might be ascribed to a material effect or a non-DLVO contribution (cf. [10]).

4.2 Shear Aggregation

At last, once the behaviors of our samples were clarified in stagnant, the interplay between coalescence and aggregation was investigated in shear conditions.

In order to discuss our results, it is necessary to understand the shear induced aggregation mechanism; this can be done by introducing the characteristic time of aggregation in shear, which by combining equation (1.32) with equation (1.34) results:

$$\tau_{agg} = \frac{W}{\beta^{DLCA} N_0} \propto e^{\frac{V_m}{k_B T} - 2\alpha Pe} = e^{\frac{V_m - 6\eta\pi a^3 \dot{\gamma}}{k_B T}} \tag{4.8}$$

If shear is introduced into the system the characteristic time of aggregation depends on the competition between the interaction potential and the shear destabilizing effect.

To better explain the physical meaning of equation (4.8) it is possible to plot the aggregation rate constant as a function of the Peclet (*Pe)* number (cf. Figure 4-15).

Figure 4-15 shows that two limit regimes are possible: at low Peclet numbers *Pe*<<1

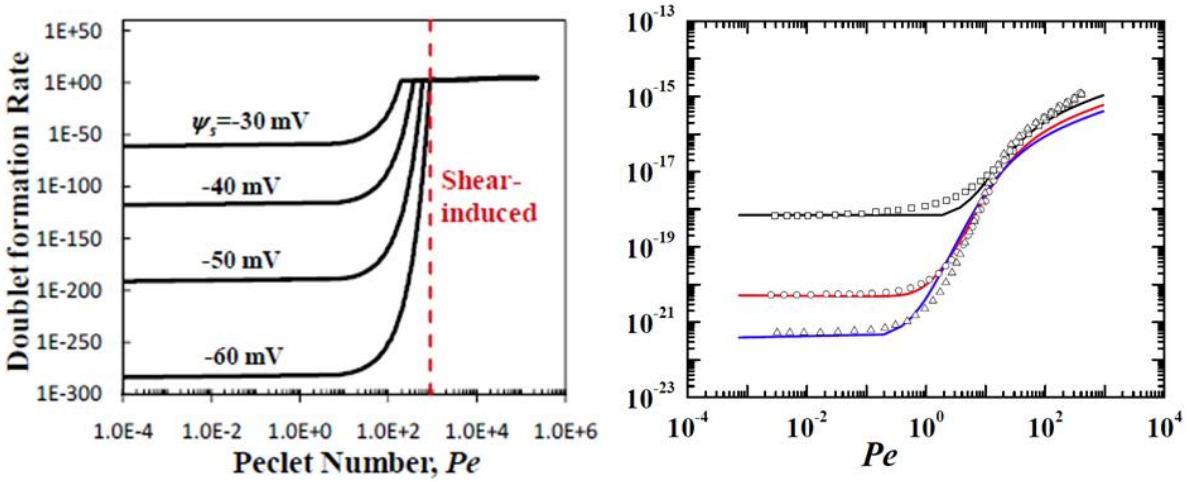

Figure 4-15 Normalized aggregation rate constants between two particles as a function of Peclet number. In the left frame the rate of doublet formation is reported at four levels of particles surface potential. In the right frame the rate of doublet formation is reported at a fixed surface potential but at different ionic strength (increasing toward bottom). Left and right pictures taken respectively from [27] and [6].

the system is in purely Brownian-like conditions and the aggregation rate is dominated by the value of the repulsive energy barrier V_m (RLCA); in these situations the exponential term of equation (4.8) is positive and large characteristic aggregation times result; at high Peclet numbers Pe>>1 the system is in purely shear induced regime and the aggregation rate results practically independent from the value of the repulsive energy barrier V_m (RLCA); in these conditions the exponential term of equation (4.8) is negative and small characteristic aggregation times result.

Furthermore, if the system starts at low *Pe*, as soon as aggregation takes place the Peclet number increases rapidly with the cluster sizes $Pe \propto a^3$ and the pure shear induced region is entered. The exponential term of equation (4.8) becomes in fact negative and the characteristic times of aggregation drop abruptly.

The theory forecasts therefore an initial induction time followed by an explosive rise of viscosity typically observed in colloidal system under shear (i.e. gelation).

This system behavior can be better appreciated looking at the relation between the volume fraction φ and the medium viscosity, which can be expressed for non-diluted solutions by the Krieger-Dougherty equation [28]:

$$\frac{\eta}{\eta_0} = \left(1 - \frac{\varphi}{\varphi_{max}}\right)^{-[\eta]\varphi_{max}} \tag{4.9}$$

Where η_0 is the viscosity at $\varphi = 0$, $[\eta]$ is the intrinsic viscosity and φ_{max} is the packing fraction, its upper limit is approximately 0.64 for random close packaging and roughly 0.71 for the closest possible arrangements of spheres. Using the geometric series and expanding the right member of equation (4.9) leads to a power dependence of the medium viscosity. If the system is aggregating at low *Pe*, since the aggregates volume is increasing slowly, φ remains almost constant (cf. equation (1.35)) and a flat medium viscosity profile results (initial induction time). As soon as larger aggregates are formed, the aggregates volume and φ rapidly grow in time due to the exponential increase of *Pe*, the medium viscosity therefore according with equation (4.9) explodes until at last the limit where a gel is formed is reached.

On the other hand if the aggregating particles undergo coalescence the characteristic time of aggregation will be affected as the cluster size will be shrinked by the on-going coalescence, therefore reducing the increase in terms of *Pe* number, slowing

down the aggregation process. If full coalescence is possible($\tau_{coal} \ll \tau_{agg}$) no occupied volume growth would be allowed, the volume fraction and the viscosity would remain constant and so no gel could be formed; if coalescence occurs partially, gel could be formed but longer initial induction times and as consequence delayed gelation times would be observed.

Several shear-induced aggregations were carried out in the rheometer for the samples 30%MMA, 50%MMA and 60%MMA (cf. Figure 4-16 - Figure 4-24).

Only these samples were sheared because it was impossible to raise the rheometer temperature over 55 [ºC], due to problems related with the evaporation of the latexes, and as previously discussed the 70%MMA sample showed to be very sensitive to breakage already in stagnant condition when the experimental temperature was below its T_g. The analysis were performed at a fixed shear rate $\dot{\gamma} = 4900$ [Hz] and final DC=5%. In order to enhance samples coalescence, according to the samples T_g values listed in Table 2-5, three different temperatures (25 [ºC], 35 [ºC], 45 [ºC]) were analyzed. Furthermore in order to observe shear induced aggregations in reasonable experimental times but still remaining in RLCA regime it was necessary to reduce the repulsive effect of the energy barrier maximum V_m by adding small quantities of salt. In particular, three different NaCl concentrations 120 [mM], 130 [mM] and 140 [mM] were identified as the proper ones. The results are reported in Figure 4-16 - Figure 4-24. In these graphs is shown the time evolution of the samples viscosity at the different temperatures and salt concentrations tested; it can be seen that gelation occurs for the majority of the samples (the viscosity abruptly increases after a given lag time).

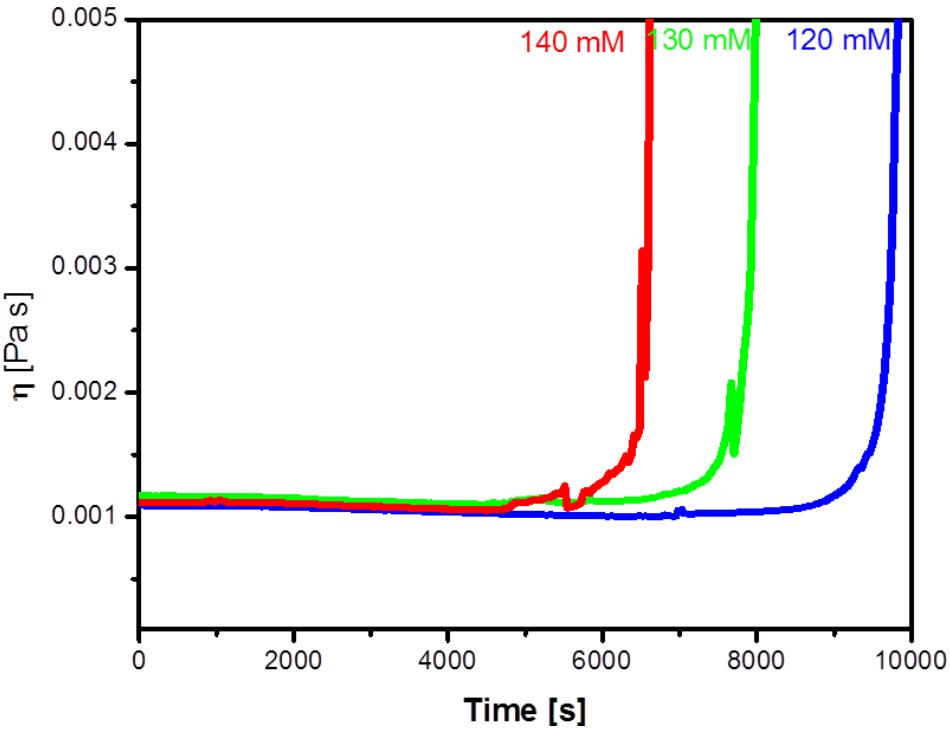

Figure 4-16 Evolution of viscosity as function of time in the rheometer for 30%MMA; Different salt concentrations (140 [mM], 130 [mM] and 120 [mM])of NaCl are reported at 25 º[C].

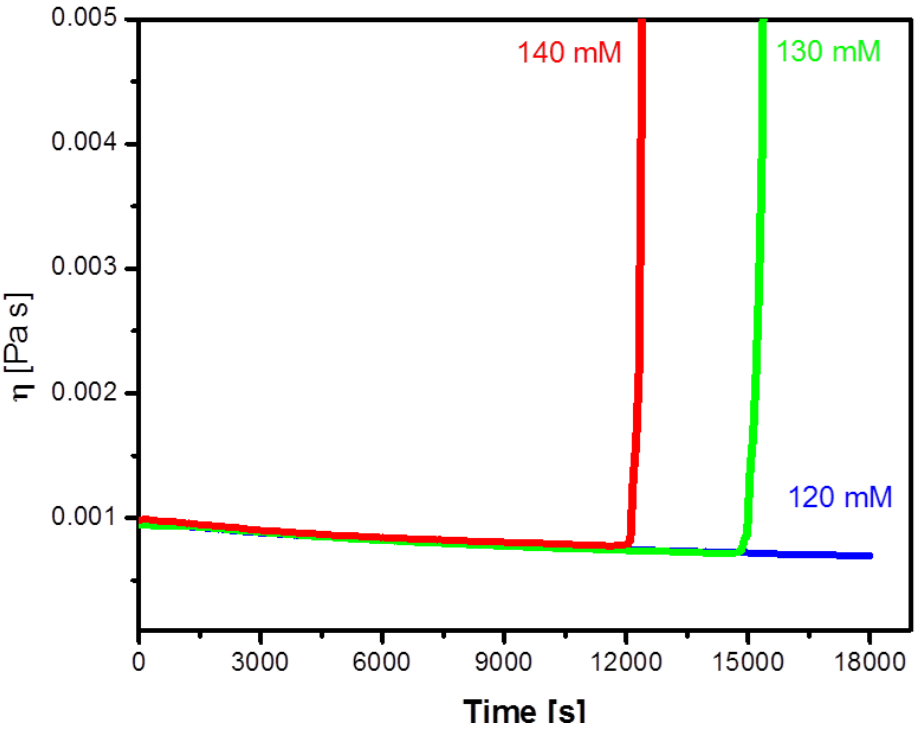

Figure 4-17 Evolution of viscosity as function of time in the rheometer for 30%MMA; Different salt concentrations (140 [mM], 130 [mM] and 120 [mM])of NaCl are reported at 35 º[C].

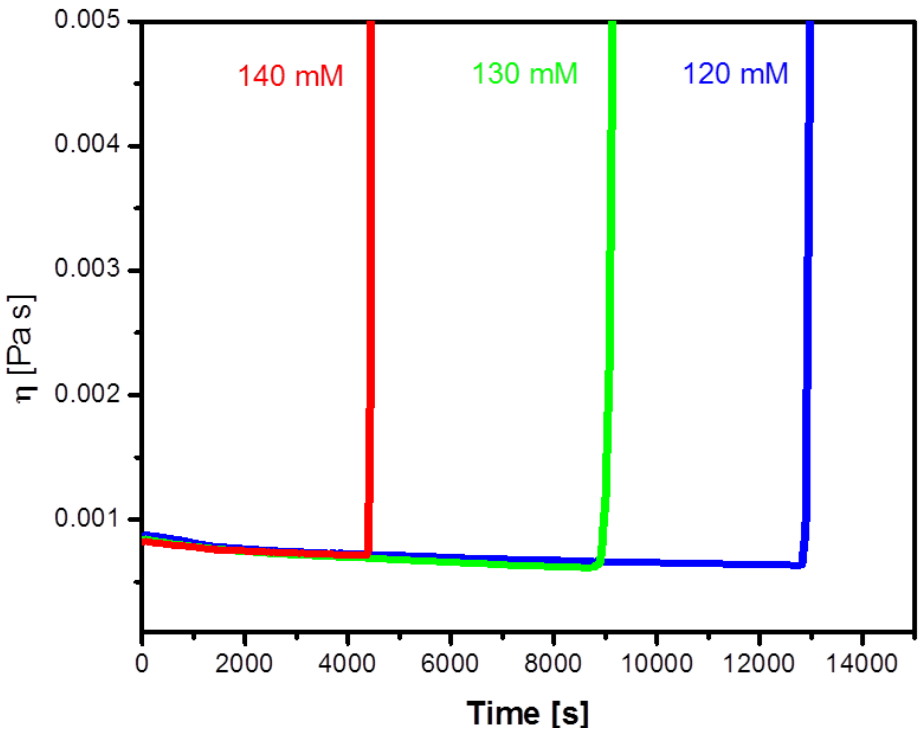

Figure 4-18 Evolution of viscosity as function of time in the rheometer for 30%MMA; Different salt concentrations (140 [mM], 130 [mM] and 120 [mM])of NaCl are reported at 45 º[C].

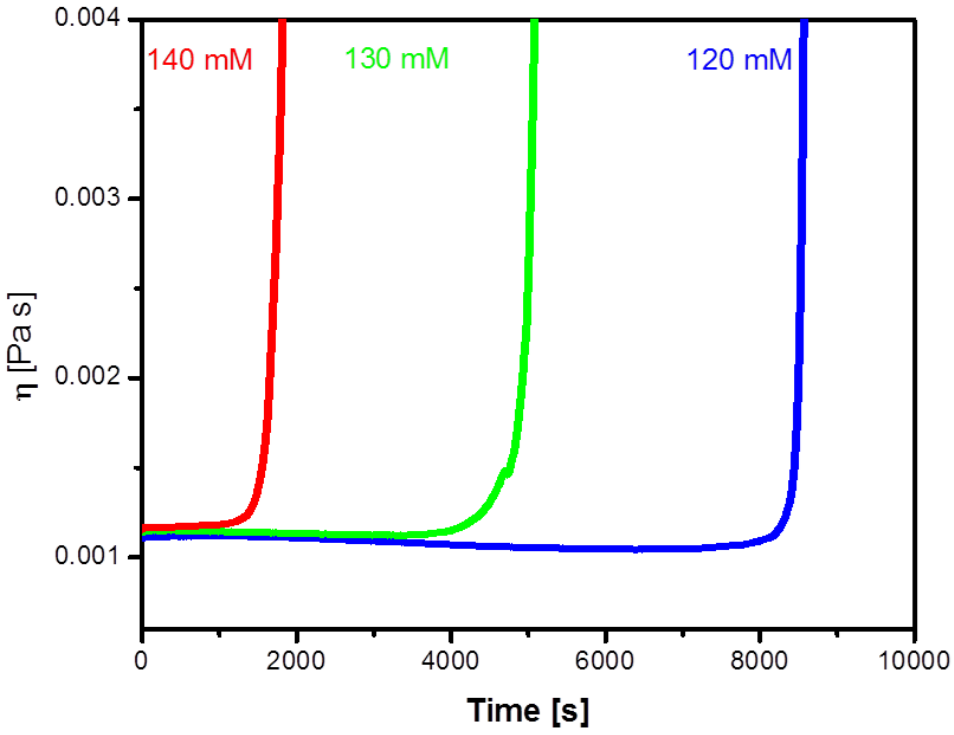

Figure 4-19 Evolution of viscosity as function of time in the rheometer for 50%MMA; Different salt concentrations (140 [mM], 130 [mM] and 120 [mM])of NaCl are reported at 25 º[C].

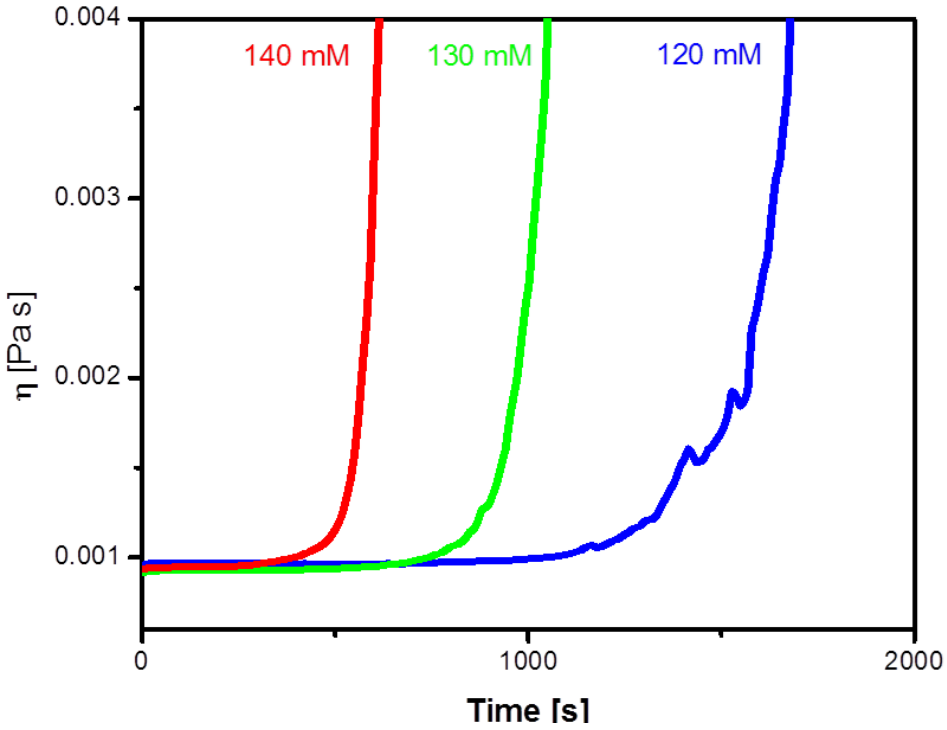

Figure 4-20 Evolution of viscosity as function of time in the rheometer for 50%MMA; Different salt concentrations (140 [mM], 130 [mM] and 120 [mM])of NaCl are reported at 35 º[C].

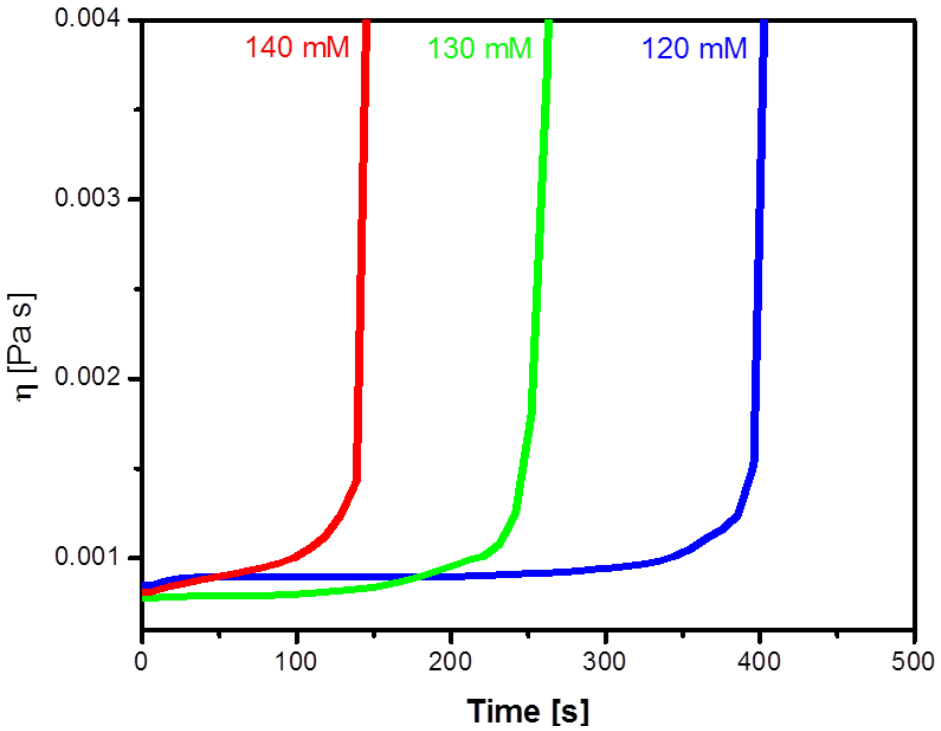

Figure 4-21 Evolution of viscosity as function of time in the rheometer for 50%MMA; Different salt concentrations (140 [mM], 130 [mM] and 120 [mM])of NaCl are reported at 45 º[C].

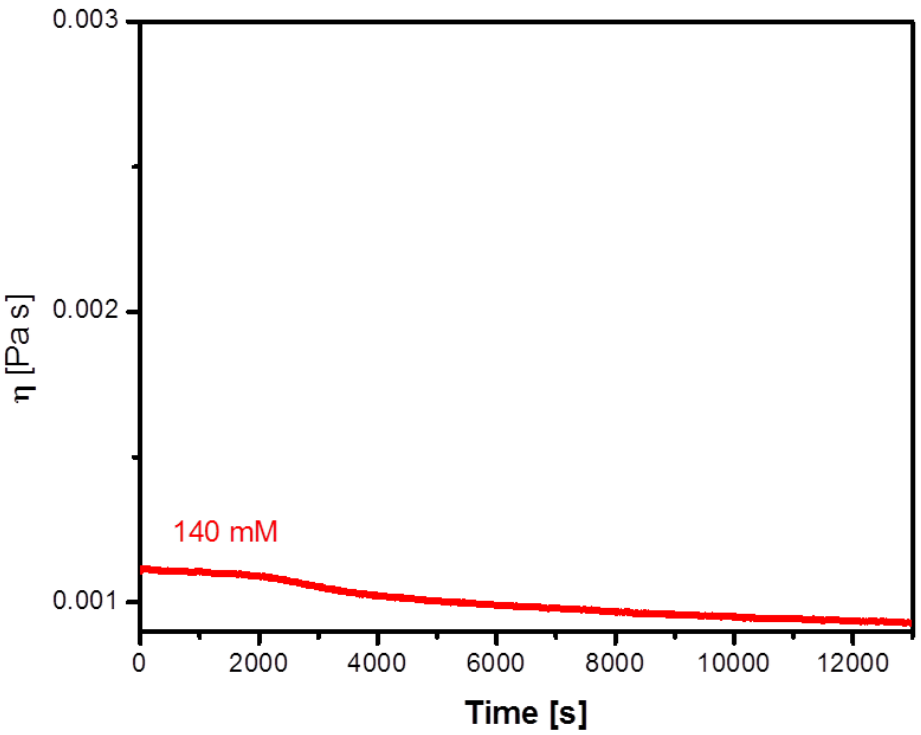

Figure 4-22 Evolution of viscosity as function of time in the rheometer for 60%MMA; 140 [mM]NaCl at 25 º[C].

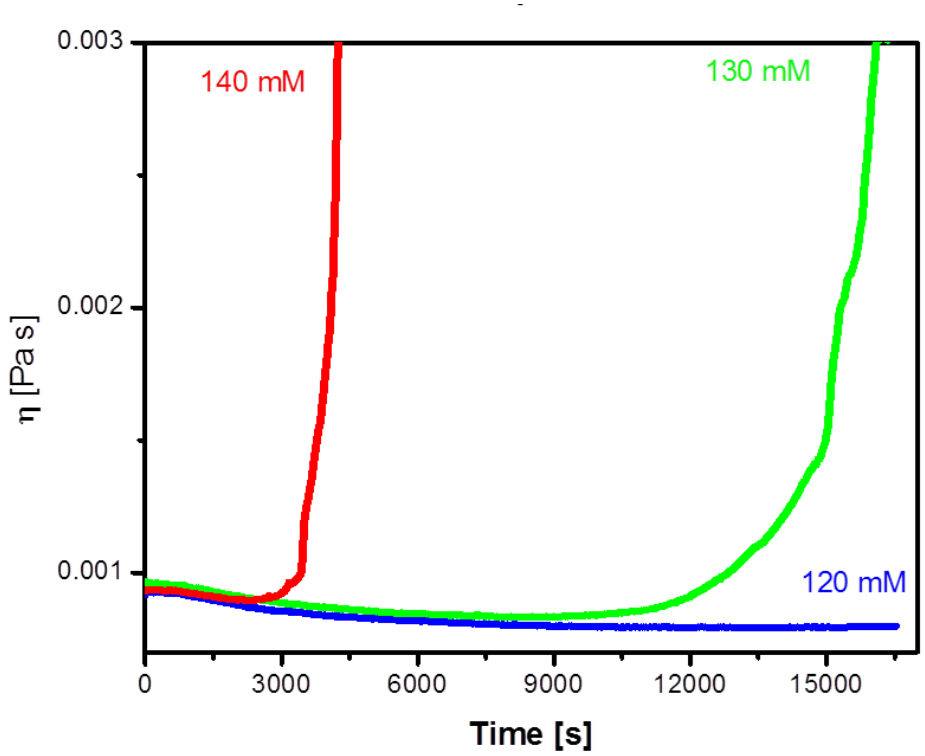

Figure 4-23 Evolution of viscosity as function of time in the rheometer for 60%MMA; Different salt concentrations (140 [mM], 130 [mM] and 120 [mM])of NaCl are reported at 35 º[C].

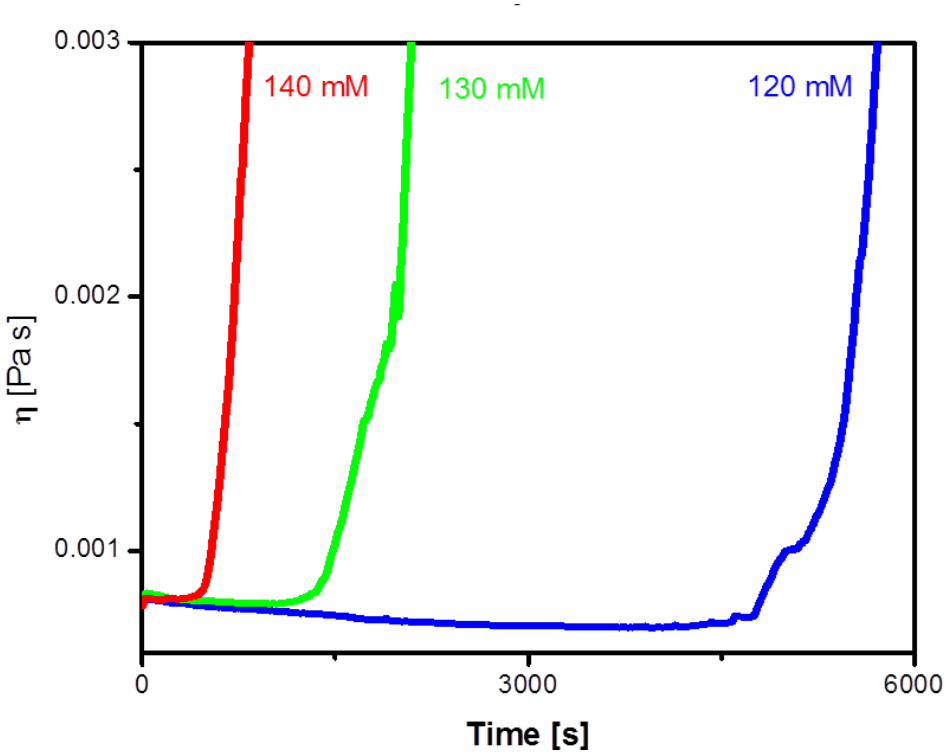

Figure 4-24 Evolution of viscosity as function of time in the rheometer for 60%MMA; Different salt concentrations (140 [mM], 130 [mM] and 120 [mM])of NaCl are reported at 45 º[C].

At these experimental conditions the initial Peclet number values are in the range 10-11. As previously discussed if the initial Peclet values exceed a certain threshold, the doublet formation rate becomes interaction potential independent and only dominated by the shear induced aggregation. As a main consequence, if our samples would be located in that region, each of them would gel at the same time regardless of the salt amount present. As shown in Figure 4-16 - Figure 4-24, this does not happen in our cases, indicating that our samples are not in pure shear-conditions and their aggregation rate is indeed affected by their potential. In this frame, the aggregation and coalescence characteristic times depend on the samples salt concentrations, temperatures and compositions. Each of these contributions will be individually discussed in the following sections.

4.2.1 Salt effect

From Figure 4-16 - Figure 4-24 the effect of the salt on the characteristic time of aggregation can be clearly appreciated: the higher is the salt concentration the

sooner the gelation occurs. This trend is explainable in terms of double layer compression as can be seen looking at the form of the total interaction potential energy which in the simplest but sufficient case of two slabs at distance r with small overlapping is given by [1]:

$$V_{tot} = -\frac{A}{12\pi r^2} + 64\xi N_0 k_B T Z^2 \exp\left(-\frac{r}{\xi}\right) \qquad \text{`(4.10)}$$

Where $Z = \tanh\left(\frac{ze\psi_0}{4k_B T}\right)$ and ψ_0 is the surface potential. The first and second terms on the right hand side of equation (4.10) describe respectively Van der Waals and electrostatics interactions. If the salt concentration increases, the Van der Waals contribute (salt independent) remains unchanged where as the Debye length ξ decreases according to equation (1.9); if ξ decreases results from equation (4.10) a lower electrostatic repulsive contribute to V_{tot}, in particular to the maximum value. From equation (4.8) if the repulsive term of V_m is progressively reduced, smaller characteristic aggregation times are obtained.

This situation is depicted in the right frame of Figure 4-15 where the rates of doublet formation, reported at a fixed surface potential and at different ionic strength, exhibit a step shape in the RLCA region, in detail the higher is the ionic strength, the higher is the aggregation rate and the lower is the gel time once the shear induced region is entered.

4.2.2 Temperature effect

In Figure 4-25 - Figure 4-27 the temperature impact for each sample composition is reported. As values of t_{gel} were taken the intersections between two linear regression, one made with the last medium viscosity measures and the other with the starting ones of Figure 4-16 - Figure 4-24.

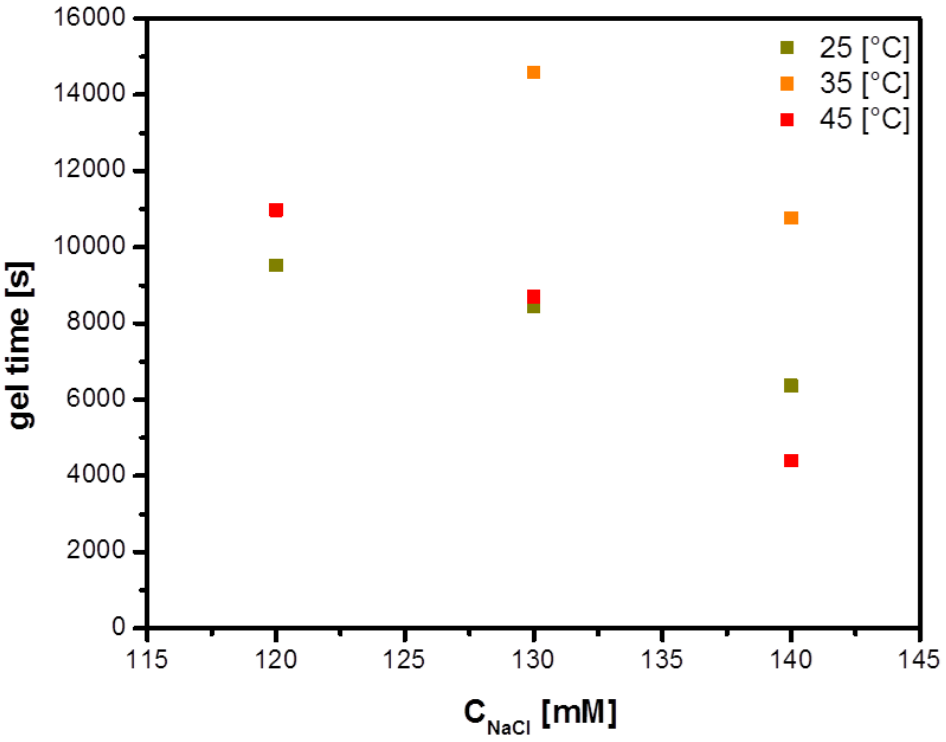

Figure 4-25 Gel times for 30% MMA as function of temperature and salt concentration

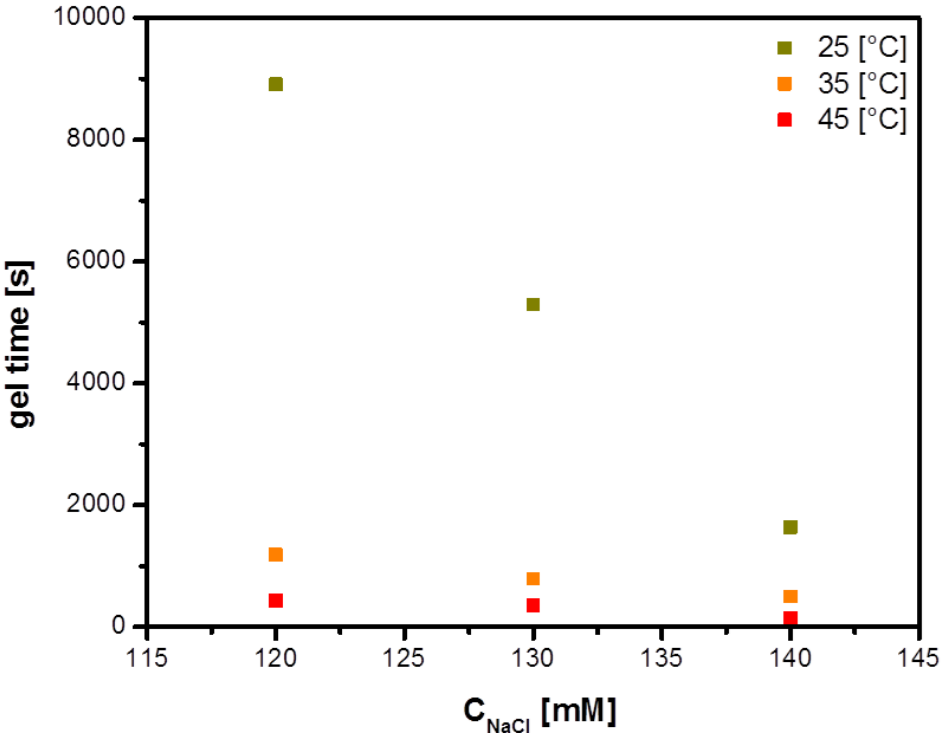

Figure 4-26 Gel times for 50% MMA as function of temperature and salt concentration

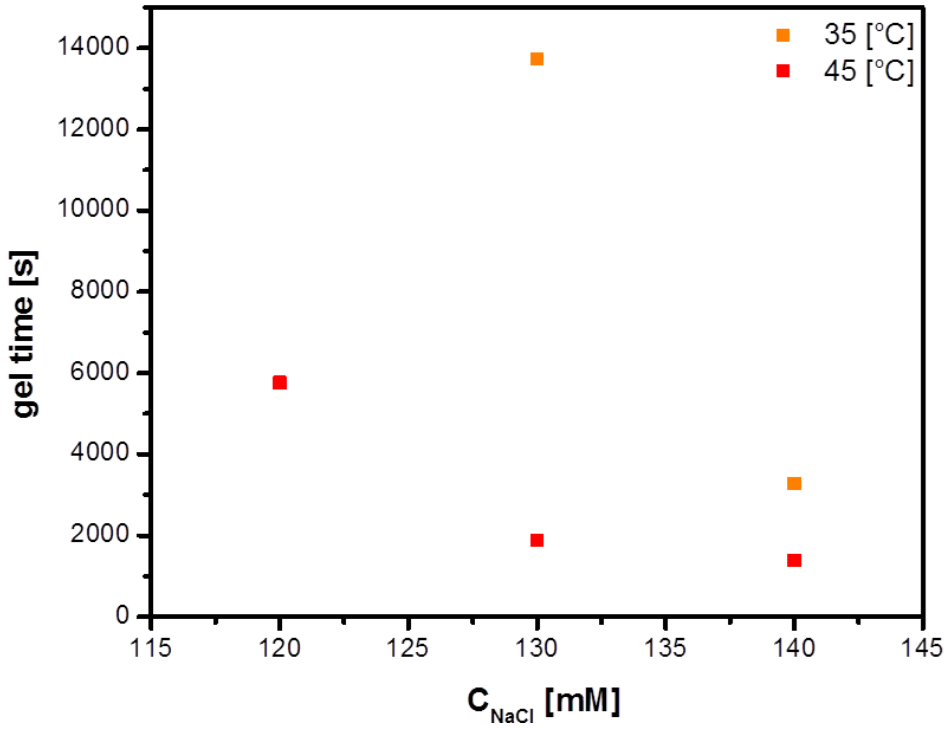

Figure 4-27 Gel times for 60% MMA as function of temperature and salt concentration

Figure 4-26 and Figure 4-27 show that increasing the temperature leads to progressively lower gelation times for the 50%MMA and 60%MMA samples. On the other hand the 30% MMA sample (Figure 4-25) shows a peculiar trend: upon temperature increase, the gel times initially increase (compare 25 [^{o}C] and 35 [^{o}C]) while a further increase (from 35 [^{o}C] to 45 [^{o}C]) leads to a further reduction of the gel times.

The expected effect of a temperature increase on the gel time is a delay in the gelation due to an enhancement of coalescence as more compact clusters with a smaller occupied volume fraction are formed. The results reported show that this occurs only in case of the 30%MMA sample at 35 [ºC] while in all the other experiments the gelation occurs sooner the higher the temperature. This trend can be explained in terms of effects competition between aggregation and coalescence times. In fact if the temperature increases the medium and particles viscosities decrease and, according to equations (1.36) and (4.8), the coalescence and aggregation characteristic times are respectively shorter and longer. On the other hand as the temperature increases a destabilizing effect takes place (the presence and nature of this destabilizing effect and its temperature dependence will be further unveiled) and affects the characteristic times of aggregation which result

progressively shorter. In the explored temperature range the destabilizing effect increases significantly with the temperature and always overcomes the coalescence ones. There is an exception for the points at 35 [ºC] of the 30%MMA: since for this sample coalescence occurs the most, its contributions at 35 [ºC] dominate the destabilizing ones leading therefore to a delay in the gel time; at 45 [ºC] nevertheless destabilization, which increases in temperature, dominates again and the delay effect of coalescence disappears.

The presence of a destabilizing effect that takes places as the temperature increases was proven by CCC measurements. (cf. Figure 4-28). The 30%MMA, 50%MMA and 60%MMA samples CCC were in fact measured again at 45 [ºC] in the same conditions as they were measured at 25 [ºC];as shown, increasing the temperature leads to a decrease in the CCC.

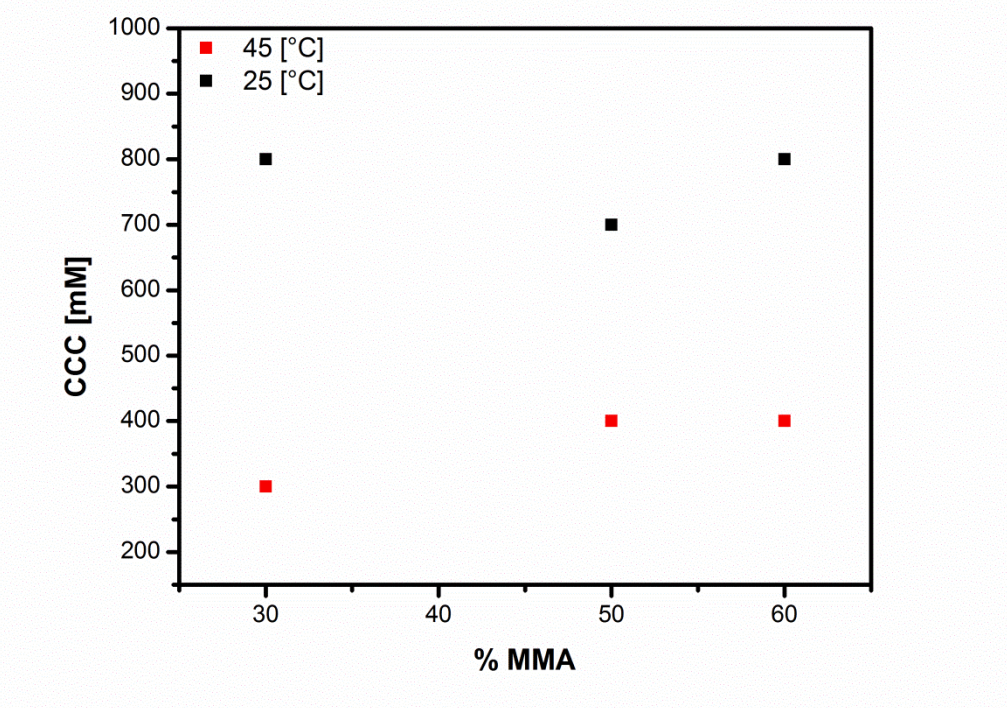

Figure 4-28 Comparison of the critical coagulation concentration values as function of the MMA% measured at $\varphi = 1x10^{-5}$ and $T = 25, 45$ [ºC]

Since the samples stabilities, as previously discussed, are related to the absolute values of the potential energy barriers, the nature of this temperature behavior can be extrapolated by looking at the relative dependence of the DLVO interaction potential (equation (4.10)). In detail the impact of the temperature on the DLVO

potential attractive term can be appreciated by substituting equation (4.7) in equations (4.10) and (4.8); as can be seen only the second member of the Hamaker constant slightly decreases if the temperature increases. Weaker Van der Waals contributes would result in higher repulsive contributes in the DLVO potential and in particular for the energetic barrier maximum. As a consequence a longer aggregation characteristic time should be expected. Thus this effect is insignificant since it would lead to the opposite trend compared with the one observed. The impact of the temperature on the DLVO potential repulsive term can be appreciated by substituting equation (4.10) in equation (4.8); as can be seen the factor $k_B T$ in the electrostatic term cancels out and only a square root temperature dependence results in the Debye length. This dependence in the range of temperatures investigated is negligible (3%) and therefore the electrostatic contributes to the DLVO potential can be practically considered temperature independent. Furthermore as additional evidence for the electrostatics temperature independence the ζ-potential values were measured at 45 [ºC] (cf. Figure 4-29).

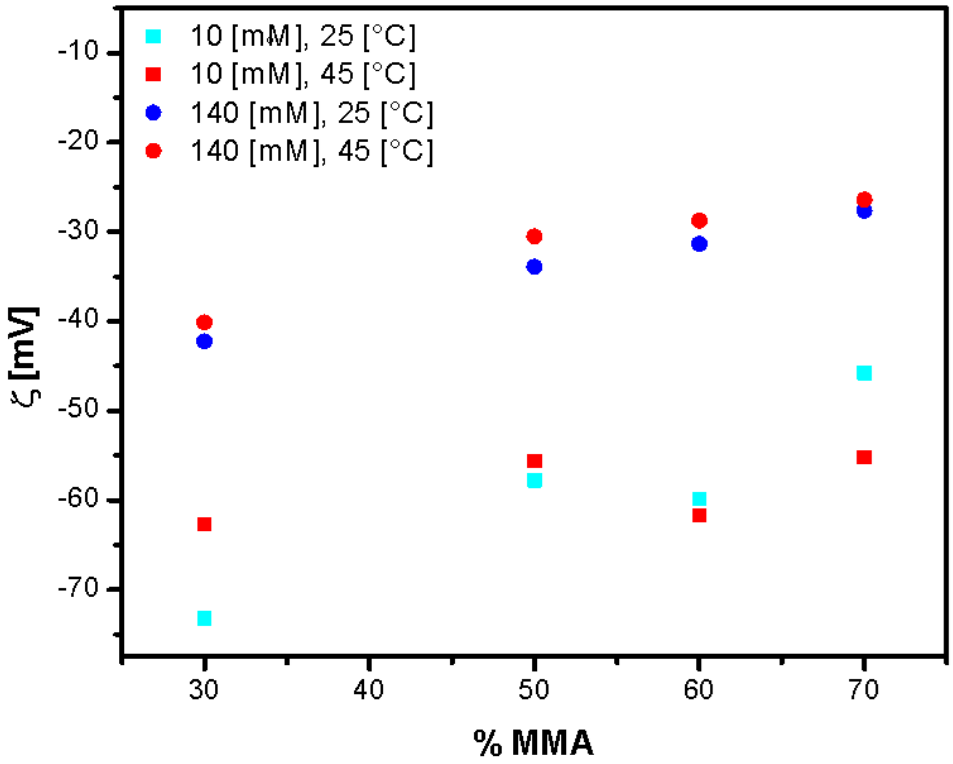

Figure 4-29 Comparison between ζ-potential values measured at 10 and 140 [mM] with $\varphi = 1\text{x}10^{-5}$ and $T = 25, 45$ [ºC]

As can be seen from they do not differ much from the ones at 25 [ºC].
Since the stability decrease upon temperature increase cannot be explained in terms of DLVO potential which has been substantially proven as temperature independent, the nature of this destabilizing effect must be ascribed to non DLVO contributions. These contributions can be condensed in a term which, if introduced into the expression of the DLVO potential (equation (4.10)), decreases the overall maximum value of the energetic barrier. From equation (4.8) as the values of the overall energetic barrier are reduced, smaller characteristic times of aggregation result

4.2.3 Composition effect

In order to elucidate the impact of the sample composition on the characteristic times of coalescence are reported in Figure 4-30 - Figure 4-32 the gelation times of all the samples as function of the salt concentrations at each specific temperature tested.

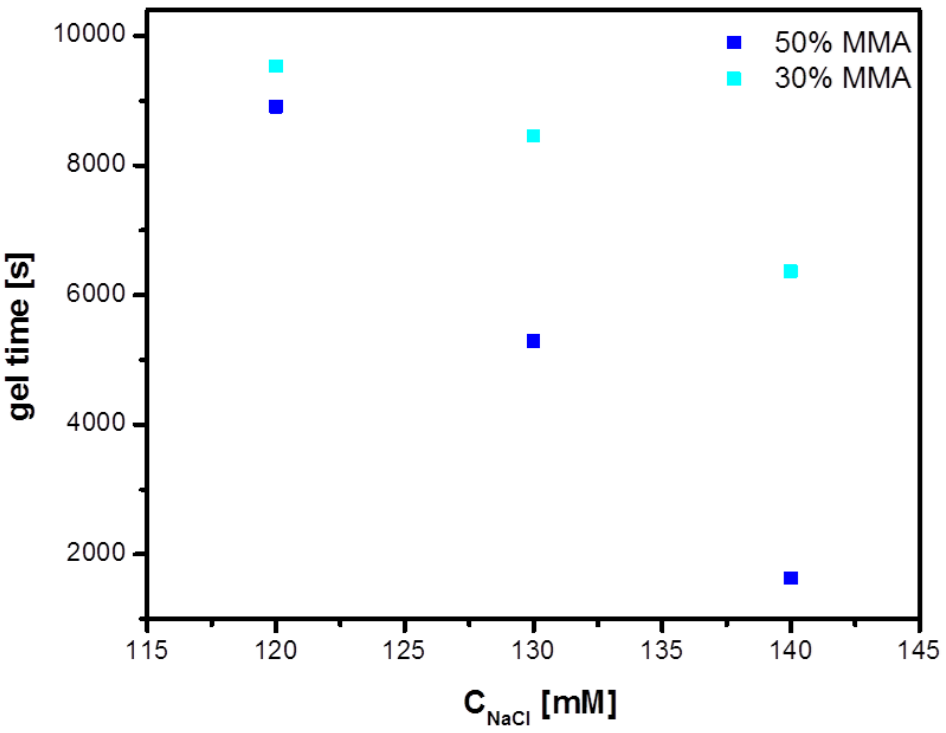

Figure 4-30 Gel times for 30%MMA, 50%MMA, 60% MMA as function of composition and salt concentration at 25 [ºC]

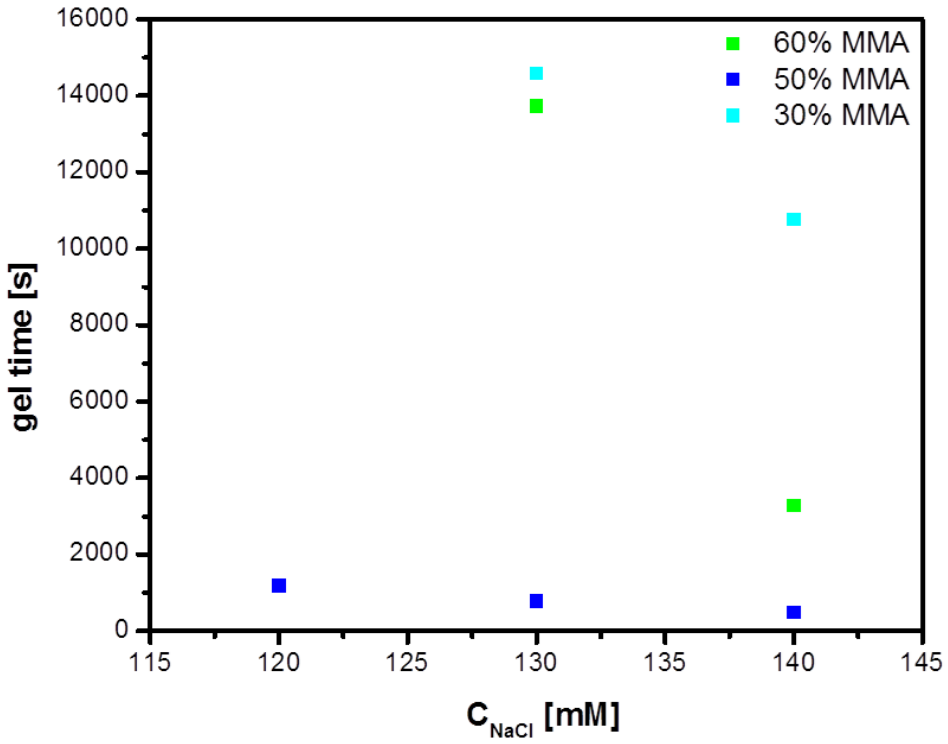

Figure 4-31 Gel times for 30%MMA, 50%MMA, 60% MMA as function of composition and salt concentration at 35 [ºC]

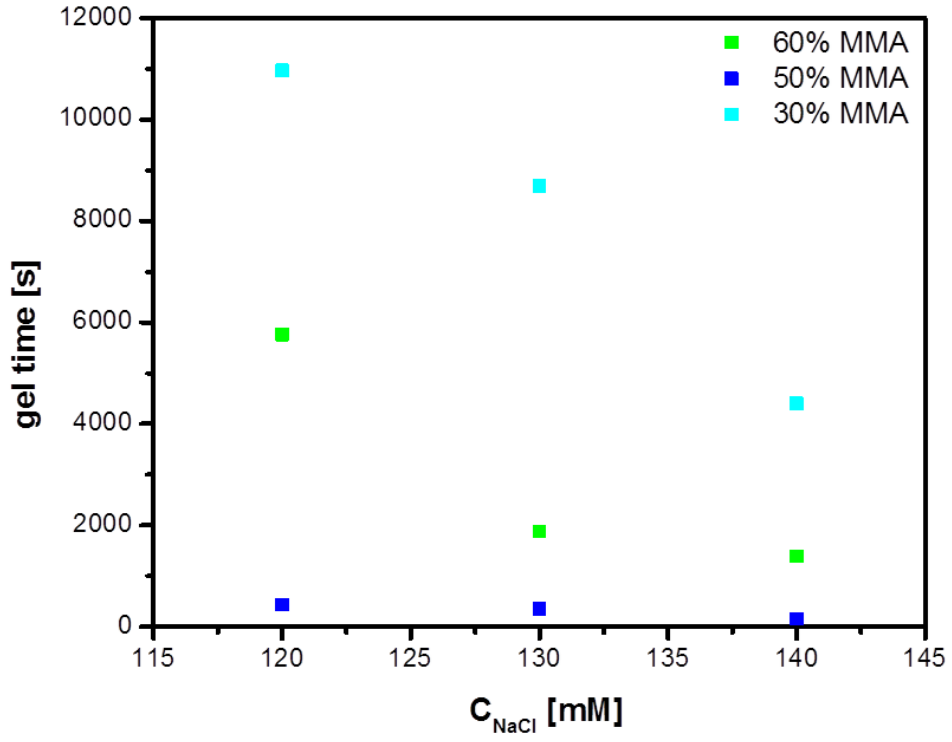

Figure 4-32 Gel times for 30%MMA, 50%MMA, 60% MMA as function of composition and salt concentration at 45 [ºC]

These graphs show that the 30%MMA and 50%MMA samples exhibit progressively shorter gelation times at all the temperatures experimented. On the other side the 60%MMA sample t_{gel} values are always placed in the middle of the previous two. Furthermore it is worth to point out that at 25°[C] for this sample no gelation was reported in the experimental time.

The expected effect of increasing the BA content is to observe longer gelations as the resulting polymers have smaller T_g and hence an increased coalescence. This trend is observed only for the 30%MMA and the 50%MMA samples.

In order to explain the results of the 60%MMA sample it is worth to remark that if the sample is tested below its T_g, it is strongly subjected to breakage; furthermore breakage is strongly reduced as coalescence takes place. As consequence around the T_g the competition between these two phenomena have to be considered in order to figure out our sample behavior. At 25 [°C] the 60%MMA sample is below its T_g (35°[C]) and coalescence cannot occur. Breakage is the dominating phenomenon and therefore no gel can be formed. At 35 [°C] despite the 60%MMA sample it is starting to coalesce, the particles are not interpenetrating enough in order to avoid breakage and longer gelation times than the 50%MMA sample result. At 45°[C] coalescence occurs more than at 35 [°C] (compare 60%MMA sample t_{gel} in Figure 4-31 and Figure 4-32) but still the particles bond are weak and again as consequence of breakage longer gelation times than the 50%MMA sample result.

As shown in Figure 4-30 - Figure 4-32 for the 30%MMA and 50%MMA samples the effect of breakage results completely negligible and increasing the BA content reduces progressively the characteristic times of coalescence.

The reason for which only for the 60%MMA breakage is observable is due to the different coalescence between the samples. As previously discussed, the material glass transition does not occur at a specific temperature but in region centered around it. As can be seen from the plot listed in APPENDIX I at 25 [°C] the 30%MMA and 50%MMA samples are already above their respective glass transition. This is not the case for the 60%MMA sample where at 35 [°C] and 45 [°C] it is still in progress. As consequence for this sample at the temperatures tested coalescence occurs less compared with the 30%MMA and 50%MMA samples and therefore the competition aggregation – breakage is observable.

5 CONCLUSION:

The scope of the present work was to study the interplay between coalescence and aggregation under shear for polymeric colloidal dispersions.

Four latexes of poly(methylmethacrylate-co-butylacrylate) (PMMA-co-BA) have been synthesized by starved emulsion polymerization in a semi-batch reactor. The different ratios of methyl methacrylate and butyl acrylate employed allowed preparing particles exhibiting a glass transition temperature gradient which allowed studying the behavior of coalescence in the system.

Initially the interplay aggregation-coalescence in stagnant conditions (DLCA) was explored. Since coalescence can occur only above the glass transition temperature, aggregations induced by salt (NaCl) were performed at different temperatures. Furthermore in order to clearly unveil the effects of coalescence these salt induced aggregations were carried out at low and high latexes volume fractions. At low volume fraction, since the characteristic time of coalescence is smaller than the aggregation one, it is found that coalescence affects aggregation resulting in lower aggregates gyration radii compared with the non coalescing ones and in high fractal dimension. Faster coalescence in general occurs the higher is the value of the sample temperature over its T_g until eventually a maximum coalescence rate is reached. The reason is due to the particles viscosity which plays a crucial role in the characteristic time of coalescence: as the temperature rises, viscosity decreases increasing the rate of coalescence. As consequence it resulted that the rich BA samples were progressively coalescing more the higher was the BA content. At high volume fractions, since the characteristic time of coalescence is larger than the aggregation one, all the samples destabilized with salt ended up in gels; in these conditions it is found that coalescence affects aggregation through the gels strength: the samples, if their experimental temperature was below their corresponding T_g, formed weak gels (gels that, if mildly agitated, showed to break rearranging in more compact structures); on the other side if their experimental temperature was above their corresponding T_g ,strong gels were formed (gels that, if shaken, did not show

any sign of breakage). The gel strength is explainable in terms of coalescence that allows the particles to partially interpenetrate one with another, sticking and forming resistant aggregates.

Successively the particles aggregation in RLCA was investigated. In these conditions it was found that the Van der Waals contributes to the samples V_m values are composition independent. The electrostatic impact on V_m values was evaluated for each sample by surface charges and ζ-potential measurements. It results in general that increasing the BA content slightly increases the surface charges, the ζ-potential and as consequence the V_m values. Higher absolute values of potential energy barriers lead to higher stability. The samples stability was determined by measuring their critical coagulation concentrations and is found to follow the same trend of the V_m values. In spite of that increasing the MMA content over a certain threshold reduces dramatically the rich MMA samples stability. Since the surface charges and ζ-potential values are comparable for all the samples, this behavior is ascribed to a material effect or a non-DLVO contribution.
Furthermore as the samples stability was measured at higher temperature it resulted to drop abruptly. This remarkable destabilizing effect due to the temperature cannot be explained in terms of DLVO potential which is substantially temperature independent and is due to non DLVO contributions.

Finally the interplay between aggregation and coalescence was investigated in shear conditions. Shear induced aggregation were performed at different salt concentrations and temperatures at a fixed dry content and shear rate.
In these conditions where the initial samples aggregation rate is dominated by the value of the repulsive energy barrier, it is found that the competition between aggregation and coalescence depends on the samples salt concentrations, temperatures and compositions.
Increasing the salt concentration reduces only the characteristic times of aggregation (double layer compression).
If the temperature increases two competitive effects take place: on one hand the coalescence and aggregation characteristic times result respectively shorter and longer as the medium and particles viscosities decrease. On the other hand the

thermal non-DLVO destabilizing effect decreases the characteristic times of aggregation. In the explored temperature range these destabilization contributions increase significantly with the temperature and in the majority of the cases overcome the coalescence effects. As consequence the impact of the temperature is relevant only for the characteristic time of aggregation.

As exception, the reduction of the characteristic time of coalescence due to effect of the temperature was appreciated for the most coalescing sample where coalescence becomes comparable with aggregation; in this case in fact upon temperature increase, the gel times initially increase while a further increase leads to a further reduction of them.

Increasing the BA content reduces progressively the characteristic times of coalescence. This tendency is confirmed only if the sample is above its glass transition. If the sample is tested below its glass transition it results strongly subjected to breakage which prevents gel formations. During the glass transition it is possible to observe the interplay between coalescence and breakage. As coalescence takes place, breakage is considerably reduced until over a certain point it becomes negligible and longer gelation times are found as the resulting polymers have an increased coalescence.

References

1. Morbidelli, *Polymer Reaction & Colloid Engineering LECTURE NOTES*, 2013.
2. Nomura, M., H. Tobita, and K. Suzuki, *Emulsion polymerization: Kinetic and mechanistic aspects.* Polymer Particles, 2005. **175**: p. 1-128.
3. Jose´ C. de la Cal, J.R.L., Jose M. Asua, Alessandro Butte`, Giuseppe Storti, and Massimo Morbidelli, *Handbook of Polymer Reaction Engineering*. p. Chapter 6, Emulsion Polymerization.
4. Waychunas, G.A., *Structure, aggregation and characterization of nanoparticles.* Nanoparticles and the Environment, 2001. **44**: p. 105-166.
5. M. Elimelech, J.G., X. Jia, R.A. Williams, John Gregory, Xiaodong Jia and Richard A Williams, *Particle Deposition & Aggregation*.
6. Zaccone, A., et al., *Theory of activated-rate processes under shear with application to shear-induced aggregation of colloids.* Physical Review E, 2009. **80**(5).
7. Frenkel, J., *Viscous flow of crystalline bodies under the action of surface tension.* Journal of Physics, 1945. **IX**.
8. R. M. Wheaton, L.J.L., *DOWEX Ion Exchange Resins Fundamentals of Ion Exchange*, 2000, Dow Liquid Separations Office.
9. Dietrich Braun , H.C., Matthias Rehahn, Helmut Ritter, Brigitte Voit, *Polymer Synthesis: Theory and Practice Fundamentals, Methods, Experiments*. 2012: Springer.
10. Berg, J.C., *An introduction to Interfaces & Colloids, The Bridge to Nanoscience*. 2010: World Scientific Publishing Co. Pte. Ltd.
11. Sorensen, C.M., *Light scattering by fractal aggregates: A review.* Aerosol Science and Technology, 2001. **35**(2): p. 648-687.
12. Macosko, C.W., *Rheology: Principles, Measurements, and Applications*. 1994: WILEY-VCH.
13. Sandkühler, P., *Kinetics of Aggregation and Gel Formation in Colloidal Dispersions*, 2004.
14. Lattuada, M., et al., *Aggregation kinetics of polymer colloids in reaction limited regime: experiments and simulations.* Advances in Colloid and Interface Science, 2003. **103**(1): p. 33-56.
15. Wu, H., M. Lattuada, and M. Morbidelli, *Dependence of fractal dimension of DLCA clusters on size of primary particles.* Advances in Colloid and Interface Science, 2013. **195**: p. 41-49.
16. Xie, D.L., et al., *Criticality for shear-induced gelation of charge-stabilized colloids.* Soft Matter, 2010. **6**(12): p. 2692-2698.
17. Ehrl, L., M. Soos, and M. Morbidelli, *Dependence of aggregate strength, structure, and light scattering properties on primary particle size under turbulent conditions in stirred tank.* Langmuir, 2008. **24**(7): p. 3070-3081.
18. Eggersdorfer, M.L., et al., *Multiparticle Sintering Dynamics: From Fractal-Like Aggregates to Compact Structures.* Langmuir, 2011. **27**(10): p. 6358-6367.
19. Wypych, G., *Handbook of Polymer*. 2013.
20. Nijenhuis, D.W.V.K.a.K.T., *Properties of Polymers*. Fourth Edition ed.
21. Israelachvili, J.N., *Intermolecular and Surface Forces, Third edition*. 2011.
22. *METHYL METHACRYLATE CAS N°: 80-62-5*, U. Chemicals, Editor.
23. *N-BUTYL ACRYLATE CAS N°: 141-32-2*, U. Chemicals, Editor.

24. Lattuada, M., et al., *Modelling of aggregation kinetics of colloidal systems and its validation by light scattering measurements.* Chemical Engineering Science, 2004. **59**(8-9): p. 1783-1798.
25. Kumar, S. and D. Ramkrishna, *On the solution of population balance equations by discretization .1. A fixed pivot technique.* Chemical Engineering Science, 1996. **51**(8): p. 1311-1332.
26. Kumar, S. and D. Ramkrishna, *On the solution of population balance equations by discretization .2. A moving pivot technique.* Chemical Engineering Science, 1996. **51**(8): p. 1333-1342.
27. Wu, H., et al., *Effect of Temperature on High Shear-Induced Gelation of Charge-Stabilized Colloids without Adding Electrolytes.* Langmuir, 2010. **26**(4): p. 2761-2768.
28. *Principles of Colloid and Surface Chemistry, Third Edition, Revised and Expanded*. 1997.

APPENDIX I

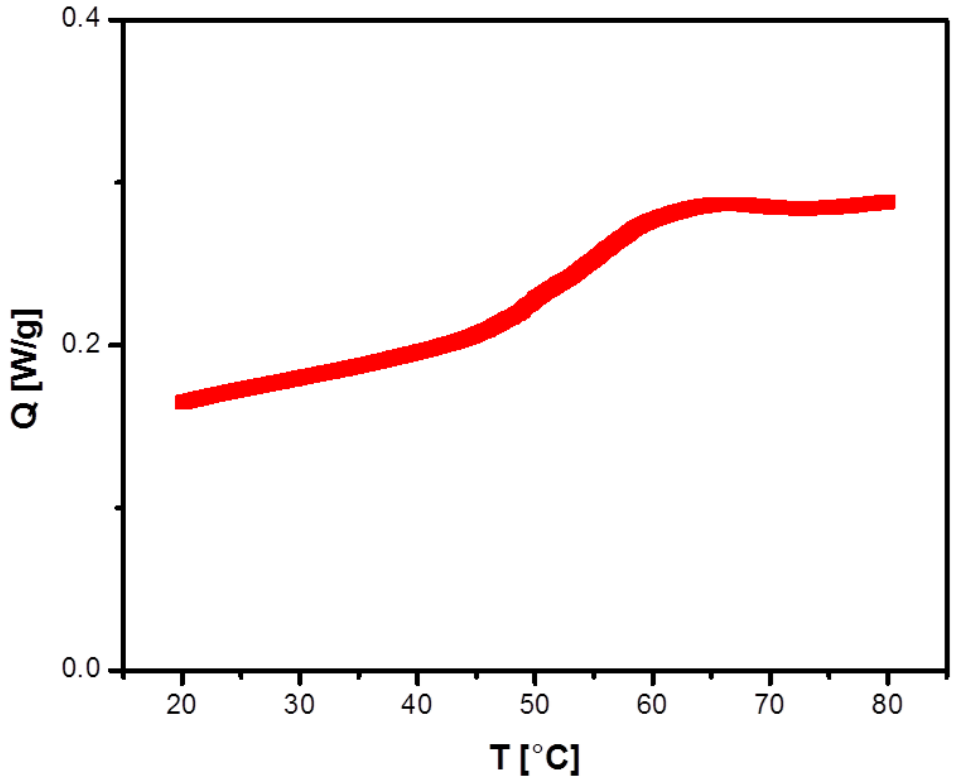

Figure 1 Heat flux as function of temperature for 70%MMA

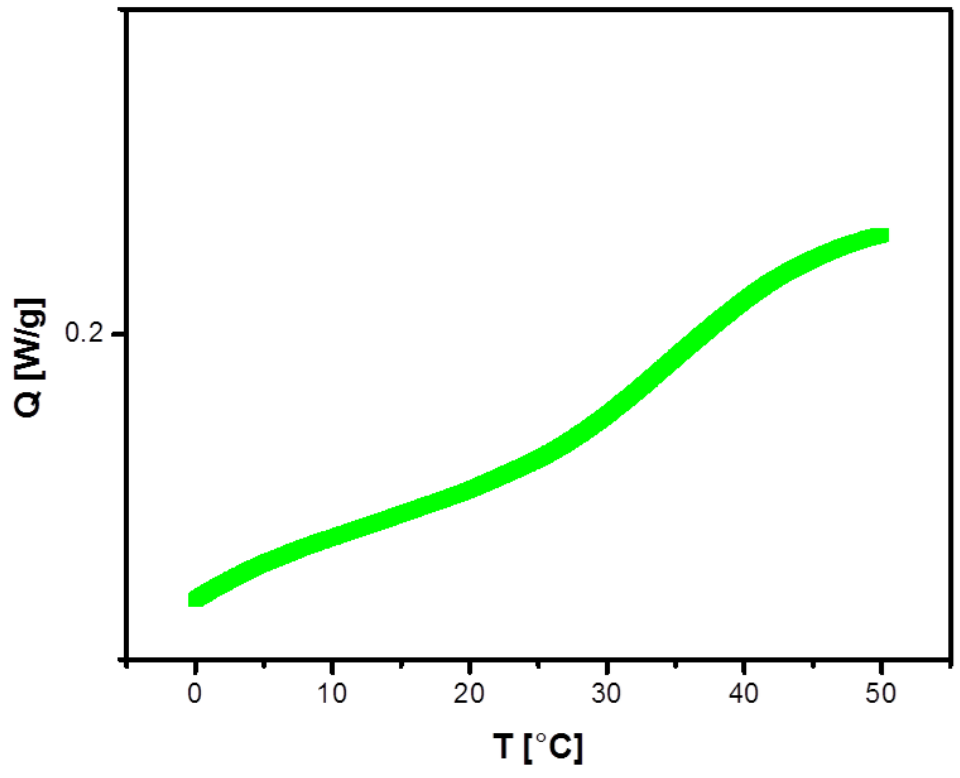

Figure 2 Heat flux as function of temperature for 60%MMA

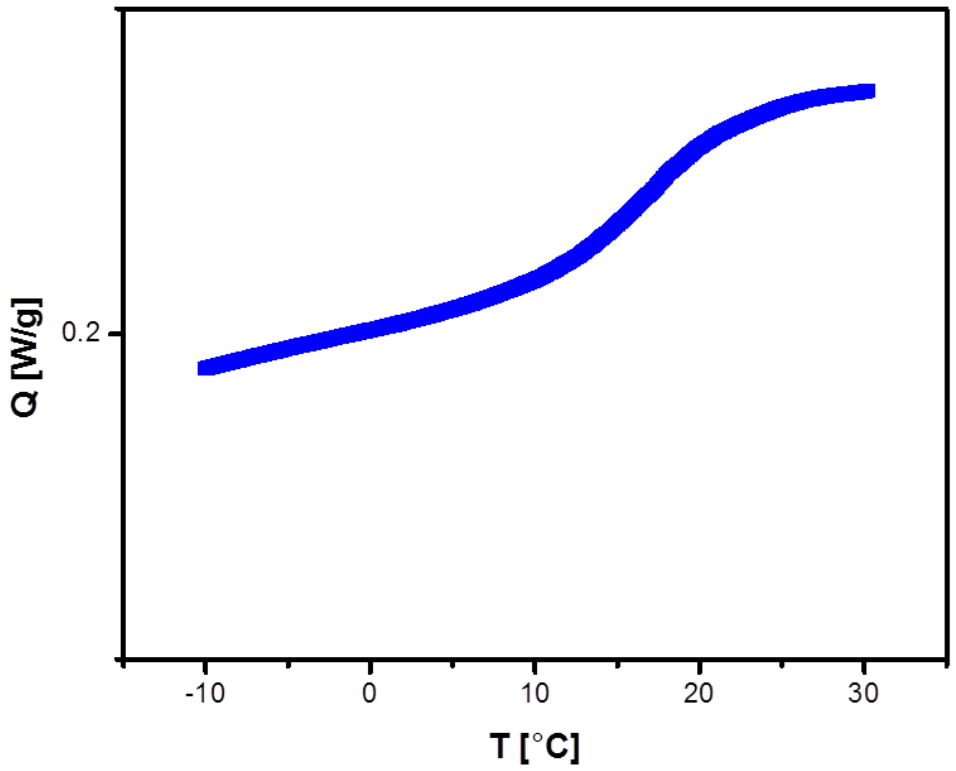

Figure 3 Heat flux as function of temperature for 50%MMA

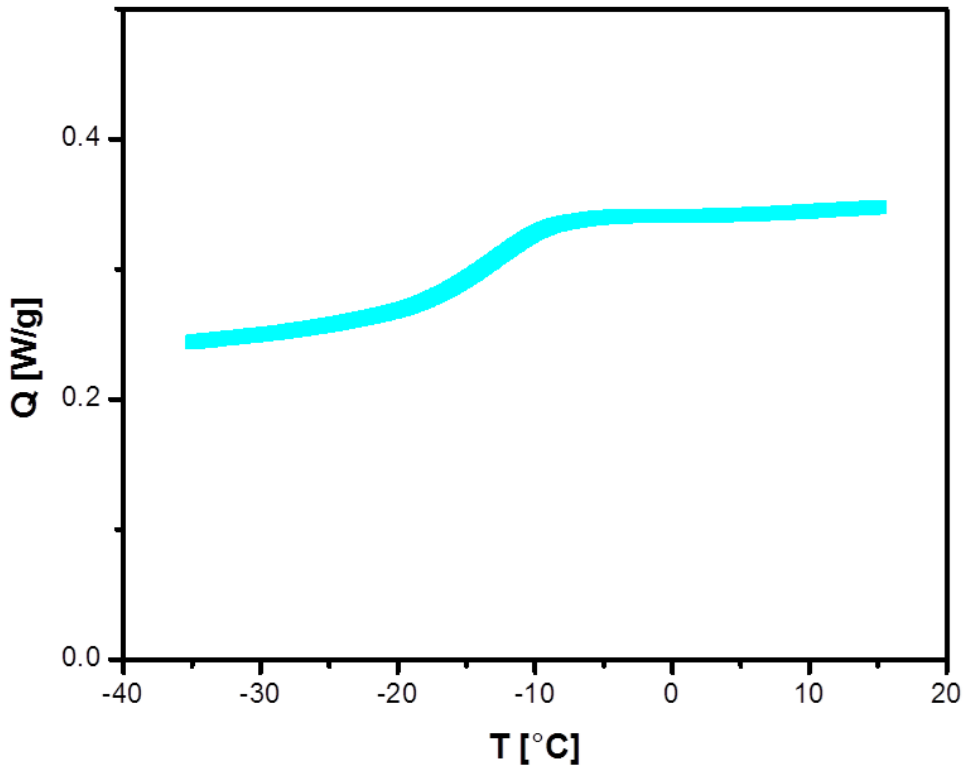

Figure 4 Heat flux as function of temperature for 30%MMA

APPENDIX II

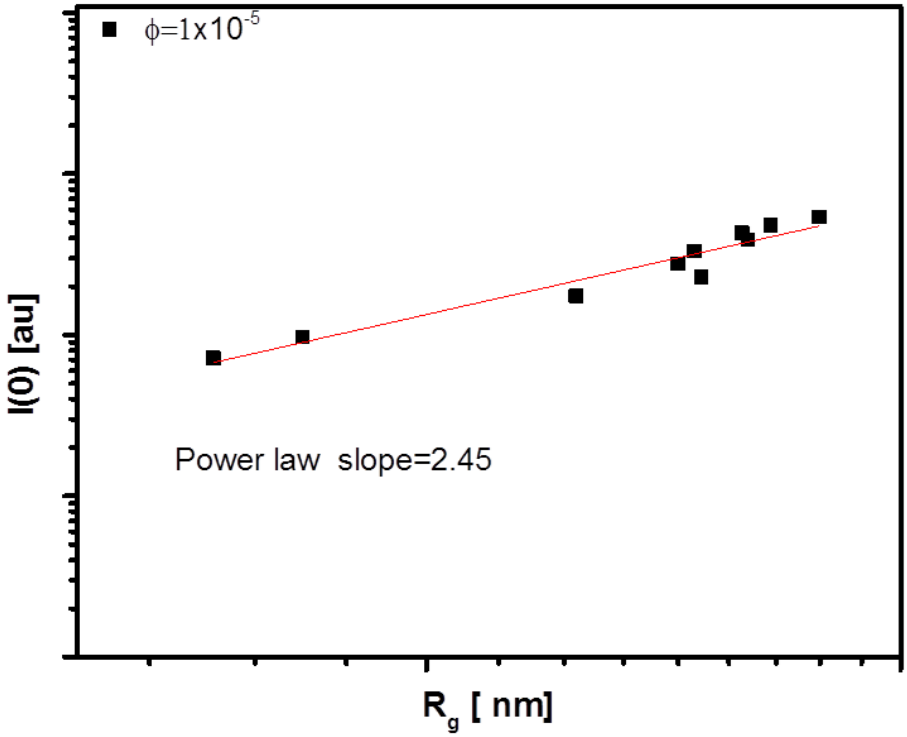

Figure 1 $I(0)$ vs. R_g plot for30%MMA in the small angle static light scattering at $\varphi =$ 1x10^{-5}

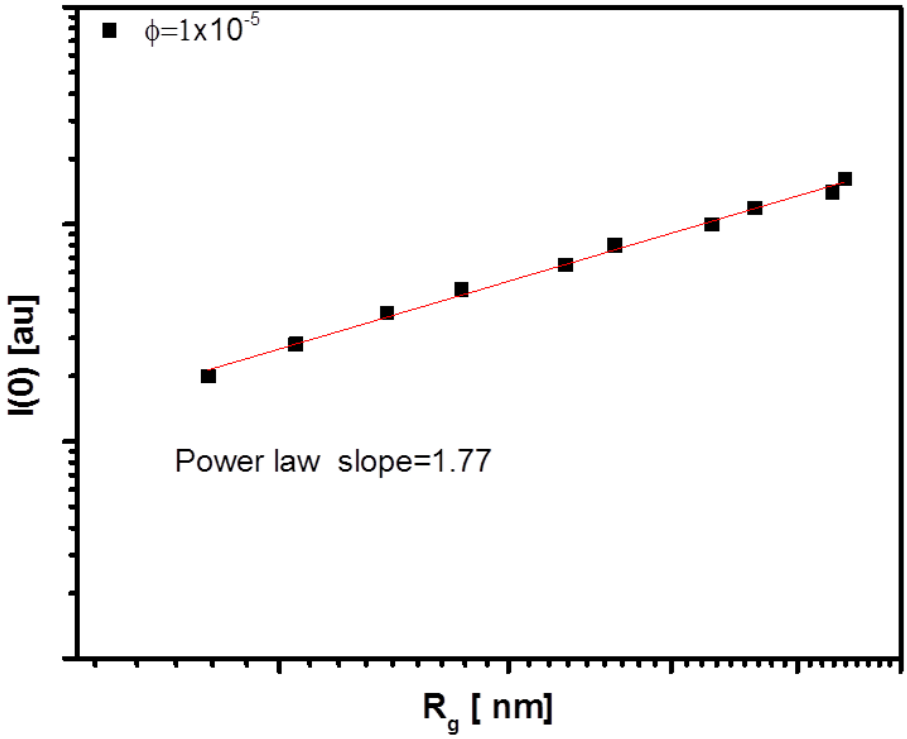

Figure 2 $I(0)$ vs. R_g plot for50%MMA in the small angle static light scattering at $\varphi =$ 1x10^{-5}

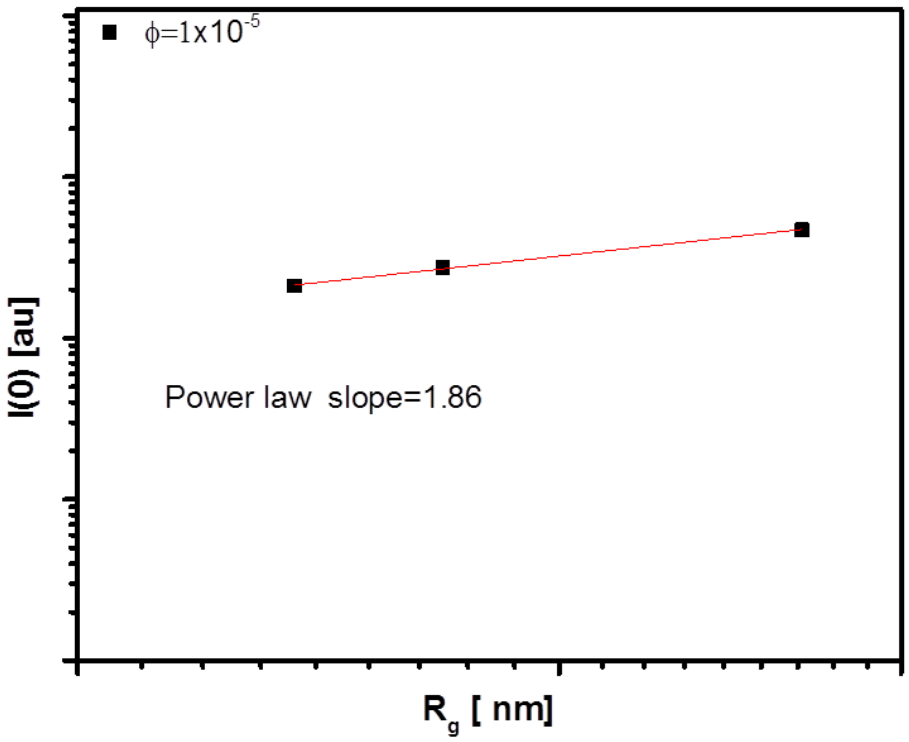

Figure 3 $I(0)$ vs. R_g plot for60%MMA in the small angle static light scattering at $\varphi =$ $1x10^{-5}$

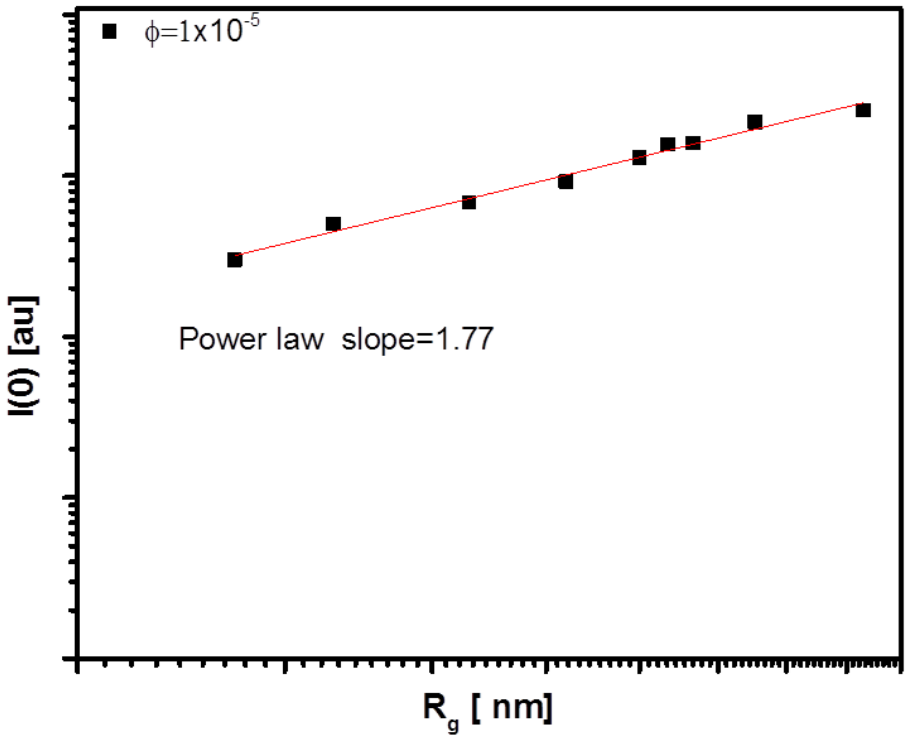

Figure 4 $I(0)$ vs. R_g plot for70%MMA in the small angle static light scattering at $\varphi =$ $1x10^{-5}$

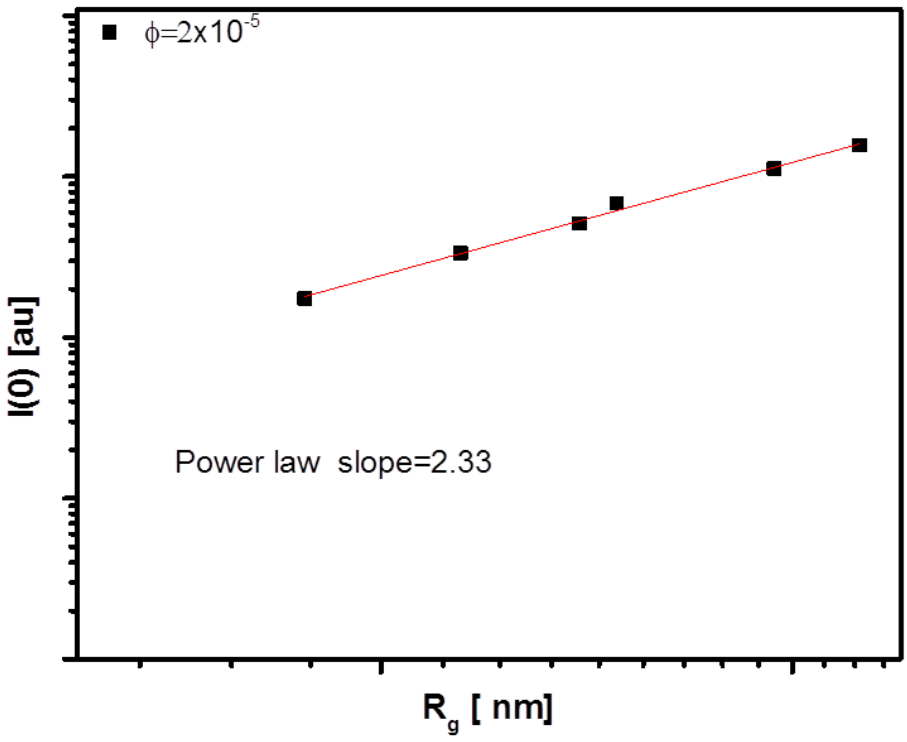

Figure 5 $I(0)$ vs. R_g plot for30%MMA in the small angle static light scattering at $\varphi =$ $2x10^{-5}$

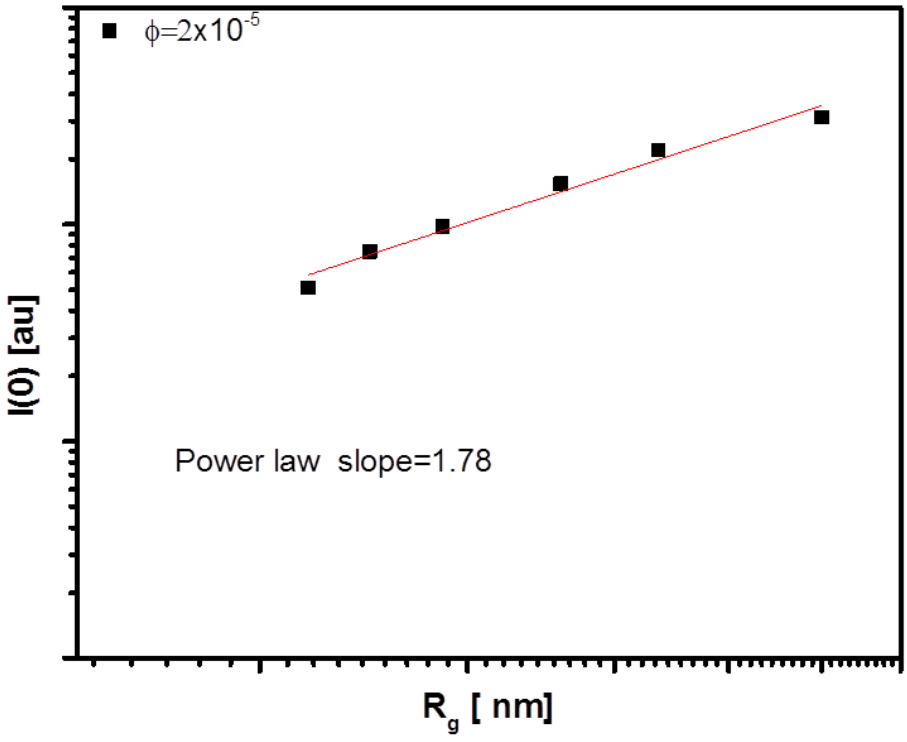

Figure 6 $I(0)$ vs. R_g plot for50%MMA in the small angle static light scattering at $\varphi =$ $2x10^{-5}$

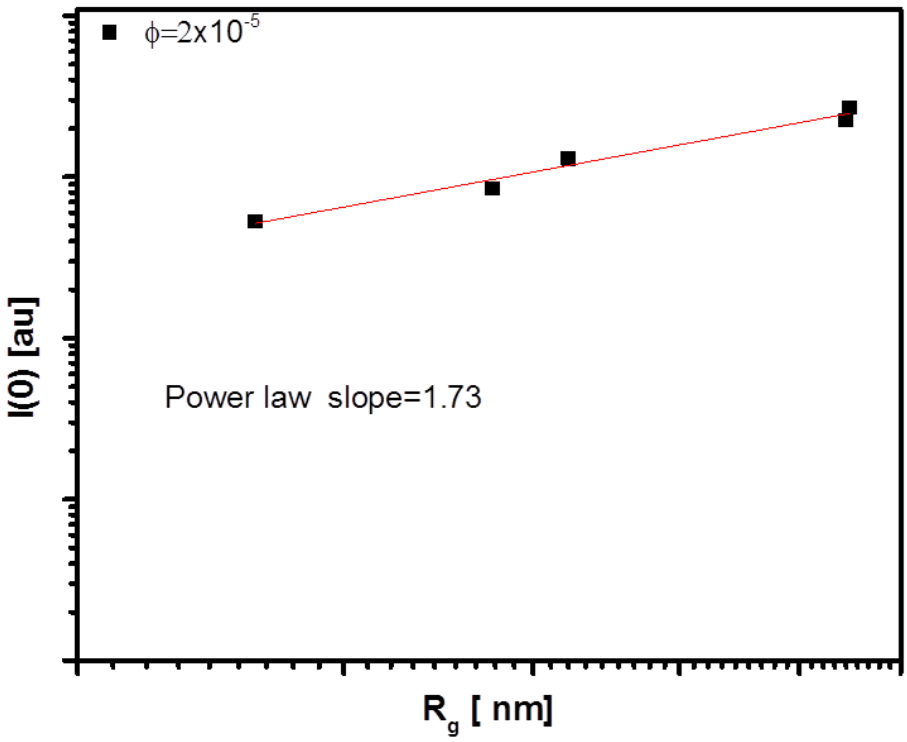

Figure 7 $I(0)$ vs. R_g plot for60%MMA in the small angle static light scattering at $\varphi =$ $2x10^{-5}$

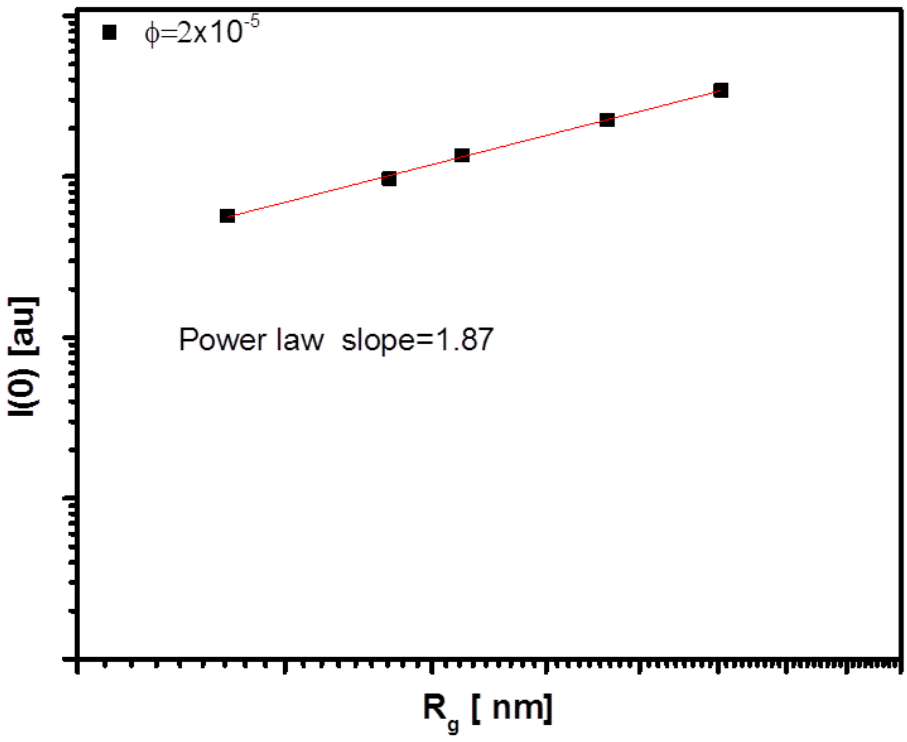

Figure 8 $I(0)$ vs. R_g plot for 70%MMA in the small angle static light scattering at $\varphi =$ $2x10^{-5}$

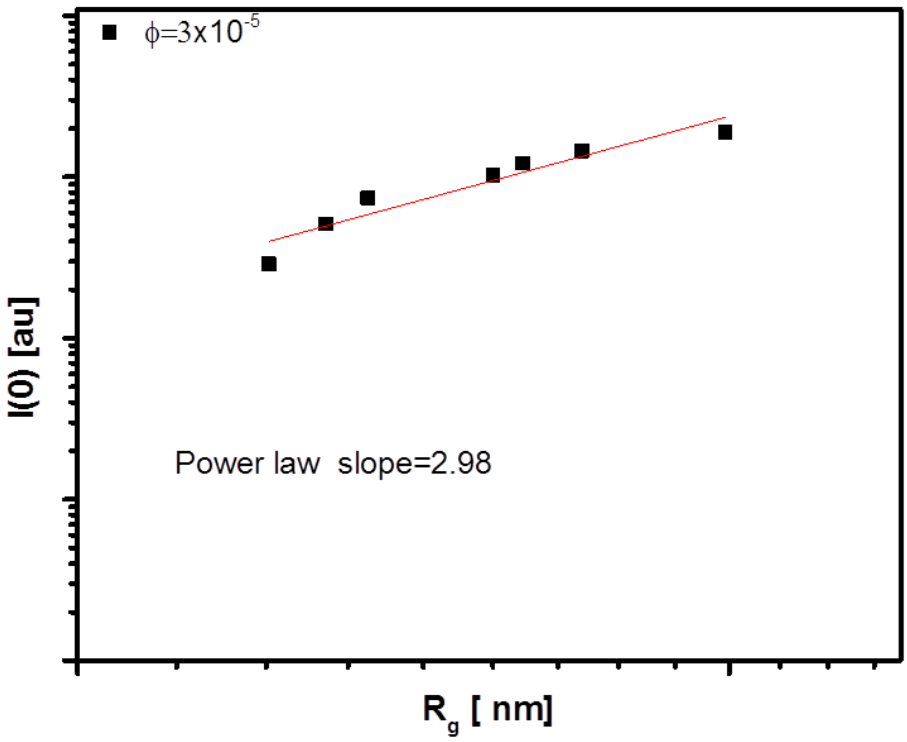

Figure 9 $I(0)$ vs. R_g plot for 30%MMA in the small angle static light scattering at $\varphi =$ $3x10^{-5}$

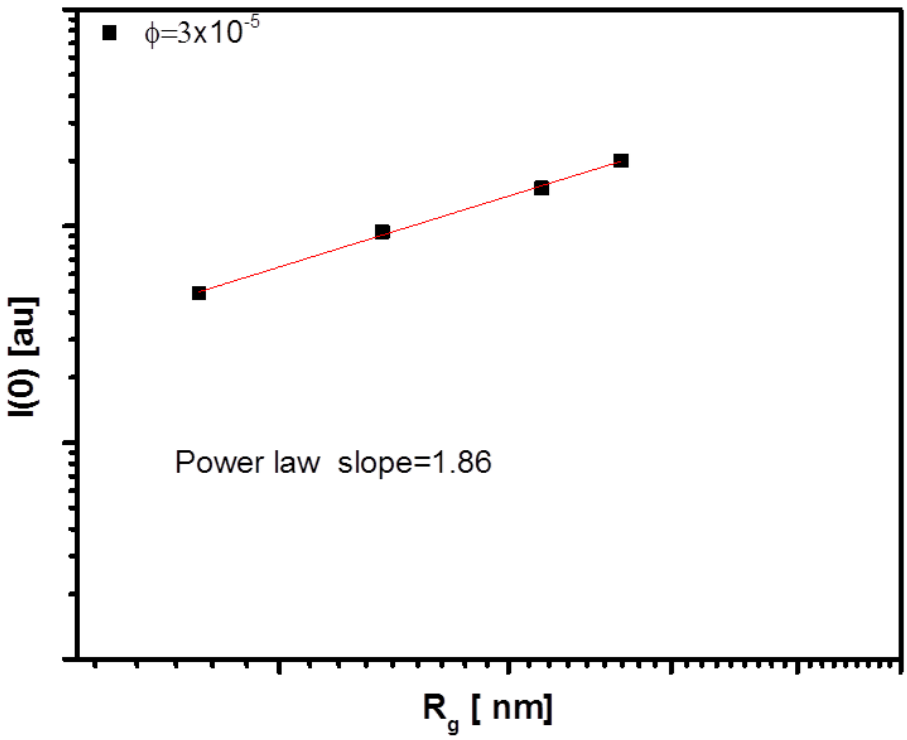

Figure 10 $I(0)$ vs. R_g plot for 50%MMA in the small angle static light scattering at $\varphi =$ $3x10^{-5}$

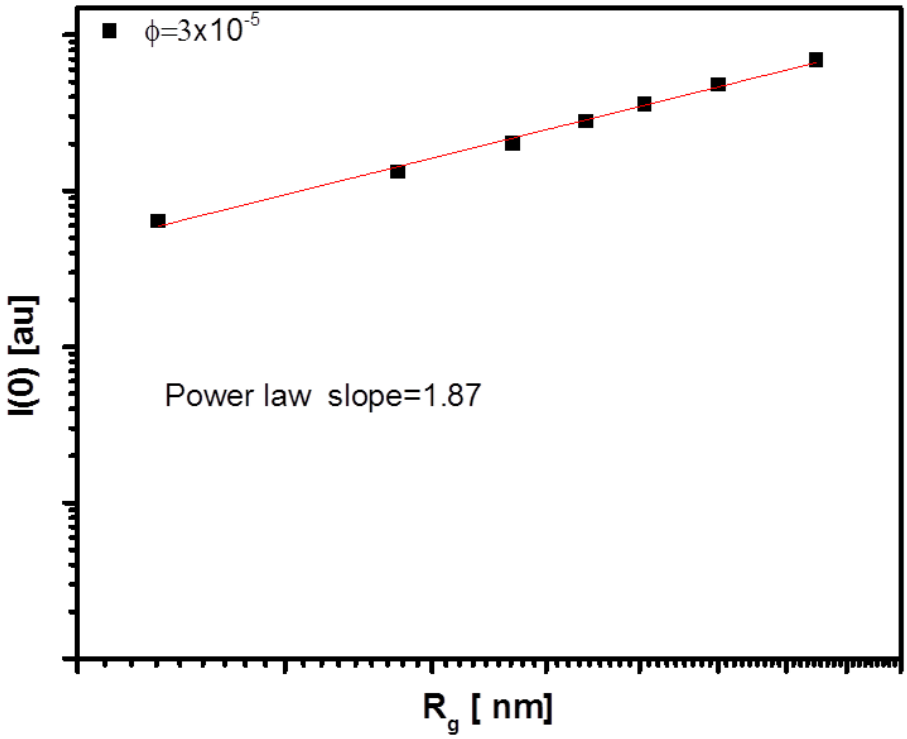

Figure 11 $I(0)$ vs. R_g plot for 60%MMA in the small angle static light scattering at $\varphi =$ $3x10^{-5}$

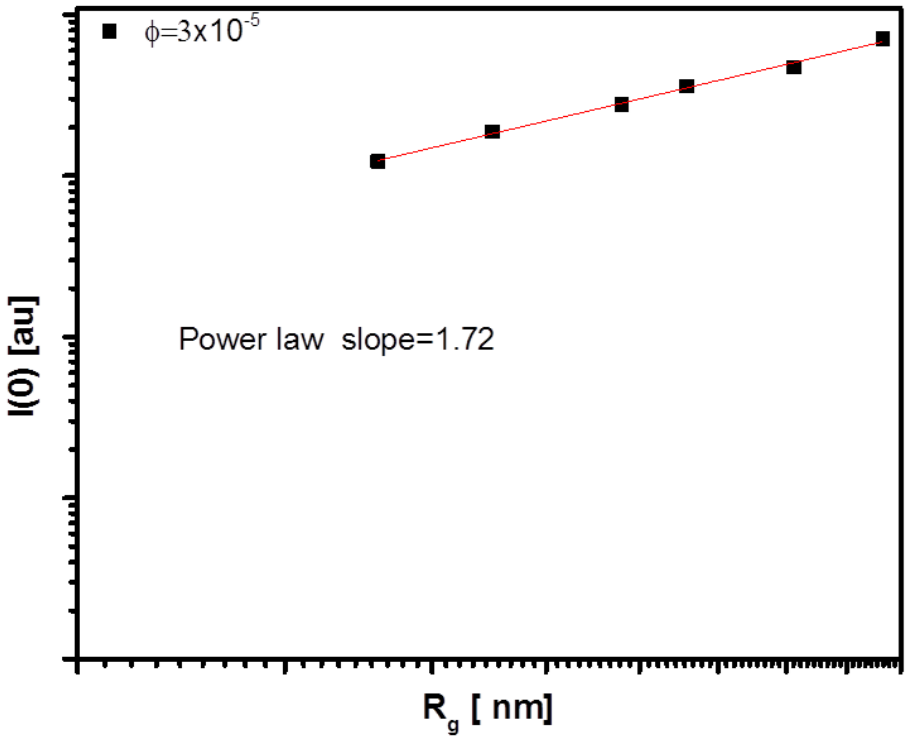

Figure 12 $I(0)$ vs. R_g plot for 70%MMA in the small angle static light scattering at $\varphi =$ $3x10^{-5}$

APPENDIX III

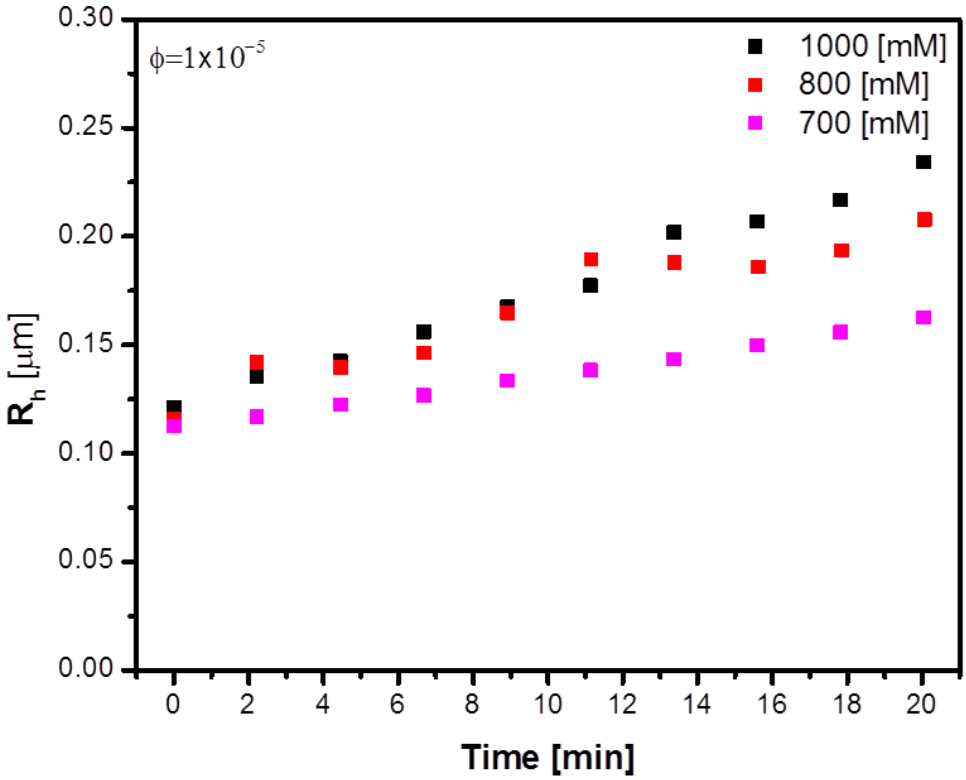

Figure 1 Aggregation kinetics in the dynamic light scattering at $\varphi =$ 1x10^{-5} and $T = 25$ [ºC] for 30%MMA

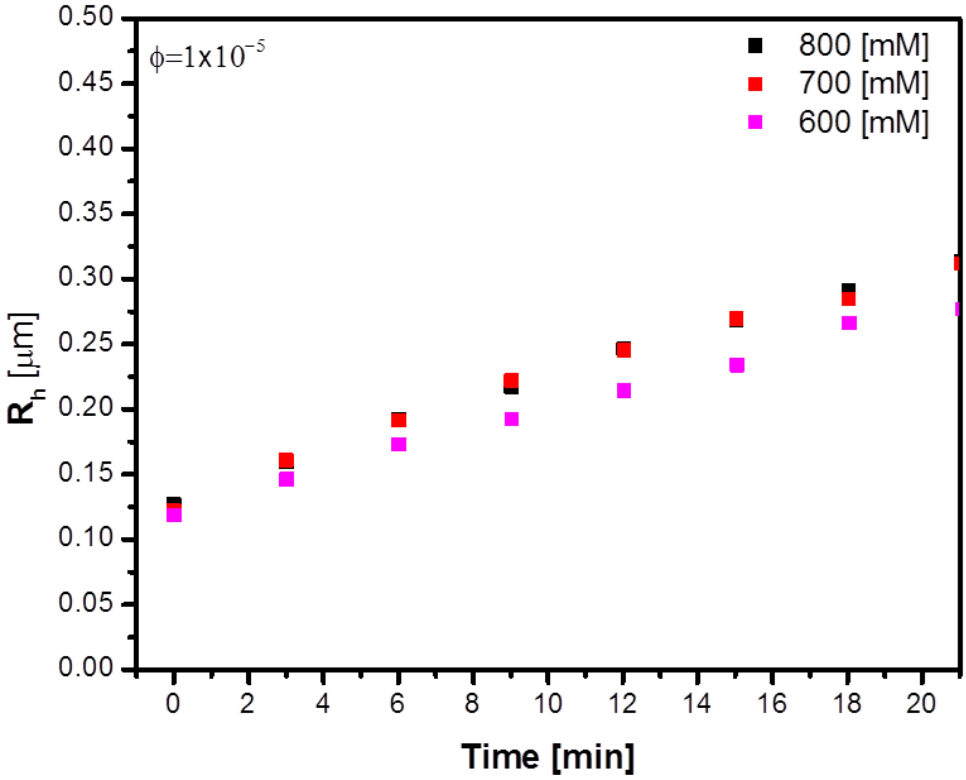

Figure2 Aggregation kinetics in the dynamic light scattering at $\varphi =$ 1x10^{-5} and $T = 25$ [ºC] for 50%MMA

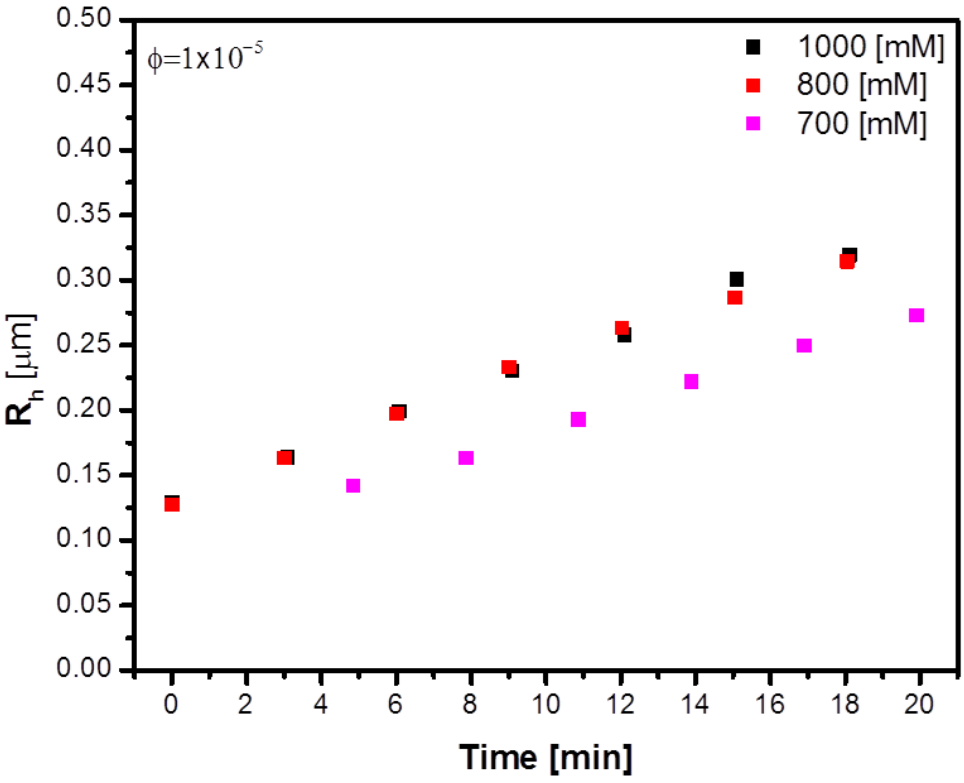

Figure 3 Aggregation kinetics in the dynamic light scattering at $\varphi =$ 1x10^{-5} and $T = 25$ [ºC] for 60%MMA

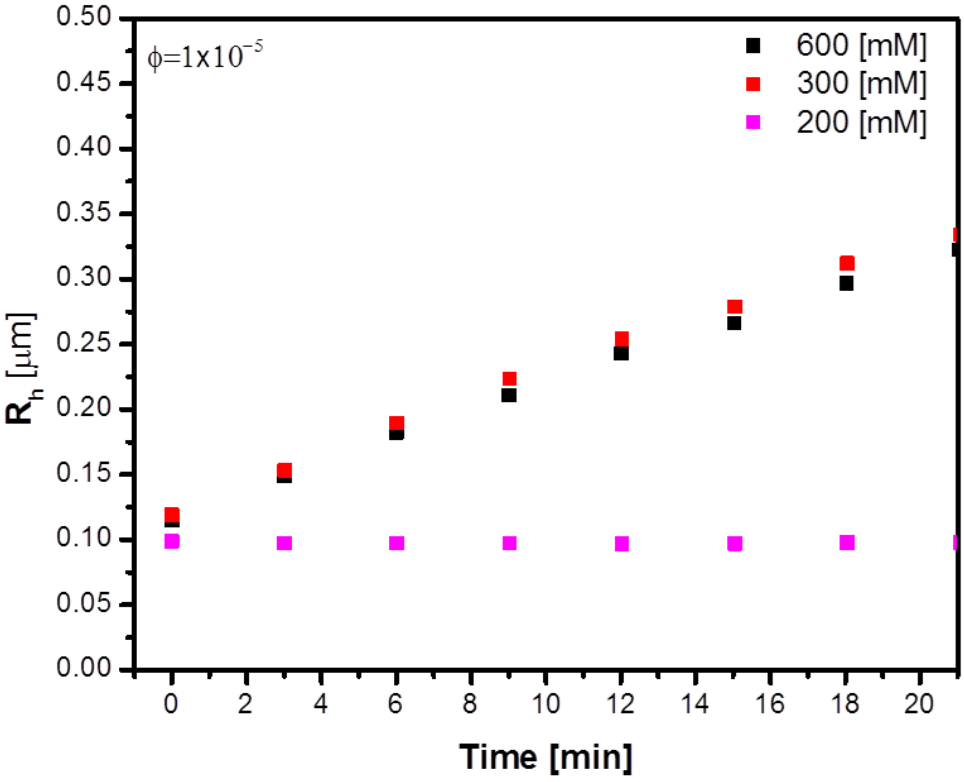

Figure 4 Aggregation kinetics in the dynamic light scattering at $\varphi =$ 1x10^{-5} and $T = 25$ [ºC] for 70%MMA

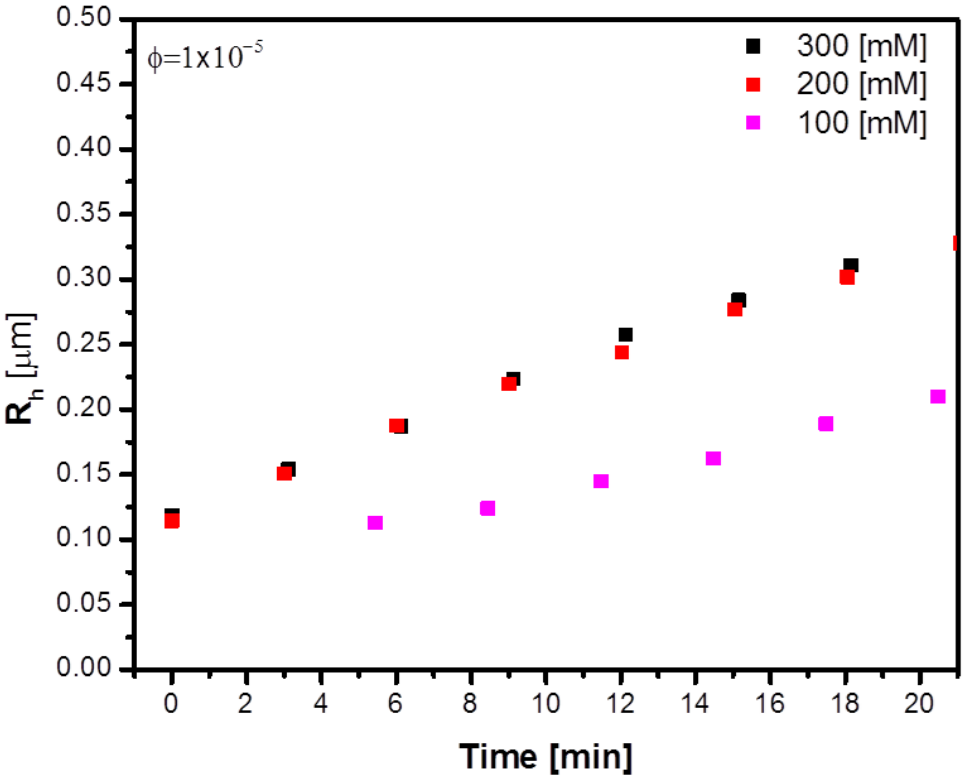

Figure 5 Aggregation kinetics in the dynamic light scattering at $\varphi =$ 1x10^{-5} and $T = 25$ [ºC] for 100%MMA